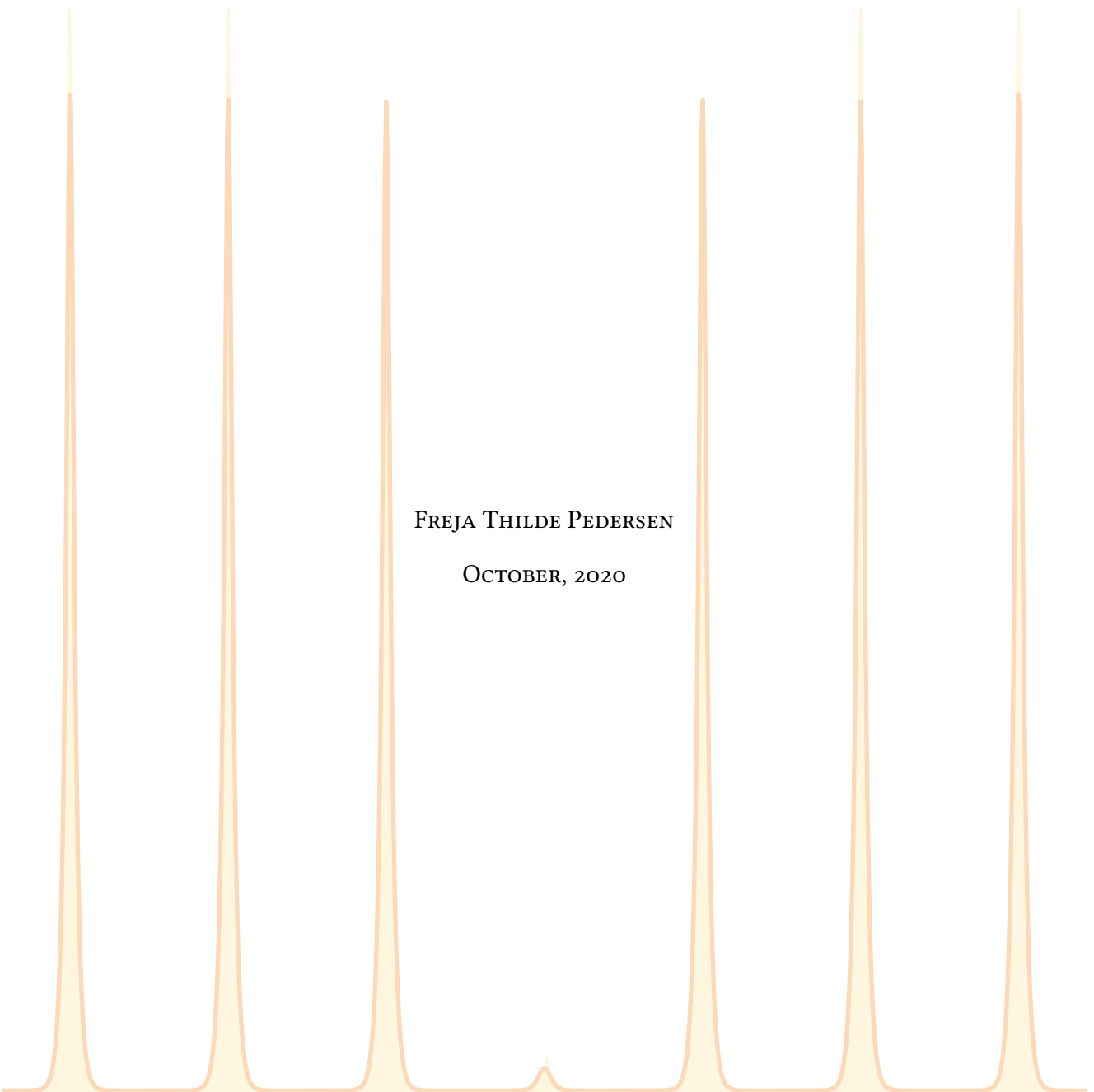


PHD THESIS

**DETERMINISTIC SINGLE AND MULTI-PHOTON
SOURCES WITH QUANTUM DOTS IN PLANAR
NANOSTRUCTURES**

FREJA THILDE PEDERSEN

OCTOBER, 2020



COVER IMAGE

Data from two-photon HOM interference.

COLOPHON

This thesis was set with \LaTeX using the memoir class.

The font is Libertine 10, on normal A4 paper

Graphics created using Matplotlib under Python 3.6, TikZ, as well as Inkscape.

Chapterstyles courtesy CP3.

DETERMINISTIC SINGLE AND MULTI-PHOTON SOURCES WITH QUANTUM DOTS IN PLANAR NANOSTRUCTURES

Author Freja Thilde Pedersen
Advisor Prof. Peter Lodahl
Advisor Asst. Prof. Ravitej Uppu



UNIVERSITY OF
COPENHAGEN

QUANTUM PHOTONICS

Center for Hybrid Quantum Networks (Hy-Q)
The Niels Bohr Institute

This thesis has been submitted to
The PhD School of The Faculty of Science
University of Copenhagen

October, 2020

ABSTRACT

Photonic qubits are key ingredients in the implementation of quantum-information processing and are ideal for interconnecting distributed nodes in a quantum network. Solid-state quantum dots have proven to be powerful and versatile sources of photonic qubits, both for single-photon emission and entanglement generation. Strong confinement in the quantum dot leads to discretized energy levels, which can be optically addressed to generate single-photons. Furthermore, the solid state environment enables engineering of the local photonic environment around the quantum dot, using a nanostructure, which is crucial in extracting and guiding the emitted photons with near-unity efficiency. The approach taken in this thesis is one among many and is employing a photonic crystal waveguide. Among the diverse array of nanostructures that were investigated for efficient single-photon generation, photonic crystal waveguides are promising owing to their broadband operation, near-unity efficiency, possibility for Purcell enhancement of the radiative decay rate, and a direct coupling to a single propagating mode. However, the introduction of nanophotonic structures and the solid-state environment typically introduce new sources of noise that should be suppressed to achieve emission of high quality photons. Moreover, to enable deterministic operation, resonant excitation schemes must be employed, where laser background suppression can be experimentally challenging.

Nearly ideal operation of self-assembled InAs quantum dots in photonic crystal waveguides as single-photon sources is presented in this thesis. We achieve close to perfect noise suppression by embedding the quantum dots in a *p-i-n* diode heterostructure for charge control. Robust resonant excitation is achieved in a thoroughly optimized experimental setup using carefully characterized quantum dots. We observe high single-photon emission 10 MHz, single-photon purity $g^{(2)}(0) < 1\%$ and indistinguishability of the emitted photons of $> 98\%$.

We also investigate the generation of polarization-entangled photon pairs from these high-quality quantum dots. Typically, polarization information of the photons is lost when the emission is coupled to a single-mode waveguide. However, photonic crystal waveguides support special locations called chiral points, which enable directional coupling of polarized emission. In this way, polarization entanglement can be converted to a spatial basis enabling on-chip entanglement generation. Finally, we present the first results towards the integration of droplet etched GaAs quantum dots into photonic crystal waveguides, which exhibit ideal properties for high-fidelity entanglement generation.

This thesis presents a quantum dot based source of photonic qubits which accommodates both scalable single-photon emission and the possibility for deterministic on-chip entanglement generation. Our source is therefore a strong resource in a future quantum based network.

SAMMENFATNING

Fotoniske qubits er en essentiel ingrediens for implementeringen af kvantemekanisk informationsprocessing, og er ideelle som forbindelse mellem adskilte punkter i et kvantemekanisk netværk. Faststofskvantepunkter har vist sig at være både en stærk og alsidig kandidat som en kilde til både enkeltfotoner og fotonisk entanglement. Kvantepunkter er så små, at den stærke lokalisering gør de interne energiniveauer diskrediterede. Disse energiniveauer kan drives optisk, og generere enkelte fotoner. Ydermere tillader faststofmaterialet, at man kan modificere det lokale fotoniske miljø rundt om kvantepunktet, ved at bruge en nanostruktur, hvilket er en essentiel komponent der leder og udkoble enkeltfotonerne med høj effektivitet. I denne afhandling har vi taget en tilgang ud af mange, som er at bruge en fotonisk krystal-bølgeleder. Blandt de forskellige tilgange til nanostrukturer er fotonisk krystal-bølgeledere lovende på grund af deres brede frekvensbåndbrede, deres koblingseffektivitet på næsten 100 % , deres mulighed for Purcell-forstærkning af henfaldsraten af kvantepunktet, samt direkte kobling til en propagerende mode. Desværre kan de nanofotoniske strukturer i faststofmiljøet rundt om kvantepunktet introducere nye støjkilder, som skal minimeres for at opnå emission af højkvalitetsenkeltfotoner. For at kunne realisere deterministisk emission skal kvantepunktet desuden exciteres resonant hvilket gør undertrykkelse af laserbaggrund udfordrende.

I denne afhandling præsenterer vi en tæt på ideel enkeltfotonkilde ved at bruge selvsamlende InAs kvantepunkter i fotonisk krystal-bølgeledere. Vi opnår tæt på perfekt undertrykkelse af støj ved at indlejre kvantepunkterne i en $p-i-n$ diode heterostruktur der kontrollerer elektrisk ladning. Robust resonant excitation opnås ved at bruge et grundigt optimeret eksperimentelt design sammen med omhyggeligt karakteriserede kvantepunkter. Vi har observeret høje enkeltfotonsemissionsrater på 10 MHz, god enkeltfotonrenhed $g^{(2)}(0) < 1\%$ samt en uadskillelighed på mere end 98 %.

Derudover undersøger vi generering af polarisationsentangled fotoner fra disse højkvalitetskvantepunkter. Typisk går polarisationsinformationen tabt når fotoner kobles til en enkelt-mode-bølgeleder. Imidlertid understøtter fotonisk krystal-bølgeledere specielle punkter kaldet kirale punkter, som tillader retningsbestemt kobling af polariseret emission. På denne måde kan polariseringsentanglement konverteres til en rummelig basis på chippen. Endelig præsenteres de første resultater hen imod at integrere dråbe-ætsede GaAs kvantepunkter i fotonisk krystal-bølgeledere. Disse kvantepunkter har tæt på ideelle egenskaber for at skabe højkvalitetsentanglement.

Denne afhandling præsenterer en kilde til fotoniske qubits baseret på kvantepunkter, som både imødekommer kravene for skalerbar enkeltfotonemission og giver muligheden for deterministisk entanglementgenerering på chippen. Vores kilde er derfor en stærk ressource i et fremtidigt kvantemekanisk netværk.

PREFACE

This thesis concludes three wonderful years spent in the *Quantum Photonics* group led by Professor Peter Lodahl at the Niels Bohr Institute, University of Copenhagen. It has been three years primarily spent in the laboratories, performing exciting experiments. I enjoy very much the experimental work which at times can be tedious but solving practical problems often makes a big difference and leads to exciting results in the end. Just as important as the interesting research is the absolutely fantastic colleagues that I have had, both as scientific co-workers and as an exceptionally socially strong and welcoming group.

I would like to start by thanking Professor Peter Lodahl for giving me this opportunity to work in the group. I would like to thank him for his great supervision and steering of the project throughout my PhD, and for creating a very nice work environment in the group. I would like to thank my former co-supervisor Matthew Broome who inspired me into applying for the PhD position in the group. The co-supervision was taken over by Ravitej Uppu, whom I would like to give my sincerest gratitude for his supervision. Ravi is highly invested in every project that he is involved in, and his enthusiasm and his constant drive is extremely inspiring and encouraging. I would like to thank him for everything he has taught me about experimental lab work and for sharing so much of his valuable knowledge. It has been a great pleasure working together, and I have enjoyed our many hours in the lab.

Furthermore I would like to thank the whole Quantum Photonics group, for being wonderful colleagues, who are always up for both assistance in the lab. a good scientific discussion, or karaoke and a beer on a Friday evening. There are some people that I would like thank more specifically. First, Cecilie T. Olesen and Adam Knorr, two master students that I have enjoyed working with and would like to thank for helping me carrying out experiments. Furthermore, I would like to thank Ying Wang and Aslı Uğurlu for sample fabrication and Leonardo Midolo for teaching me how to design masks and help with photonic structure design. Besides the aforementioned people there are a couple of more who I would like to thank for their help in simulations, lab work or scientific discussions; Xiaoyan Zhou, Martin H. Appel, Eva M. González Ruiz, Camille Papon, Hanna Le Jeannic, Nils V. Hauff, Henri Thyrrstrup and Thomas Hummel. Lastly I would also like to thank all of Hy-Q and the quantum optics section for great discussions and knowledge sharing.

I would like to thank two external groups for supporting this thesis work as well. First a great thanks to Professor Armando Rastelli, Daniel Huber and Siamon F. Silva for providing one of the samples used in the thesis, and letting us visit their lab to learn some specific experimental procedures. Secondly, I would like to show my gratitude to Professor Gregor Weihs and Maximilian Prilmüller for letting me conduct my *change of scientific environment* in their group, with great supervision and many highly fruitful discussions.

I would also like to thank Sofie Janas, Jonas Mathiassen, Viktor L. Holm, Asbjørn A. Jørgensen and Anders Bakke for reading and commenting my thesis at an early stage.

A special thanks goes to Sofie Janas and Hanna Le Jeannic for taking me out for dinner and other small activities during the writing months.

Finally, an enormous thanks goes to my fantastic boyfriend Christoffer Østfeldt, who has both been incredibly patient and supportive for this project. I would like to thank him for taking care of me in terms of cooking and moral support through the months of thesis writing, and for his huge work on reading and commenting the thesis. Furthermore, I would like to thank my family for always supporting me, and my little 8 month old nephew, from whom I have received motivational text messages along the way.

LIST OF PUBLICATIONS

- *Near Transform-limited Quantum Dot Linewidths in a Broadband Photonic Crystal Waveguide.* Freja T. Pedersen, Ying Wang, Cecilie T. Olesen, Sven Scholz, Andreas D. Wieck, Arne Ludwig, Mathias C. Löbl, Richard J. Warburton, Leonardo Midolo, Ravitej Uppu and Peter Lodahl. ACS Photonics 2020, 7, 9, 2343–2349.
- *Scalable integrated single-photon source.* Ravitej Uppu, Freja T. Pedersen, Ying Wang, Cecilie T. Olesen, Camille Papon, Xiaoyan Zhou, Leonardo Midolo, Sven Scholz, Andreas D. Wieck, Arne Ludwig, and Peter Lodahl. Accepted in Science Advances.

IN PREPARATION

- *Single photon purity of a resonantly excited quantum dot single-photon source* Freja T. Pedersen, Cecilie T. Olesen, Ying Wang, Johannes Bjerlin, Sven Scholz, Andreas D. Wieck, Arne Ludwig, Anders S. Sørensen, Ravitej Uppu and Peter Lodahl.
- *Chirally coupled biexciton decay for on-demand entangled photon pair generation.* Freja T. Pedersen, Ying Wang, Adam Knorr, Tommaso Pregolanto, Sven Scholz, Andreas D. Wieck, Arne Ludwig, Ravitej Uppu and Peter Lodahl.

CONTENTS

Abstract v

Preface vii

List of publications ix

- 1 Photonic Quantum Dots as a Resource for Quantum Information** 5
Perspectives on how single- and multi-photon sources are key resources for a future quantum information network, and how solid state quantum dots have the ability to realize these resources.
- 2 Quantum Dots as Photon Emitters** 9
Introduction to semiconductor quantum dots as emitters and how their discretized electronic states can be employed as a single- and multi-photon sources.
 - 2.1 Semiconductor Heterostructures 10
 - 2.2 Epitaxial Growth of Quantum Dots 12
 - 2.3 Excitonic States 14
 - 2.4 Control of the Quantum Dot Charge Environment 16
 - 2.5 Two-level Emitter 18
 - 2.6 Multiphoton Emission from the Biexciton 24
- 3 Nanophotonic Structures for Deterministic Generation of Photons** 29
Presentation of different approaches to nanophotonic structures followed by an introduction to the approach in this thesis; a photonic crystal waveguide with shallow-etched grating outcouplers.
 - 3.1 Approaches for Modifying the Photonic Environment 30
 - 3.2 Photonic Crystal Waveguides 32
 - 3.3 Planar Integration and Photon Outcoupling 37

- 4 Optimized Experimental Design 41**
Details of the experimental setup employed in this thesis, optimized and characterized to achieve high performance.
- 4.1 Experimental Setup 41
 - 4.2 Efficiency Characterization 48
 - 4.3 Electrical Characterization 52
- 5 A Scalable Single-Photon Source 55**
Thorough quantum dot characterization allows scalable single-photon emission. The procedures presented can be used as recipe for achieving high quality single photon emission from quantum dots in planar waveguides.
- 5.1 Photonic Crystal Waveguide Characterization 55
 - 5.2 Resonant Transmission for Quantum Dot Search 57
 - 5.3 Resonant Spectroscopy 58
 - 5.4 10 MHz Single-photon Source 64
 - 5.5 Near Lifetime-limited Linewidths in Photonic Crystal Waveguides 67
 - 5.6 Single-photon Purity 70
 - 5.7 Photon Indistinguishability 75
- 6 Optimizing Resonant Excitation Schemes 85**
Two approaches to resonant excitation schemes, which has the potential to improve the single-photon quality are studied and discussed.
- 6.1 Optimized Excitation Laser Pulse Bandwidth 85
 - 6.2 Two-photon Resonant Excitation 90
- 7 Polarization Entanglement from the Biexciton Cascade 99**
The method for tomographic reconstruction of polarization-entangled photons is presented and performed using photons emitted from a quantum dot.
- 7.1 Reconstruction of a Two-mode Quantum State 99
 - 7.2 Experimental Realization of Polarization Entanglement 102
- 8 Chiral Coupling of the Biexciton Cascade 111**
The polarization entanglement generated from the biexciton cascade can be preserved and converted to path-encoding by chiral coupling in a planar nanophotonic structure.
- 8.1 Chiral Nanostructure for Entanglement Preservation 112
 - 8.2 Experimental Evidence of Chirally Coupled Biexciton 115
- 9 Low-Strain Droplet-Etched Quantum Dots Coupled to Nanostructures 121**
Progress on the integration of droplet etched quantum dots in planar nanophotonic structures are presented. These dots are promising for entanglement generation due to their low strain.
- 9.1 Bulk Spectroscopy and Fine Structure Splitting 122
 - 9.2 Nanophotonic Structures in AlGaAs 124

10 Conclusions and Outlook 131

Conclusions and summary of the work carried out in this thesis, and an outlook towards future work for single and entangled photons from quantum dots in photonic crystal waveguides.

Bibliography 135

CHAPTER
1PHOTONIC QUANTUM DOTS AS A RESOURCE
FOR QUANTUM INFORMATION

Perspectives on how single- and multi-photon sources are key resources for a future quantum information network, and how solid state quantum dots have the ability to realize these resources.

Classical information technology has revolutionized the way we live and communicate, and in many ways defines the modern world. This revolution occurred due to the development of the transistor (Bardeen & Brattain, 1948; Shockley, 1949) followed by rapid advances in miniaturizing solid-state processors to realize compact computers. The computers together with optical fiber interconnects enable transferring massive amounts of data using short optical pulses, which forms the internet. Today we stand on the edge of the next technological revolution, namely the potential reality of a *quantum internet* (Kimble, 2008; Wehner et al., 2018).

A key requirement for realizing a quantum internet is to establish interconnects between local quantum processors that enable quantum communication across spatially separated nodes. The quantum-based network is expected to supplement the classical internet with the potential of addressing specific problems and enabling protocols that would otherwise be impossible. Classical information is carried in bits, which can take the value of either 0 or 1. A collection of bits can form a binary string in which information is encoded. Quantum information can be encoded in quantum bits or *qubits*, which can be $|0\rangle$ or $|1\rangle$ but also in any arbitrary superposition of the two $a|0\rangle + b|1\rangle$, where $|a|^2 + |b|^2 = 1$.

Qubits can be encoded in various different physical systems that have two quantized states such as atomic energy levels, electron spin, or single photons. In this thesis, we

focus on photonic qubits, which are ideal candidates to realize quantum interconnects, where single photons could transmit through the existing fiber based network as flying qubits. More information can be carried in a qubit than in a classical bit, due to the possibility of superposition states. Over the past few decades, new computing algorithms that utilize the potential of quantum physics to overcome the classical limitation have been developed (Deutsch & Jozsa, 1992; Grover, 1996, 2001; Shor, 1994). One example is the factorization of a large integer that no known classical algorithm can efficiently perform. This inefficiency of classical algorithms ensures the security of widely used encryption protocols (Rivest et al., 1978). With Shor's algorithm, employing qubits, the factorization can be carried out in polynomial time with increasing integer size (i.e. far more efficient than the exponential scaling of classical algorithms) (Shor, 1994). This is an example of how quantum-based information technology have a computational advantage over classical technologies.

However, factorization, as well as the far more wide-reaching goal of implementing an universal quantum computer, requires control of many qubits and the implementation of high-fidelity operations between qubits. Given these challenging tasks, one could ask the question: "Is there an intermediate experiment that could demonstrate the advantage of quantum physical systems?". Different experiments designed, to solve problems that are hard to solve for a classical computer but easy for a quantum computer have been proposed, and one was recently demonstrated with superconducting qubits (Arute et al., 2019). For photonic qubits, *Boson sampling* is the most promising approach to do this (Aaronson & Arkhipov, 2013). Boson sampling can be realized by sending N identical photons into an M -mode interferometer and detecting the photon correlations at the output of the interferometer. For the experimental realization, a high efficiency of the photon source, as well as transmittance through the sampling interferometers, is key (H. Wang et al., 2017). Sampling the output probability distribution of the network can be much more efficient than simulating such an output on a classical computer. As the number of modes is scaled up, the complexity of the classical problem becomes insurmountable, and the boson sampler has an advantage in sampling the outcome. Efficient boson sampling relies additionally on indistinguishability of the N input photons, and therefore single photons of high quality are required to realize this (Renema et al., 2018). A state-of-the-art boson sampling experiment has been carried out with 20 photons (H. Wang, Qin, et al., 2019), where the pair-wise indistinguishability of the photons varied between 90 % and 96 %, which could prove to be limiting for scaling up to > 50 photons required for demonstrating quantum advantage. A boson sampler can experimentally be realized using integrated photonics, where the interferometric network is integrated on a chip (Carolan et al., 2015; Tillmann et al., 2013). Such reprogrammable optical circuits also have the potential to simulate complex multi-body chemistry problems (Aspuru-Guzik & Walther, 2012) as well as for learning algorithms in a neural network (Shen et al., 2017).

Photonic qubits, further, enable secure communication between two nodes that relies on no *a priori* assumptions except the validity of the laws of quantum mechanics. A secret key can be generated by sharing a string of single photons between two nodes by using the BB84 protocol (Bennett & Brassard, 1984, 2014). In order to disallow

any side channel attacks by an eavesdropper, establishing the secret key can be made secure by sharing a maximally-entangled state between the sender and the receiver. The E91 protocol employs entangled photon pairs, where the security is ensured by violating Bell's inequality (Bell, 1964; Ekert, 1991). Violating Bell's inequality requires high efficiency of the entangled pair generation of $> 83\%$ using the CHSH experiment (Clauser et al., 1969) but can be reduced to 67% using a non-maximally entangled state (Eberhard, 1993). This high efficiency requirement rules out the possibility to entangle two single photons using linear optical components, which has a maximal efficiency of 50% (Calsamiglia & Lütkenhaus, 2001). Ultimate secure communication can be guaranteed by introducing additional security requirements for realizing device-independent quantum key distribution (Acín et al., 2007; Máttar et al., 2020) where a secret key can be securely established between two nodes without the need of trusting the measurement apparatus or any other physical devices.

Single-photon generation was first demonstrated from the emission of an excited atom in Kimble et al., 1977, by observing anti-bunching in the photon statistics. The subsequent experiments studying the light-matter interaction continued with better control of the emitter, and excitation field, forms the extensively studied field of experimental quantum optics. However, atomic experiments require active trapping of the atoms leading to complicated experimental setups. Solid-state alternatives to two-level emitters which include e.g.; nitrogen-vacancy centers (Kurtsiefer et al., 2000), single molecules (Lounis & Moerner, 2000) and semiconductor quantum dots (Michler et al., 2000) emerged a few decades later. This thesis focuses in quantum dots. In 2002 the first experiments demonstrating indistinguishable single-photon emission from quantum dots were performed (Santori et al., 2002). Since then, great effort has been put into optimizing quantum dot properties towards achieving well isolated energy levels. In parallel to quantum dot developments, advances in photonic nanostructures integrated into the solid-state material have enabled stronger light-emitter coupling and high extraction efficiencies of the quantum dot emission in nanofabricated structures such as, e.g., nanowires, micropillar cavities or photonic crystal waveguides (Claudon et al., 2010; Lund-Hansen et al., 2008; Santori et al., 2002). We employ quantum dots coupled to photonic crystal waveguides as a single-photon source in this work.

Deterministic single- and entangled photon generation is key for a large scale quantum network, for this quantum dots coupled to nanophotonic structures are strong candidates. The current workhorse for single- and entangled photon generation is from a fundamentally different process not based on a two-level emitter. Photon generation from spontaneous parametric down-conversion (SPDC) was discovered around the same time as the solid-state emitters (Kwiat et al., 1995). Photons generated using SPDC sources, exhibit high indistinguishability, and are the most widely employed source due to their simplicity of implementation and operation. However, these sources are probabilistic and therefore there is a limit to the achievable generation efficiency in order to keep multi-photon generation low (Kaneda & Kwiat, 2019), could be problematic for scale up to a quantum network. In this thesis, we present a single-photon source with indistinguishability of $> 96\%$ across a string of > 100 photons that is at the same level or better than typical SPDC source demonstrations (Zhong et al., 2018).

Importantly, the use of quantum dots embedded in a photonic nanostructure enables near-deterministic operation with source efficiencies that would enable boson sampling with > 50 photons. We further show a pathway for deterministic entangled photon generation.

More specifically the thesis covers:

In [chapter 2](#), the emitter employed as a photon source is introduced, namely the solid-state quantum dot. First, the growth and the resulting confined electronic states are presented. After this, we discuss the optical properties of the quantum dot assuming a two-level system, that is afterwards expanded to include multiple levels to describe more realistically the quantum dot system.

[Chapter 3](#) gives an overview of the different nanophotonic structures employed in the literature and discusses the photonic crystal waveguides employed in this thesis.

In [chapter 4](#) we detail the experimental setup and its thorough characterization and optimization to achieve the high performance needed to perform the measurements presented later in this thesis.

[Chapter 5](#) presents a thorough recipe for identifying a quantum dot with good single-photon emission properties. We highlight the importance of charge control of the quantum dot emission leading to near transform-limited linewidths which is crucial for achieving indistinguishable emission. Under carefully optimized resonant excitation, we demonstrate high emission rates of nearly perfectly indistinguishable single photons.

In [chapter 6](#) we discuss two different resonant excitation schemes, which have the potential to improve the emitted single-photon properties.

[Chapter 7](#) presents a quantum dot that can be employed as an entangled photon source. The work presented here was conducted during an external stay at the University of Innsbruck.

[Chapter 8](#) demonstrates conversion of polarization encoding to path encoding of the biexciton cascade using directional coupling in a photonic crystal waveguide. This demonstration enables on-chip path entanglement generation.

Finally, [chapter 9](#) presents progress on integration of a newer type of quantum dots into planar nanophotonic structures. These newer quantum dots exhibit lower strain due to droplet etching method employed for fabrication and are particularly interesting for implementation as an entangled photon source.

We round off by presenting conclusions on this thesis work and outlook for future work in [chapter 10](#).

CHAPTER
2

QUANTUM DOTS AS PHOTON EMITTERS

Introduction to semiconductor quantum dots as emitters and how their discretized electronic states can be employed as a single- and multi-photon sources.

Single photons are promising candidates for interconnections of nodes in a quantum based network (Kimble, 2008; Wehner et al., 2018). If interfaced with a memory, they can serve as flying qubits for transport of information. However, single photon generation based on atoms is exceedingly complex, due to the challenges related to trapping of neutral atoms.

Quantum dots, a special kind of nanofabricated solid-state structure, offer a viable alternative, which foregoes the need for trapping. In this chapter, we will cover the basic operational principles and the needed physics, to appreciate the advantages and also drawbacks related to the use of quantum dots as single-photon sources.

Naturally, we will need to cover the enormous field in relatively short order; the interested reader may consult e.g. Michler, 2017 for more in-depth discussions. In section 2.1 we briefly present the electron bands in semiconductor heterostructures that are used to form the quantum dot potential. After that, in section 2.2, we quickly jump to explaining how quantum dots can be fabricated, leading to 0-dimensional confinement of an electron in a quantum dot. In 2.3, we present the states resulting from the electron confinement, and in 2.4, we discuss an experimental knob to tune the states. Finally, in sections 2.5 and 2.6, we present a set of calculations describing the optical properties, first in a simple two-level system, whereafter multiple states are included.

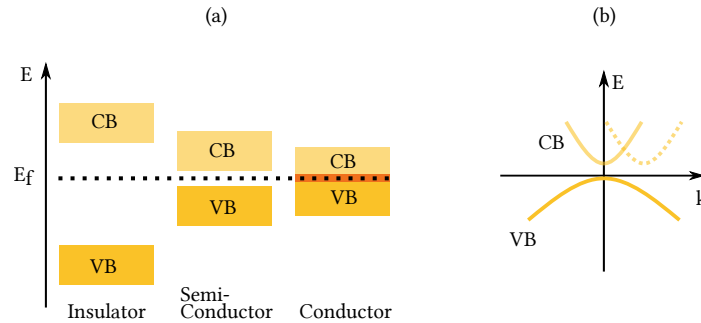


Figure 2.1: (a) Illustration of different types of materials with different band gap properties by the location of the valence band (VB) and conduction band (CB). (b) Schematic of energy dispersion relation of a semiconductor. Solid line represents a direct band gap, while the dotted line shows an indirect band gap.

2.1 SEMICONDUCTOR HETEROSTRUCTURES

In this section, we briefly introduce the principle behind using the electronic band structure of two semiconductors to make a trapping potential, forming a quantum dot.

Quantum dots are made from two semiconductor materials with different bandgap energies, which are joined in a *heterostructure*. Due to the periodic potential that electrons experience in crystalline lattices, energy band gaps can emerge between the valence band (VB), the highest energy band occupied with electrons, and the next energy band, the conduction band (CB). Semiconductors are distinguished from conductors and insulators in their conduction properties as a consequence of their intrinsic lattice structures. In insulators and semiconductors, the bandgap is located at the Fermi level E_f , in contrast to conductors, where electrons flow freely between the two bands, as illustrated in figure 2.1(a). Large band gaps lead to an insulator, where all flow of electrons are blocked. For semiconductors, the distance to the Fermi level is small enough that transitions between the two bands can be mediated with a small amount of external energy.

In figure 2.1(b), a simplified schematic of the energy dispersion relation $E = E(k)$ of the electronic bands in a semiconductor is shown, as a function of the wavenumber k . For certain materials such as GaAs (gallium arsenide), the bandgap is so-called direct. A direct bandgap is when the lowest energy state of the CB and the highest energy state of the VB is located at the same k . This is shown with the solid line in figure 2.1(b). For an indirect bandgap, there is an offset in the extrema, as illustrated with the dotted line. In a direct bandgap configuration, the absorption of a photon can bring an electron to the conduction band, since optical transitions are allowed due to momentum conservation; $\Delta k = 0$. When an electron is excited to the conduction band, what is known as a *hole* is left behind in the valence band. A hole is the absence of an electron, and another picture of the valence band states.

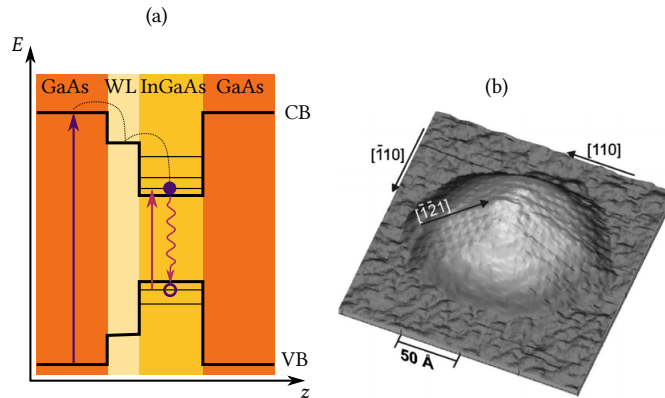


Figure 2.2: Semiconductor quantum dot (a) The heterostructure of an InAs/GaAs quantum dot. The different band gap regions forms a potential well in the conduction and valence bands (CB, VB). Optical transitions are illustrated with arrows, where aboveband is purple and resonant is indicated with red. (b) Scanning tunnelling microscope image of an InAs self-assembled quantum dot, grown on GaAs. $[110]$, $[\bar{1}10]$ and $[\bar{1}21]$ are the crystallographic axes defined during growth. Figure is from (Marquez et al., 2001).

By combining two materials with different bandgap energies in a heterostructure, it is possible to make a spatial potential profile for the electrons at the interface. For carefully selected combinations of materials, with similar lattice constants, it is possible to grow them together⁽¹⁾, with an abrupt transition from one material to the other. By surrounding a material with a lower energy gap by a material with a higher gap, a potential well can be formed. If the confinement is tight and in all three dimensions, such that the electrons have no free movement, discretized energy levels form. This is comparable to the discretized levels in an atom, and the reason why quantum dots are sometimes called *artificial atoms*. Discretized levels are reached if the physical size of the low bandgap material region is small, much smaller than optical wavelengths. The quantization energy of these states is on the order of tens of meV and must be addressed temperatures of a few Kelvin, to not populate them thermally instead. The confinement potential of an InGaAs/GaAs (indium gallium arsenide/gallium arsenide) type quantum dot is shown in figure 2.2(a). The dark yellow region is the potential well forming the quantum dot surrounded by the bulk GaAs. The wetting layer (WL) is formed during the growth at the interface between the two semiconductor materials, leading to a less deep potential well and should ideally be avoided.

By the absorption of a photon, an electron can be excited from the valence band and into the conduction band. Together with the hole in the valence band, they form a bound state called an *exciton*. When the absorbed photon has the same energy as the energy difference of the well, we call it resonant excitation, indicated with the red arrow. Alternatively above band excitation is also possible, where the excitation is

(1) Epitaxially, see next section.

created in the bulk material with an energy higher than the bandgap energy, illustrated with the purple arrow. From here, the electron relaxes down via nonradiative processes into the quantum dot potential well, while the hole 'bubbles' up in the potential. The bound exciton in the potential well will recombine resulting in the emission of a single photon. This lowest state has an s-like character, also observed in atomic electron orbitals. Higher discretized states in the CB (or sub-bands) in the quantum dot also exist, which have a p-like orbital character.

The intrinsic performance of the quantum dot is to a great extent defined by how good the confinement potential is, and is determined by the quality of the growth of the semiconductor heterostructure. Epitaxial growth, which will be introduced in the next section, allows extremely pure growth, together with the flexibility of changing the materials during growth to form the heterostructure.

2.2 EPITAXIAL GROWTH OF QUANTUM DOTS

We will in this section introduce how quantum dots are grown, using *molecular beam epitaxy*, but in two different ways. Molecular beam epitaxy allows growth of monolayers of the semiconductor under highly controlled conditions in vacuum, which ensures high purity of the material. The monolayers grow epitaxially, meaning that the crystalline layers are formed at well-controlled orientations, which is crucial for quantum dot growth. A heterostructure can be made directly during one growth process, where the content of the molecular beam can be changed. The crystal lattices need to be compatible, for the composite structure forming the quantum dots to be grown epitaxially. The most commonly used is the so-called *Stranski-Krastanov self-assembled quantum dots*, which are used for the majority of this thesis, but another type of epitaxially grown quantum dots is also studied, namely *droplet etched quantum dots*.

2.2.1 Self-assembled Quantum Dots

Self-assembled quantum dots are grown by exploiting the intrinsic strain caused by the lattice mismatch of the two materials in the heterostructure. This is known as the Stranski-Krastanov method. The dots consist of InAs epitaxially grown on top of GaAs, which have a 7% lattice mismatch. After a few monolayers of InGaAs the strain is released and small clusters of InAs will form. The clusters consist of $\sim 10^4 - 10^5$ atoms and have dimensions of 15 – 20 nm diameter and 5 – 10 nm in height. In figure 2.2(b) a scanning tunneling microscope 3D image of a quantum dot is displayed, where the typical conical shape is seen. The quantum dot is formed when it is capped off with GaAs on top, to form 3D confinement.

The spontaneous assembly process leads to inhomogeneous properties of the quantum dots. This means that two quantum dots will emit at slightly different wavelengths and that their location is completely random. However, this growth method has proven to be one of the most robust methods, leading to quantum dots with excellent performance as single-photon emitters (Lodahl et al., 2015). The few monolayers building up before the strain is released is what forms the wetting layer (WL) shown in figure

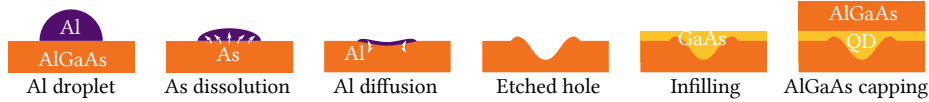


Figure 2.3: Growth process of droplet etched quantum dots. Holes are etched into an AlGaAs substrate by a droplet of Al. This leads to highly symmetric holes, which are then infilled by GaAs and capped off with AlGaAs to form a quantum dot in the last panel. Figure is reproduced from Keil et al., 2017

2.2, which is a 2D confinement well from which electrons can scatter into the quantum dot. Recently it has been shown that by a modification of the growth protocol, the electron wetting layer states can be eliminated by overgrowing the quantum dots with a monolayer of AlAs, effectively creating a barrier to the quantum dot well (Löbl et al., 2019). The InGaAs/GaAs quantum dots used in this thesis were grown by Scholz, S., Ludwig, A. and Wieck, A. D. from our collaboration group Lehrstuhl für Angewandte Festkörperphysik, Ruhr Universität Bochum, Germany.

The growth method is based on strain, the majority is released when the clusters are formed, but some strain remains in the final quantum dot. This residual strain affects the quantum dot electronic transitions as it will be explained later. Droplet etched quantum dots are emerging as an alternative type, which contains less strain and further potentially have much cleaner transitions between the materials.

2.2.2 Droplet Etched Quantum Dots

Low strain quantum dots can be grown with GaAs embedded in AlGaAs (aluminum gallium arsenide). There is almost perfect lattice matching between the two semiconductors and they form a nearly ideal heterostructure (Rastelli et al., 2004). This means that they cannot be grown with the traditional self-assembly process. Instead, by making nanoholes in the AlGaAs substrate and infilling with GaAs, quantum dots can be made. The growth process is depicted in figure 2.3.

The nanoholes are formed with droplet etching, where aluminum droplets are randomly deposited on the AlGaAs substrate, and via a diffusion process, the aluminum leaves highly symmetric holes in the substrate. The hole is epitaxially filled with GaAs, and due to the weak intermixing between the two materials, the GaAs dot takes the symmetric shape of the etched hole. The quantum dots are then capped off again with AlGaAs to enclose the quantum dot.

The high symmetry of the quantum dot is visible in top view of the 3D atomic force microscopy (AFM) image shown in figure 2.4(b). The dimensions are around 50 nm laterally and 10 nm high. Figure 2.4(a) shows the cross section of the AFM image, highlighting the shape of infilled hole forming the quantum dot.

Reproducible growth of GaAs/AlGaAs quantum dots with systematic geometry has been challenging, but after mastering the growth (Huo et al., 2013), droplet etched GaAs quantum dots have been popular for implementation of a polarization-entangled photon source (D. Huber et al., 2017; Keil et al., 2017; Liu et al., 2019). Very recently emission properties have been more carefully characterized under resonant excitation (Schöll

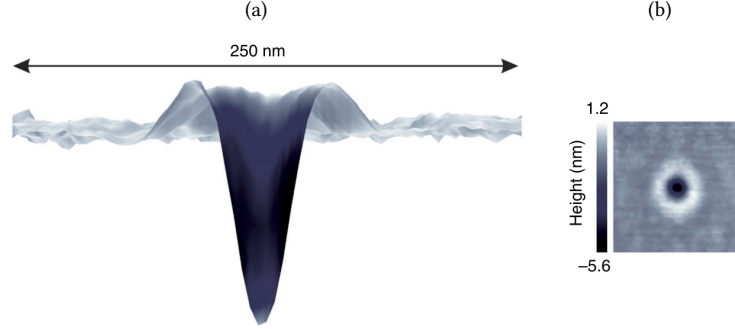


Figure 2.4: (a) Cross section of a 3D AFM image of a quantum dot grown with the droplet etching method. The height-to-width ratio is amplified 17 times to highlight the nanohole shape. (b) Top view of the AFM image revealing the high in-plane symmetry of the quantum dot. Figure is adapted from (D. Huber et al., 2017).

et al., 2019; Zhai et al., 2020), showing excellent single-photon properties. Finally, the emission wavelength overlaps with the D2 line in Rubidium and this combination is therefore highly attractive as a single photon quantum memory (Akopian et al., 2010; Jahn et al., 2015; Keil et al., 2017).

The samples of droplet GaAs/AlGaAs quantum dots studied in this thesis was grown by Covre da Silva, S. F and Rastelli, A. in Linz, Austria, Institute of Semiconductor and Solid State Physics, Johannes Kepler University.

2.3 EXCITONIC STATES

We will now discuss the states resulting from the confinement of an electron in a quantum dot, and the associated optical transitions.

An excitation in a quantum dot called an exciton, consist of an electron ($|\uparrow\rangle$) -hole ($|\uparrow\rangle$) pair forming a bound state by the Coulomb interaction. The electronic states are characterized by the total angular momentum $J = S + L$, along the quantization axis which is taken to be the growth direction z . Both electrons and holes are fermions with spin $S_{e/h} = \frac{1}{2}$. The orbital angular momentum L is given by the symmetry of the relevant electronic band. For electrons in the conduction band which have an s -like character $L_e = 0$ while the valence bands has p -like orbitals, leading to $L_h = 1$ for the holes. The projected total angular momentum therefore is $J_e^z = \pm\frac{1}{2}$ and $J_h^z = \pm\frac{3}{2}$. The combination of an electron and hole $J_{e,h}^z = J_e^z + J_h^z$ allows four possible bound states $|\uparrow\uparrow\rangle = |J_{e,h}^z = -1\rangle$, $|\downarrow\uparrow\rangle = |J_{e,h}^z = 1\rangle$, $|\uparrow\uparrow\rangle = |J_{e,h}^z = 2\rangle$ and $|\downarrow\downarrow\rangle = |J_{e,h}^z = -2\rangle$. Since all energy transitions to the ground state, where $J = 0$ that we are interested in, are mediated with photons (exciting or emitting) only the $\Delta J = \pm 1$ are allowed. This is because photons can carry angular momentum of ± 1 (if circular polarization), leaving the $J = \pm 2$ states as *dark states*. The level structure of the optically allowed transitions

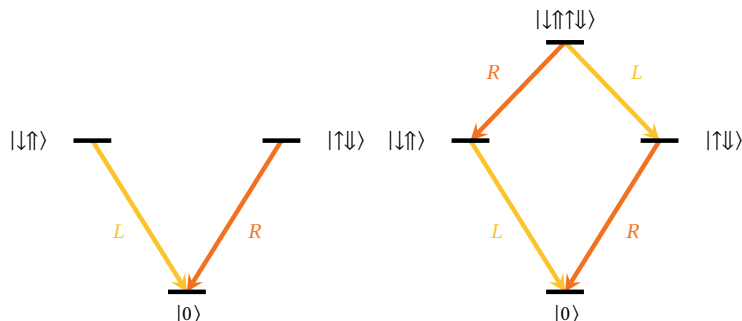


Figure 2.5: First is the level diagram of the bright exciton leading to circularly polarized photons, when decaying. Second is the level diagram corresponding to two excitons in a quantum dot forming a biexciton.

which we call the *bright exciton* is illustrated in figure 2.5. The bright exciton couples to the dark exciton via a spin flip of the electron, and while in this state no emission is seen. Another spin flip can occur and it comes back into the bright exciton state and can recombine by emission of a photon, a phenomenon known as *blinking*.

In addition to the exciton states, a higher energy state consisting of two electron-hole pairs confined in the same quantum dot exist, known as the *biexciton*. The binding energy of the biexciton is lower than the exciton recombination energy, due to the Coulomb force between the two electrons. Determined by Pauli's exclusion principle only two electrons of opposite spins are allowed in the same state, and thus a single biexciton state exists $|\uparrow\uparrow\downarrow\downarrow\rangle$. The bright exciton and the biexciton are the central quantum dot transitions considered in this thesis work.

Finally, charged states are also possible, where one extra electron or hole is added to the exciton states, but since these are not studied in this thesis, the details can be found in reference Warburton, 2013.

The pure energy diagram of the exciton and biexciton in figure 2.5, where the exciton states are degenerate is hard to achieve in practice, and requires a full overlap of the electron and hole wavefunction. Any anisotropy in the confinement potential will decrease the overlap. For example the excess strain from the growth process of self-assembled quantum dots leads to elongation of the quantum dot shape, which prevents the electron and hole wave functions from fully overlapping. This effect is much smaller in the symmetric droplet etched quantum dots. The effect on the energy level structure is that the degeneracy of the exciton states is lifted by the fine structure splitting S , and form new superposition bright exciton states as shown in figure 2.6. These superposition states are now addressed with linear polarization and the circular photon basis is no longer the good eigenbasis⁽²⁾. The two linear dipoles are referred to as the X and Y dipole. The orientation of the dipole moment is defined during the growth where the strain profile is induced along the crystallographic axes. This means

(2) Linear polarization is just a superposition of circular polarizations (and vice versa)

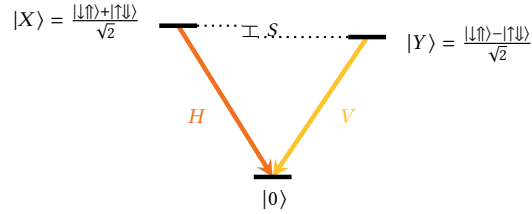


Figure 2.6: Energy level diagram of the bright exciton. Here the degeneracy of the exciton levels are lifted by the fine structure splitting S , which leads to linear polarization of the emission.

that on the final sample ideally all linear dipoles are oriented along one of two axes separated by 90° , except for local variations.

2.4 CONTROL OF THE QUANTUM DOT CHARGE ENVIRONMENT

In this section, we explain how to introduce a tuning knob of the quantum dot emission by applying a constant electric field across the quantum dots, which simultaneously control the noisy charge environment.

The semiconductor environment of the quantum dot can lead to random additional charges, e.g. due to impurities in the material, or by scattering an electron from the wetting layer or the bulk material, into the quantum dot. An additional charge confined in the quantum dot leads to a shift of the emission energy. If electrons scatter in and out of the quantum dot confinement well, they repeatedly modify the electronic environment leading to noise in the neutral exciton transition. By applying a constant electric field and thereby controlling the electron flow, random charge scattering can be suppressed.

A constant electric field can be created across the quantum dots, by embedding them in the center of a diode structure. The quantum dots are grown in the center of a GaAs membrane, where p - i - n diode can be made directly during the GaAs growth. This is done by altering the doping content to make a heterostructure of different GaAs dopants, as illustrated in figure 2.7(a). Further, an AlGaAs barrier is added in the i region to prevent current flow in the membrane. The electronic potential difference between the p (positive) and n (negative) layer leads to a constant intrinsic electric field across the membrane. The strength of the field determines the steepness of the slope of the CB (and VB), where for simplicity, only the CB is shown, but the VB shifts accordingly. The constant electric field can be changed by applying an external field, changing the slope of the CB, as illustrated in figure 2.7(b). The field is applied using an external bias voltage through metal contacts deposited on the n and p layer.

The Fermi level of the diode structure is defined by the electron-rich n layer. The i region between the quantum dot layer and the n -doped layer forms a barrier between the quantum well and the reservoir of electrons. At 0 bias field, due to the slope of the band, the high tunnel barrier is preventing electrons to enter the quantum dot. As the

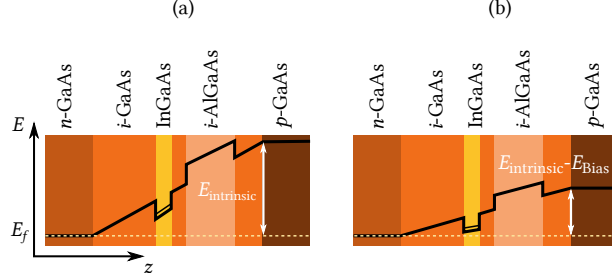


Figure 2.7: (a) p - i - n diode structure in the quantum dot membrane. The doped layers introduce an intrinsic constant electric field $E_{\text{intrinsic}}$, which shift the conduction band. (b) Same as in (a) but the case where an external bias field is applied E_{bias} , to modify the slope of the conduction band.

bias field is applied and the slope decreases less energy is required to cross the barrier and an exciton is allowed to be trapped. The tunneling of additional charges is hindered by the Coulomb blockade. If the applied bias field is increased further, the quantum dot can be shifted below the Fermi level, where the tunneling of an additional electron is energetically favorable. In this way, the charged states can be deterministically populated (Warburton, 2013). In summary, the doped membrane allows very stable control of the charge environment, preventing unwanted additional charges to scatter into the quantum dot.

The possibility of applying an external electric field also allows tuning of the quantum dot emission energy via the Stark effect. This leads to a so-called voltage plateau, which is a range of voltages where the quantum dot emission energy tunes with applied voltage, until emission abruptly shift to the next energy level where it is populated by an additional charge. The tuning range depends on the growth and can be optimized and to some degree regulated. The sample investigated in this thesis has a tuning range of ~ 0.2 nm for the neutral exciton. Tuning of the emission energy opens the possibility to tune the quantum dot into resonance with e.g. a cavity or another quantum dot. The electrical control further allows to effectively turn 'on' and 'off' the quantum dot in a highly convenient manner. This gives reliable background measurements and gives direct access to the single-photon impurity ξ (ratio of single photons to laser background photons) which will be much more thoroughly introduced later on.

Accurate tuning of the electrical field is crucial for deterministic control of the charge. To achieve this, high performance of the diode and of the deposited electrical contacts is crucial. For an ideal diode, the relation between the current I and the voltage V follow the Shockley equation

$$I(V) = I_0 \left(e^{eV/k_B T} - 1 \right), \quad (2.1)$$

where e is the electron charge, k_B is the Boltzmann constant and T is the temperature and I_0 is the saturation current. Measuring the I - V curve is an important sample characterization step, and will be described in section 4.3.

2.5 TWO-LEVEL EMITTER

The optical transition in a two-level emitter is ideal to employ as a single-photon source. As we have already seen above, the quantum dot consists of multiple levels, but by spectral filtering and selecting the polarization of excitation, it is possible to come close to this picture. In this section, we briefly introduce some concepts of the textbook description of a two-level emitter, move on to including dark state blinking effects using numerical solutions, and round off by outlining the dephasing mechanisms not described with these models.

2.5.1 Spontaneous emission of a two-level emitter

An exciton confined in a quantum dot will spontaneously recombine by the emission of a single photon. The spontaneous emission is a consequence of the coupling to a continuum reservoir of radiation modes ω_k and can be described by what is known as Wigner-Weisskopf theory for a two-level emitter. This is sketched in figure 2.8(a). We describe the two levels by the excited state $|e\rangle$ and the ground state $|g\rangle$, and the transition operators $\sigma_+ = |e\rangle\langle g|$ and $\sigma_- = |g\rangle\langle e|$. We assume that the emitter starts out in the excited state and vacuum in the radiation modes $|e\rangle|0\rangle$, and end up in the state $|g\rangle|1_k\rangle$, emitting a photon of frequency ω_k into the mode $|1_k\rangle$.

In the rotating wave approximation the system is described by the Hamiltonian

$$H = \hbar\omega_0\sigma_+\sigma_- + \hbar\sum_k\omega_k\left(a_k^\dagger a_k + \frac{1}{2}\right) - \hbar\sum_k\left(g_k\sigma_+a_k e^{i(\omega_0-\omega_k)t} + g_k^*\sigma_-a_k^\dagger e^{-i(\omega_0-\omega_k)t}\right), \quad (2.2)$$

where a_k and a_k^\dagger are the quantized field operators for each mode k , ω_0 is the quantum dot resonance frequency and g_k is the electric dipole matrix element i.e the light matter coupling strength $g_k = i\mathbf{E}_k \cdot \mathbf{d}_{eg}/\hbar$. We seek a solution that connects states $|e, 0\rangle$ to $|g, 1_k\rangle$ with a state vector of the form $|\psi(t)\rangle = c_e(t)|e, 0\rangle + \sum_k c_g(t)|g, 1_k\rangle$ and the amplitudes c_e and c_g . By time evolution, using the Schrödinger equation in the interaction picture, the equations of motion reads

$$\dot{c}_e(t) = -i\sum_k g_k e^{-i(\omega_k-\omega_0)t} c_g(t) \quad (2.3)$$

$$\dot{c}_g(t) = -ig_k^* e^{-i(\omega_0-\omega_k)t} c_e(t) \quad (2.4)$$

Under the initial conditions $c_g(0) = 0$ and $c_e(0) = 1$ and by integration and substitution we find that

$$\dot{c}_e(t) = -i\sum_k |g_k|^2 \int_{t_0}^t dt' e^{-i(\omega_k-\omega_0)(t-t')} c_e(t'). \quad (2.5)$$

There are many approaches forward here, but for the quantum dot semiconductor system, which later on will be embedded in a nanophotonic environment, it is

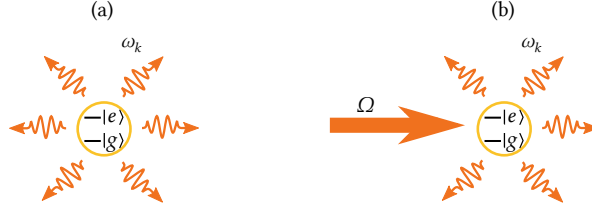


Figure 2.8: Illustration of the two level emitter cases that is treated in the main text. (a) Spontaneous emission. (b) Resonance fluorescence.

convenient to write the summation over the radiation modes k in terms of the local density of state (LDOS) $\rho_{\text{LDOS}}(\mathbf{r}, \omega, \hat{\mathbf{e}}_d)$. The LDOS specifies the number of optical states per volume available for an emitter with dipole orientation $\hat{\mathbf{e}}_d$ and frequency ω and location \mathbf{r} . It can be shown that (Lodahl et al., 2015)

$$\dot{c}_e(t) = -\frac{|\mathbf{d}_{eg}|^2}{2\varepsilon_0\hbar} \int_0^\infty d\omega \omega \rho_{\text{LDOS}}(\mathbf{r}, \omega, \hat{\mathbf{e}}_d) \int_{t_0}^t dt' e^{-i(\omega-\omega_0)(t-t')} c_e(t'), \quad (2.6)$$

where ε_0 is the vacuum permittivity.

We apply the Markov approximation, which assumes that $\omega \rho_{\text{LDOS}}(\omega)$ changes slowly over the linewidth of the emitter, such that the time integral can be moved outside the frequency, integration leading to a Dirac delta function in time. Since the time integral describes the memory of the system i.e. how much previous times t' affect $c_e(t)$, it implies that the radiation reservoir is memoryless. This leads to an exponential decay of the excited state

$$\dot{c}_e(t) = -\frac{\gamma}{2} c_e(t). \quad (2.7)$$

This exponential decay is spontaneous emission induced by the interaction with the reservoir, where the decay rate is

$$\gamma = \frac{\pi \mathbf{d}_{eg}^2}{\varepsilon_0 \hbar} \omega_0 \rho_{\text{LDOS}}(\mathbf{r}, \omega, \hat{\mathbf{e}}_d). \quad (2.8)$$

The rate at which the emitter decays is therefore highly dependent on the LDOS, which in case of a solid state quantum dot can be tailored by the introduction of nanophotonic structures.

2.5.2 Resonance Fluorescence

In the above, we have seen how the coupling between the emitter in the excited state and a continuum of reservoir modes, leads to spontaneous emission. In this section,

we include the driving field which brings the emitter into the excited state from where it spontaneously emits, as illustrated in figure 2.8 (b). This is *resonance fluorescence*, where we include the coherent driving of the laser field described by

$$H_{\text{coh}} = \hbar\Delta\sigma_+\sigma_- + \hbar(\Omega^*\sigma_- + \Omega\sigma_+). \quad (2.9)$$

Here Ω is the Rabi frequency of the driving field and Δ is the detuning between the laser and the two-level resonance frequency ω_0 . Resonance fluorescence is most conveniently described with the master equation formalism, where we choose to not keep track of all information about the reservoir since this is both very complicated and not necessary since we are essentially only interested in the system dynamics. The state of the system and reservoir (SR) is described by the density operator $\rho_{SR}(t) = |\psi(t)\rangle\langle\psi(t)|$ in the interaction picture, where the reservoir can be traced out, giving the reduced density operator $\rho(t) = \text{Tr}_R[\rho_{SR}(t)]$. The equation of motion, of the interaction picture reduced density operator, is given by the master equation. The master equation is also derived under the Markov approximation and the assumption of vacuum in the radiation continuum. The equation of motion is (Meystre & Sargent, 2007)

$$\dot{\rho}(t) = \frac{i}{\hbar}[H_{\text{coh}}, \rho(t)] + \mathcal{L}_\gamma(\rho(t)) + \mathcal{L}_{\gamma_{\text{dp}}}(\rho(t)), \quad (2.10)$$

where the Linblad terms $\mathcal{L}(\rho(t))$ accounts separately for the spontaneous emission decay γ and a second decay γ_{dp} describing dephasing of the system.

The equations of motion can be written out as $\langle i|\dot{\rho}|j\rangle = \dot{\rho}_{ij}$ where $i, j = \{g, e\}$ for all combinations, known as the *optical Bloch equations*

$$\begin{pmatrix} \dot{\rho}_{gg}(t) \\ \dot{\rho}_{ge}(t) \\ \dot{\rho}_{eg}(t) \\ \dot{\rho}_{ee}(t) \end{pmatrix} = \begin{pmatrix} 0 & i\frac{\Omega}{2} & -i\frac{\Omega^*}{2} & \gamma \\ i\frac{\Omega}{2} & \frac{-\gamma}{2} - \gamma_{\text{dp}} + i\Delta & 0 & -i\frac{\Omega}{2} \\ -i\frac{\Omega}{2} & 0 & \frac{-\gamma}{2} - \gamma_{\text{dp}} - i\Delta & i\frac{\Omega^*}{2} \\ 0 & -i\frac{\Omega}{2} & i\frac{\Omega^*}{2} & -\gamma \end{pmatrix} \begin{pmatrix} \rho_{gg}(t) \\ \rho_{ge}(t) \\ \rho_{eg}(t) \\ \rho_{ee}(t) \end{pmatrix}. \quad (2.11)$$

The introduced second decay rate is known as pure dephasing which describes the loss of coherence due to interaction with the environment. This evolution only affect the coherence terms (ρ_{eg} and ρ_{ge}), and hence has no effect on the population (ρ_{ee} and ρ_{gg}). We write the total decay rate $\gamma_{\text{tot}} = \gamma/2 + \gamma_{\text{dp}}$.

If the quantum dot is driven continuously i.e with a continuous wave (cw) laser we see the steady state solutions. In steady state, $\dot{\rho}(t) = 0$, it is straightforward to calculate the excited state population

$$\rho_{ee}(t \rightarrow \infty) = \frac{\Omega^2}{\gamma} \frac{\gamma + 2\gamma_{\text{dp}}}{4\Delta^2 + (\gamma + 2\gamma_{\text{dp}})(\gamma + 2\gamma_{\text{dp}} + 2\Omega^2/\gamma)}. \quad (2.12)$$

The excited state population is plotted as a function of laser detuning in figure 2.9(a), which shows a Lorentzian lineshape. In the low power limit the full width half maximum

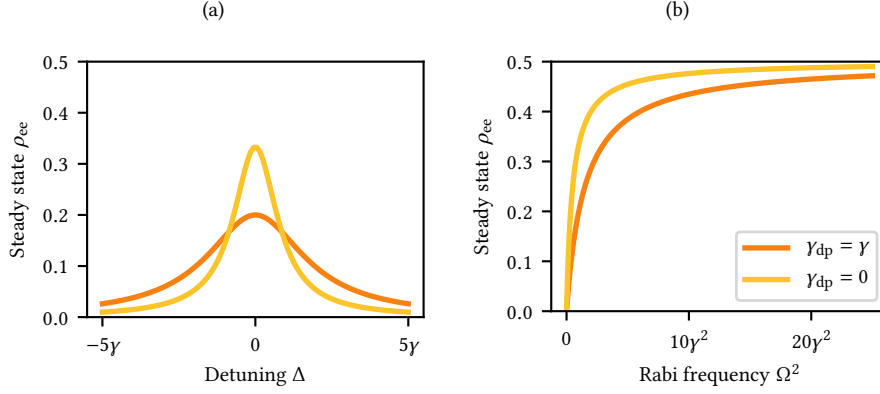


Figure 2.9: Steady state solutions to the optical Bloch equations. (a) The ρ_{ee} dependence of the laser frequency detuning Δ , showing a Lorentzian lineshape. (b) The Rabi frequency area Ωt dependence of the steady state solutions.

is $\Delta_{\text{FWHM}} = \gamma + 2\gamma_{\text{dp}}$, which shows how the presence of pure dephasing broadens the line shape. If no dephasing is present $\gamma_{\text{dp}} = 0$ the lineshape is defined by the radiative decay rate γ . With increasing Ω , the excited state population is asymptotically reaching 0.5 in steady-state, plotted in figure 2.9(b).

We will leave out the solution of the time dynamics of the excited state population, which leading to Rabi oscillations as a function of pulse area Ωt , where the excited state population reaches 1 at $\Omega t = \pi$ for $\gamma_{\text{dp}} = 0$ (Steck, 2007).

The coherence of the emitted photons is described by the first order correlation function $G^{(1)}(t, \tau) = \langle \sigma_+(t)\sigma_-(t+\tau) \rangle$. This correlation of the field at different times can be used to calculate the emission spectrum (Meystre & Sargent, 2007). Another important characteristic of resonance fluorescence that will be studied experimentally later in this thesis, is the second order correlation function

$$G^{(2)}(\tau) = \langle \sigma_+(t)\sigma_+(t+\tau)\sigma_-(t+\tau)\sigma_-(t) \rangle, \quad (2.13)$$

describing the probability of detecting a photon both at time t and $t + \tau$. The two-time correlation function can be calculated from the solution of the Bloch equations, using the quantum regression theorem. To understand the principle we look at the expectation value of a system operator

$$\langle A(t) \rangle = \text{Tr}[A(t)\rho_{\text{SR}}] \quad (2.14)$$

which in the Schrödinger picture is

$$\langle A(t) \rangle = \text{Tr}[AU(t, 0)\rho_{\text{SR}}U^\dagger(t, 0)] = \text{Tr}_S[A\rho(t)]. \quad (2.15)$$

The quantum regression theorem states that the expectation value at different times is

$$\langle A(t)B(t+\tau) \rangle = \text{Tr}_S[BA(t+\tau)], \quad (2.16)$$

where the two time operator is given by $\Lambda(t+\tau, t) = \text{Tr}_R[U(t+\tau, t)\rho_{SR}(t)AU^\dagger(t+\tau, t)]$. This means that the expectation value of the two-time correlation operator satisfies the same equations of motion as the single time expectation value does⁽³⁾, and hence the matrix system of the optical Bloch equations can be used to solve the two-time correlation. The results of this calculation can be found in eg. (Meystre & Sargent, 2007; Steck, 2007). Physically, the second-order correlation function describes how pure the emitted single photons are, revealing if multi-photon events occur. The experimental implementation will be discussed in more detail in section 5.6.

Numerical Solution to Bloch Equations

Analytical calculation of the time dynamics is possible for cw excitation. However, as will be explained later on, we would like to study the fluorescence under pulsed excitation enabling triggering of the emission. This complicates the calculations further, but we can instead solve the Bloch equations numerically to calculate the time dynamics and the spectrum⁽⁴⁾. Pulsed excitation is modeled with a Gaussian envelope in time, such that the Rabi frequency entering the Bloch equations is now

$$\Omega(t) = \frac{\Omega_0}{\sqrt{2\pi}\sigma} e^{-(t-t_0)^2/\sigma^2}, \quad (2.17)$$

where Ω_0 is the pulse area, σ is the width of the pulse and t_0 is the center in time. Numerical solutions to the Bloch equation can be very useful for modeling the real physical system. By including extra states to the Bloch equations the corresponding time dynamics can be found.

2.5.3 Modelling of the Effect of Dark States on Single-photon Emission

A real quantum dot shows deviations from the ideal two-level case. In our experiments, we typically see the existence of a dark state (the dark exciton), which can be incorporated into the model as a third level.

We can include the dark state similar to (Johansen et al., 2010). Only the bright state couples to the ground state optically, and the dark state decays with the non-radiative rate γ_d . We introduce a scattering rate between the bright and dark exciton γ_{bd} which we assume to be the same in both directions and as depicted. The level diagram and the corresponding decays are illustrated in figure 2.10.

We include this additional state ρ_{dd} , which is not optically driven and can be described by the following modification of the Bloch equations,

(3) Which also corresponds to the Markov approximation

(4) By the Fourier transform.

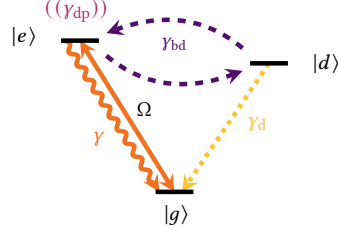


Figure 2.10: Three level diagram, including a dark exciton state $|d\rangle$ in addition to the bright exciton excited state $|e\rangle$ and the ground state $|g\rangle$. All decay rates and coupling terms included in the model of equation 2.18 are illustrated.

$$\begin{bmatrix} \dot{\rho}_{gg}(t) \\ \dot{\rho}_{ge}(t) \\ \dot{\rho}_{eg}(t) \\ \dot{\rho}_{ee}(t) \\ \dot{\rho}_{dd}(t) \end{bmatrix} = \begin{bmatrix} 0 & i\frac{\Omega(t)}{2} & -i\frac{\Omega(t)}{2} & \gamma & \gamma_d \\ i\frac{\Omega(t)}{2} & -\frac{\gamma}{2} - \frac{\gamma_{bd}}{2} - \gamma_{dp} + i\Delta & 0 & -i\frac{\Omega(t)}{2} & 0 \\ -i\frac{\Omega(t)}{2} & 0 & -\frac{\gamma}{2} - \frac{\gamma_{bd}}{2} - \gamma_{dp} - i\Delta & i\frac{\Omega(t)}{2} & 0 \\ 0 & -i\frac{\Omega(t)}{2} & i\frac{\Omega(t)}{2} & -\gamma - \gamma_{bd} & \gamma_{bd} \\ 0 & 0 & 0 & \gamma_{bd} & -\gamma_d - \gamma_{bd} \end{bmatrix} \begin{bmatrix} \rho_{gg}(t) \\ \rho_{ge}(t) \\ \rho_{eg}(t) \\ \rho_{ee}(t) \\ \rho_{dd}(t) \end{bmatrix}. \quad (2.18)$$

For a given set of parameters $\{\gamma, \gamma_{dp}, \gamma_{bd}, \gamma_d, \Omega_0, \sigma, \Delta\}$ these equations of motions can be solved numerically. The numerical solution is found using MATLAB's implementation of Runge-Kutta (4,5) solver `ode45`. Using the quantum regression theorem, the second-order correlation function can be calculated, and compared or fitted to experimentally observed values, by keeping some parameters as free fit parameters. It was briefly mentioned in the introduction that we typically use a spectral filter to selectively collect photons in a narrow spectral window. Spectral filtering has a large impact on the observed values of the second-order coherence function and can be included in the numerical solution from the first-order coherence function as already mentioned.

2.5.4 Contributions to the Spectral Linewidth of Quantum Dot Emission

The emission spectrum of an ideal two-level emitter has a linewidth limited by the radiative lifetime of the transition $\Gamma_0 = \gamma/2\pi$. Due to decoherence induced by the solid-state environment, this limit is hard to reach in practice for quantum dots. This is one of the challenges when using solid-state systems as single-photon sources. Dephasing or decoherence induced by noise in the solid-state environment have different origins. We briefly here introduce the two main contributions for the neutral exciton.

Starting with the already introduced pure dephasing. Pure dephasing is mainly caused by phonons, vibrational modes in the solid-state material. The interaction between a quantum dot and phonons at time-scales that comparable or faster than the radiative decay time⁽⁵⁾ leads to broadening of the emission line. This interaction is highly dependent on the dimensionality of the system. Therefore, introducing a nanostructure (which we do later in chapter 3) leads to a contribution to this effect depending on the type structure. This is studied in detail in Tighineanu et al., 2018. Recently in Dreessen et al., 2019 an approach to overcome this is presented, where vibrational modes in a nanostructure are clamped using a cladding of low refractive index material which can dampen the phonon modes.

Phonons also interact with quantum dots on a much shorter time scale, through inelastic scattering with the bulk phonons of the material. Mediated by a phonon the quantum dot can be excited to a higher level state, which leads to rapid photon emission at a few picosecond time scales. The fast decay time leads to a broad emission spectrum around the exciton transition, known as the phonon sideband. The phonon sideband is easy to spectrally filter and effectively just leads to losses of 5%–10%, and not broadening of the emission line.

The second process *spectral diffusion* enters differently. Is not described by the optical Bloch equations written above, but has a significant contribution to exciton linewidth broadening. The origin of this broadening is charge noise in the solid-state environment around the quantum dot. Noise in the electronic charge environment leads to shifting of the quantum dot resonance due to the Stark effect. This charge noise is slow, typically on the millisecond time scale, which leads to line broadening over the relevant time scales when using the exciton as a single-photon source. This noise is significantly reduced by the introduction of a *p-i-n* diode structure as described in section 2.4, and will further be a topic again in section 5.5.

When talking about decoherence processes in a quantum dot, typically the spin noise is also mentioned. The spin noise stems from the spin-orbit coupling to a fluctuating magnetic field (Overhauser field), originating from fluctuations in the nuclear spins of the bulk material. It has been shown to have very little effect on the neutral exciton in (Kuhlmann et al., 2013), but is crucial for experiments probing the spin using the charged states.

2.6 MULTIPHOTON EMISSION FROM THE BIEXCITON

In the last section of this chapter, we will focus on multiphoton emission from a quantum dot biexciton. The biexciton denoted $|XX\rangle$ decays through a cascade with the neutral exciton $|X\rangle$ as an intermediate state, and results in the emission of two photons. This system is interesting as a single-photon source since it allows coherent excitation that is not strictly resonant with any of the emission wavelengths of the photons. This will be further explained and discussed in section 6.2. Secondly, the two decay channels in the cascade is widely studied as a source of polarization-entangled

(5) Typically 100 ps–1 ns.

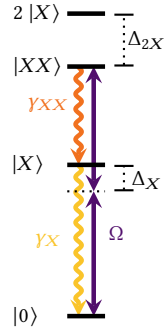


Figure 2.11: 3 level cascade system using only one branch of the biexciton decay. This diagram illustrates the dynamics modelled in equation 2.19.

photons (D. Huber et al., 2017; T. Huber et al., 2014; Hudson et al., 2007; Zeuner et al., 2019).

2.6.1 Three Level Cascade Solution to Bloch Equations

By selecting one of the two emitted photons, the biexciton can be used as a single-photon source. The main advantage of this scheme is that it can be driven using a two-photon excitation process, which means that the excitation laser frequency is detuned from both the X and XX transitions. This process is described by the level diagram displayed in 2.11, where only the decay through one dipole is considered. This three-level cascade is described by the Bloch equations of the form

$$\begin{bmatrix} \dot{\rho}_{0,0}(t) \\ \dot{\rho}_{0,X}(t) \\ \dot{\rho}_{X,0}(t) \\ \dot{\rho}_{X,X}(t) \\ \dot{\rho}_{XX,X}(t) \\ \dot{\rho}_{XX,XX}(t) \\ \dot{\rho}_{0,XX}(t) \\ \dot{\rho}_{XX,0}(t) \end{bmatrix} = M \begin{bmatrix} \rho_{0,0}(t) \\ \rho_{0,X}(t) \\ \rho_{X,0}(t) \\ \rho_{X,X}(t) \\ \rho_{XX,X}(t) \\ \rho_{XX,XX}(t) \\ \rho_{0,XX}(t) \\ \rho_{XX,0}(t) \end{bmatrix},$$

where $M =$

$$\begin{bmatrix}
 0 & i\frac{\Omega}{2} & -i\frac{\Omega}{2} & \gamma_X & 0 & 0 & 0 & 0 & 0 \\
 i\frac{\Omega}{2} & \frac{-\gamma_X - 2\gamma_{dp}}{2} + i\Delta_X & 0 & -i\frac{\Omega}{2} & 0 & 0 & 0 & i\frac{\Omega}{2} & 0 \\
 -i\frac{\Omega}{2} & 0 & \frac{-\gamma_X - 2\gamma_{dp}}{2} - i\Delta_X & i\frac{\Omega}{2} & 0 & 0 & 0 & 0 & -i\frac{\Omega}{2} \\
 0 & -i\frac{\Omega}{2} & i\frac{\Omega}{2} & -\gamma_X & i\frac{\Omega}{2} & -i\frac{\Omega}{2} & \gamma_{XX} & 0 & 0 \\
 0 & 0 & 0 & i\frac{\Omega}{2} & \frac{-\gamma_X - \gamma_{XX} - 2\gamma_{dp}}{2} - i\Delta & 0 & -i\frac{\Omega}{2} & -i\frac{\Omega}{2} & 0 \\
 0 & 0 & 0 & -i\frac{\Omega}{2} & 0 & \frac{-\gamma_X - \gamma_{XX} - 2\gamma_{dp}}{2} + i\Delta & i\frac{\Omega}{2} & 0 & i\frac{\Omega}{2} \\
 0 & 0 & 0 & 0 & -i\frac{\Omega}{2} & i\frac{\Omega}{2} & -\gamma_{XX} & 0 & 0 \\
 0 & i\frac{\Omega}{2} & 0 & 0 & -i\frac{\Omega}{2} & 0 & 0 & \frac{-\gamma_{XX} - 2\gamma_{dp}}{2} + i\Delta_{2X} & 0 \\
 0 & 0 & -i\frac{\Omega}{2} & 0 & 0 & i\frac{\Omega}{2} & 0 & 0 & \frac{-\gamma_{XX} - 2\gamma_{dp}}{2} - i\Delta_{2X}
 \end{bmatrix} \quad (2.19)$$

and we have defined $\Delta = \Delta_X - \Delta_{2X}$.

This can again be numerically solved to calculate the second-order coherence function, to see the time dynamic of the cascaded decay. We return to this topic in section 6.2, where we experimentally drive the two-photon transition and study the single-photon properties of the emitted photons.

2.6.2 Entanglement from the Biexciton

The biexciton decay was introduced in section 2.3 (see figure 2.5). If the two decay channels are indistinguishable, the emitted photons will be entangled in polarization $|\Psi\rangle = |RL\rangle + |LR\rangle$. As we saw, the presence of a fine structure splitting S changes this picture, and the full biexciton decay diagram can be represented in different bases, as illustrated in figure 2.12. In the linear basis, S leads to the energy splitting of the exciton state, while representing the system in circular polarization basis leads to spin flips between the two degenerate exciton states at a rate defined by it.

Starting with the linear basis shown in figure 2.12(a), then the emitted two-photon state will be entangled in polarization

$$|\Phi\rangle = \frac{1}{\sqrt{2}} \left(|H_{XX}H_X\rangle + e^{i\phi} |V_{XX}V_X\rangle \right), \quad (2.20)$$

where the phase $\phi = St/\hbar$ is accumulated while the quantum dot is in the exciton state. Equation 2.20 does not represent a maximally entangled Bell state if the fine structure splitting is non-zero. The larger the value of S the more it deviates from a maximally entangled state, and therefore one obvious approach to overcome this is to use quantum dots optimized to have minimal fine structure splitting such as droplet-etched quantum dots, introduced in section 2.2.2. This approach is taken in e.g. (D. Huber et al., 2017; Liu et al., 2019; H. Wang, Hu, et al., 2019).

The accumulated phase ϕ over the time that the quantum dot spends in the exciton state is essentially a time average. We can instead consider the time dynamics of the decay by considering the circular polarization basis. The emitted two-photon state, in

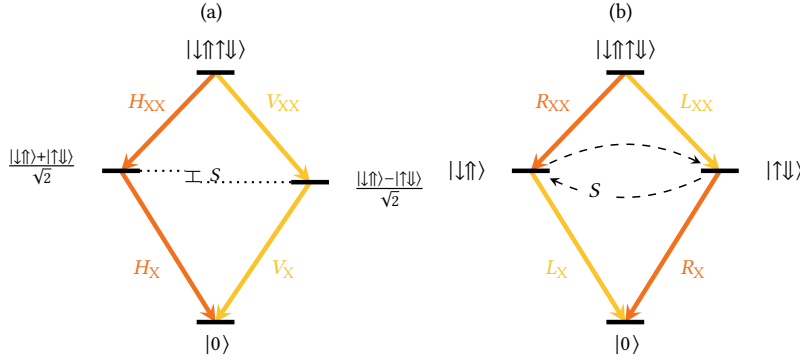


Figure 2.12: Biexciton level diagrams. (a) 4 level decay system of the biexciton including a fine structure splitting S in the linear basis. (b) 4 level decay system of the biexciton including a fine structure splitting S in the circular basis, leading to oscillations between the exciton states.

this case, oscillates between states

$$|\Psi\rangle = \frac{1}{\sqrt{2}} \left(|R_{XX}L_X\rangle + |L_{XX}R_X\rangle \right) \quad (2.21)$$

$$|\Phi\rangle = \frac{1}{\sqrt{2}} \left(|R_{XX}R_X\rangle + |L_{XX}L_X\rangle \right), \quad (2.22)$$

at the rate S . This time dependence of the entanglement is discussed in chapter 7, where a tomographic measurement of a biexciton polarization-entangled state is performed. Fast detection equipment is required to resolve these oscillations unless the fine structure splitting is very low. In chapter 8 we study how this oscillating entangled state couples and is preserved in a planar nanophotonic structure.

In this chapter, we have established how quantum dots can be used as a single-photon source as well as polarization-entangled sources. Starting from the fundamental aspect of forming a quantum dot from a heterostructure of two semiconductors and moving on to how to add tuning and control of the emission properties. We have introduced optical models describing the emission, based on different level schemes.

As mentioned in the very beginning of the chapter, a great advantage of quantum dots is that they are embedded in a solid material, with no need for trapping. In the next chapter, we are going to see how patterning a nanophotonic structure directly in the material around the quantum dot, leads to further advantageous properties. Nanophotonic structures enable both enhancement of the emission, and to efficiently extract the single photons.

CHAPTER



NANOPHOTONIC STRUCTURES FOR DETERMINISTIC GENERATION OF PHOTONS

Presentation of different approaches to nanophotonic structures followed by an introduction to the approach in this thesis; a photonic crystal waveguide with shallow-etched grating outcouplers.

In this chapter, we are going to see how modification of the photonic environment around a quantum dot can be designed to efficiently collect the emitted photons and enhance the emission rate. The most classical example of enhanced emission is an atom in a resonant optical cavity, where the number of available modes that the atom can decay into is suppressed, and hence the emission into specific modes is enhanced. This was first suggested by Purcell, 1946 for a magnetic resonance. The radiative decay rate of the emitter γ_{rad} in the cavity environment is enhanced compared to the decay rate in a homogeneous medium $\gamma_{\text{hom,rad}}$ by the Purcell factor

$$F_p = \frac{\gamma_{\text{rad}}}{\gamma_{\text{hom,rad}}}. \quad (3.1)$$

For solid-state emitters such as quantum dots, the interaction with the embedding environment introduces noise which leads to dephasing, as was briefly explained in the previous chapter. On the other hand, nanophotonic structures can be fabricated directly into the solid-state material and can be designed to Purcell enhance the emission. By enhancing the decay rate, the interaction time with the noisy environment is shortened. Distributed Bragg reflectors (DBRs), nanophotonic cavities e.g. in form of vertical micropillars (Ates et al., 2009; Ding et al., 2016; Somaschi et al., 2016; Unsleber et al., 2016) can be patterned around the quantum dot to reach high Purcell factors. Another

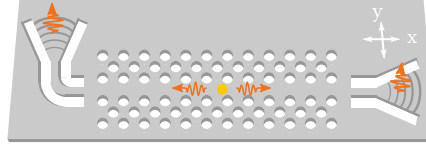


Figure 3.1: Sketch of a device similar to that used for the majority of the thesis work. A photonic crystal waveguide, which collects the emitted photons from the quantum dot, and guides the photons to the shallow etched grating out couplers.

approach to suppress the available optical modes for the quantum dot is to place it inside the bandgap of a planar photonic crystal.

As mentioned, nanophotonic structures do not only serve the purpose of enhancing the emission but also to efficiently couple the emitted photons into a well-defined optical mode, that can be collected in an optical fiber. From a planar bulk wafer i.e. with no nanostructures the collection efficiency using microscope objective is limited to around $< 1\%$, since the quantum dot will emit into all directions above the sample and only a small fraction can be captured by the objective. For on demand single-photon generation, we have to collect photons at much higher efficiencies. There are many approaches to this, and it is worth establishing a small overview of some of the most classical ones, in order to compare with the structures used in this work. In the single-photon experiments performed in this thesis work we employ a *photonic crystal waveguide* in a suspended membrane as sketched in figure 3.1. The quantum dots are located at the center layer of the membrane, and couples to the waveguide along the x axis seen in the figure. We fabricate the waveguide along one of the crystallographic axes defined during the growth, such that the dipole orientations are aligned with either x or y in figure 3.1. The waveguide coupled emission is scattered using *Shallow-etched grating couplers* terminating the waveguide in each end. We start this chapter out by giving a brief introduction to some other approaches using different nanostructures.

3.1 APPROACHES FOR MODIFYING THE PHOTONIC ENVIRONMENT

To appreciate the strengths of the photonic crystal waveguide as a single-photon device, we present a brief overview of some alternative approaches to modifying the photonic environment. The selected approaches are not meant to be exhaustive, and there are indeed many more than the four that are presented here. The aim is to give a brief conceptual overview of their performances with some pros and cons. The four selected approaches are displayed in figure 3.2. The quoted number is the first lens efficiency η_{lens} , which means how much light will reach the first optical component after exiting the sample.

The first structure presented is a *Nanowire*, which collects emitted photons into a tapered waveguide that efficiently couples the photons to an out-of-plane propagating mode. The nanowire is simple to fabricate at a predetermined position by placing a nanoparticle on a substrate, where the core of the nanowire is grown epitaxially.

The growth conditions can hereafter be controlled to be axial which forms a cladding around the core. This together makes a nanophotonic waveguide pointing out-of-plane for free space coupling. A few layers during the core growth can be replaced with another semiconductor material to form the quantum dot, typically InAsP (Indium Arsenic Phosphite) inside InP. Quantum dots grown in a nanowire have high radial symmetry, and therefore low fine structure splitting. By tapering of the nanowire tip, it is possible to design the free space mode to match the Gaussian collection mode of a fiber. A fiber coupling efficiency as high as 93 % has been reported (Bulgarini et al., 2014). The simplicity, low fine structure, and potentially almost unity extraction efficiency makes the nanowire highly appealing for single-photon sources (Reimer et al., 2012). High indistinguishability of single-photons from a nanowire has though not yet been demonstrated, possibly due to charge noise on the surface of the nanowire. The nanowire has no immediate possibility to integrate charge control. Nonetheless, it is a popular platform for polarization entanglement from the biexciton (T. Huber et al., 2014; Jöns et al., 2017; Prilmüller et al., 2018), and exactly this platform will be used in chapter 7.

Secondly, a *vertical micropillar cavity* is presented which is one of the most widely used for single photon generation (Ates et al., 2009; Ding et al., 2016; Somaschi et al., 2016; Unsleber et al., 2016). Micropillars are etched out of a thick epitaxially grown substrate with quantum dots grown in the central layer. DBRs can be created below and above the quantum dot by growing thin layers of alternating refractive index as seen in figure 3.2, to form a cavity. By making one of the DBR's semi-transparent, photons exit the cavity there, and are guided out-of-plane by total internal reflection on the pillar sides. Micropillars provide both high extraction efficiencies and strong Purcell enhancement. Charge control has been implemented (Somaschi et al., 2016) and is one of the leading candidates as a device for single-photon sources. A shortcoming in the micropillar design is that excitation and collection modes are overlapping, and they need to be operated in a cross polarized configuration. In general cavity nanophotonic structures has a disadvantage since coupling of photon is only possible in a narrow resonance frequency region, which is also the case for the last two cavity design. Two micropillars, forming micro-pillar-molecule allows tuning of the resonance frequency of the system and support multiple polarizations which is crucial for biexciton entanglement (Dousse et al., 2010).

Using a *microcavity*, remarkably high efficiencies has been reported very recently in the preprint Tomm et al., 2020. The microcavity consist of a bottom DBR mirror similar to the micropillar, but no with no etching step. The top mirror is external and is placed on top of the sample. It is fabricated in of fused silica with a micromachined curved surface to focus the emission into a highly Gaussian out of plane mode. Further, in this cavity design light matter interaction in the strong coupling regime is reached (Najer et al., 2019). Charge control is easily integrated in the sample heterostructure, and has a great advantage that no post fabrication is required. This new design has high potential for applications as a single-photon source. Another widely used design is a cavity formed by two DBR mirrors around the quantum dot layer, and a solid immersion lens on top of the sample to focus the emission. Here the extraction efficiency is typically

Struct.	Nanowire	Micropillar	Microcavity	Bulls-eye cavity
Ref.	Claudon et al., 2010	Ding et al., 2016	Tomm et al., 2020	H. Wang, Hu, et al., 2019
η_{lens}	35 %	66 %	82 %	48 %

Figure 3.2: Overview of different often used approaches to modifying the nanophotonic environment. The quoted efficiency η_{lens} is from references and is the first lens efficiency. There is no scale bar for the microcavity, but the full image width is around $10 \mu\text{m}$.

low, but has been employed for entanglement generation (D. Huber et al., 2018; Zeuner et al., 2019).

The final design that we consider here is the *Bulls-eye cavity*, which is a planar photonic cavity formed by rings around the quantum dot. The rings are created by etching ridges in a semiconductor on top of a silicon substrate. This design has recently shown excellent performance for biexciton entanglement, with high generation and extraction efficiencies (Liu et al., 2019; H. Wang, Hu, et al., 2019).

The common feature of all the discussed nanophotonic designs is that the quantum dot is excited directly from above, i.e. using the same spatial mode as the collection optical mode of the single-photon emission. Under resonant excitation, this means that it is hard to suppress the excitation laser background in comparison to the single-photon emission. The most common method to circumvent this is to cross-polarize the excitation and collection modes, which can give very high laser suppression. This in turn means that both collection and excitation mode can never be aligned with the dipole orientation, which lowers the excitation and extraction efficiency⁽¹⁾. In this context, planar waveguide nanostructures have a huge advantage since the collection and excitation modes can be spatially separated, as we will see in the next sections.

3.2 PHOTONIC CRYSTAL WAVEGUIDES

In this section, the main characteristics of the type of photonic crystal waveguide used in this thesis will be presented. Going into full details is beyond the scope of this thesis, and for more through description one can consult the references given throughout the next sections.

As discussed in the introduction, the radiative decay rate of a quantum dot scales with the number of modes it can emit into. This is in fact exactly what we calculated in equation 2.6 where we saw that the spontaneous emission rate is proportional to the

(1) In both nanowires and micropillars excitation from the side has also been used to overcome this, but it requires a second focusing objective

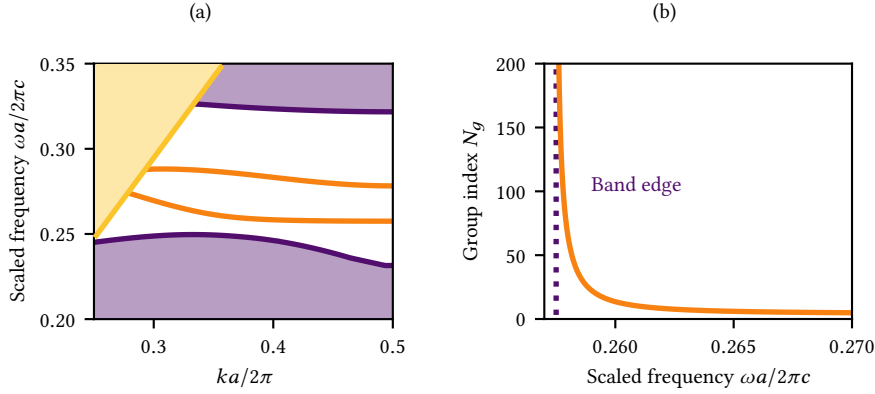


Figure 3.3: Band diagram of photonic crystal waveguide from simulation (Javadi et al., 2015). (a) Dispersion relation of allowed photonic bands. Slab modes are shaded in purple and the light cone from out of plane confinement by total internal reflection is shaded yellow. The dispersion relation of the three TE-like waveguide modes are plotted in orange. (b) Group index n_g for the lowest waveguide mode, which has a group velocity approaching 0, leading to dramatic increase of n_g towards the band edge. Credit for the simulations to Nils Hauff.

local density of states (LDOS). Instead of using a cavity, the LDOS can efficiently be modified using a photonic crystal, with a photonic bandgap where no modes are allowed. A photonic crystal is formed by a modulation of the refractive index with a period comparable to the optical wavelength, which modifies the electric field distribution and hence the supported modes (Joannopoulos et al., 2011). If an emitter is spectrally located within the photonic bandgap the emission will be inhibited, and it will in the ideal case not decay. We use a 2D slab photonic crystal, which is fabricated by perforating a suspended semiconductor membrane creating holes in a periodic a triangular lattice as shown in figure 3.1. This is particularly convenient since the quantum dots can be directly grown in this membrane before the photonic crystal fabrication. The size of the holes etched into the membrane, their separation and the lattice structure, the thickness of the membrane, together with the refractive index of the materials, determine the photonic band structure and hence the bandgap frequencies. A propagating waveguide mode can be introduced in the band diagram by removing a row of holes in the photonic crystal, forming a *photonic crystal waveguide* PCW. The resulting band diagram is shown in 3.3(a), with dispersion relation of the modes $\omega = \omega(k)$, where k is the wave vector along the propagation direction, plotted in orange.

The band diagram is calculated numerically, with an eigenmode solver using the finite element software COMSOL. From the simulation, the geometry can be optimized to match the desired frequencies of the quantum dots. The purple shaded area represents the *slab modes* of the membrane, and the gap between them is the bandgap. Light is confined in the plane of the membrane by the photonic crystal, and out of plane by total

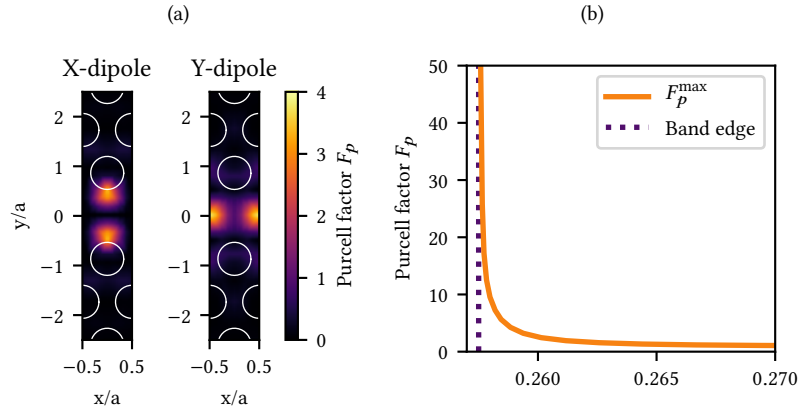


Figure 3.4: Purcell enhancement (a) Spatially dependent Purcell factor F_p in a unit cell of a PCW, for an X and Y-dipole, using a moderate group index of $n_g = 20$. (b) Maximal Purcell enhancement calculated from the group index in figure 3.3(a), and interpolated using the maximum value of simulations like (a) for different values of n_g . Data is simulations from (Javadi et al., 2018).

internal reflection on the interface with the surrounding air or vacuum. This appears as a light cone of radiation modes shaded in yellow in the band diagram. Towards the lower frequencies ($ka/2\pi \rightarrow 0.5$) of the low waveguide mode, appears a dramatic change in LDOS which abruptly becomes 0. We call this the *band edge* of the photonic crystal. The waveguide modes are highly dispersive, with a group velocity approaching zero in the band edge region $V_g(\omega) = \frac{d\omega}{dk} \approx 0$, and accommodate slow light. The slow down factor is determined by the group index $n_g(\omega) = c/V_g$, plotted in 3.3(b), which is proportional to the Purcell factor. For a GaAs membrane PCW, group indexes of $n_g \sim 50$ can be reached experimentally (Arcari et al., 2014). The full calculation of the Purcell factor is far more complex since it is also highly dependent on both the spatial location of the emitter within the waveguide and the overlap of the dipole moment of the emitter and the local polarization of the waveguide mode. Using the results from the full 3D numerical simulation in (Javadi et al., 2015), the spatially dependent Purcell factor is plotted in a unit cell of the PCW for two orthogonal dipole orientations in figure 3.4(a) for a moderate $n_g = 20$.

From figure 3.4(a), we can see that the amount of Purcell enhancement a dipole experience is not only dependent on its spatial location, but also on the dipole orientation since this changes the overlap with the waveguide mode electric field. Therefore, for a quantum dot located exactly in the center of the waveguide, the two dipoles from the neutral exciton can experience a very different amount of Purcell enhancement. The maximal Purcell factor can be expressed analytically assuming field maximum of the waveguide mode in a PCW and perfect dipole mode overlap, and is given by (Hughes,

2004; Lodahl et al., 2015)

$$F_p^{\max}(\omega) = \left(\frac{3}{2\pi n} \frac{\lambda^2/n^2}{V_{\text{eff}}/a} \right) n_g(\omega). \quad (3.2)$$

Here n is the refractive index, a is the lattice constant and λ is the wavelength. The effective mode volume $V_{\text{eff}} \sim (3\lambda^2/n^2)/(1/a)$ is almost constant in a PCW, which means that the main contribution to the Purcell factor lies in the group index,

$$F_p^{\max}(\omega) \approx \frac{1}{2\pi n} n_g(\omega). \quad (3.3)$$

In figure 3.4(b) the maximal achievable Purcell enhancement is plotted as a function of scaled frequency, which highlights that Purcell enhancement is also highly dependent on the spectral distance to the band-edge marked by the dotted line. In order to achieve Purcell enhancement, one should aim for quantum dot emitting at frequencies close to the bandgap, and select the Y dipole to have the most effect. However, operating at the band-edge is challenging, since it is difficult to distinguish single-photon emission from the steeply changing background, and often, we employ quantum dots with modest enhancements. As we will see in the next chapter, excellent single-photon properties can be reached in this regime as well. Operating spectrally further away from the PCW band-edge does not compromise the waveguide coupling efficiency, which is broadband. We will now take a closer look at this waveguide coupling and its spatial dependence.

3.2.1 Waveguide Coupling Efficiency: β -factor

By isolating the waveguide modes as seen in the band diagram in figure 3.3(a), emission at the corresponding frequencies will preferentially couple to those modes. This results in near-unity collection efficiency of single-photons into a single propagating mode. The emitter-waveguide coupling efficiency is quantified by the β -factor which is defined as

$$\beta = \frac{\gamma_{\text{wg}}}{\gamma_{\text{wg}} + \gamma_{\text{ng}} + \gamma_{\text{nrad}}}, \quad (3.4)$$

where γ_{wg} is the radiative decay rate of the emitter into the waveguide mode, γ_{ng} is radiative decay into non-guided modes, e.g. emission into the out of plane radiation modes overlapping with the frequency region, and γ_{nrad} is the non-radiative decay rate of the quantum dot. The β -factor is also highly spatially dependent on the LDOS and is computed numerically in (Javadi et al., 2018). The spatial dependence for the two orthogonal dipole orientations are plotted in figure 3.5(a), as well as a slice along the vertical axis in 3.5(b), in the center of the waveguide.

From the solid lines, we can see that the Y-dipole couples with near-unity efficiency at close to all locations along this slice, while the X-dipole has a negligible coupling to the waveguide mode. This can be exploited for single-photon sources where single dipole emission is preferred. Experimentally, near unity waveguide coupling of $> 98\%$ have been demonstrated in (Arcari et al., 2014).

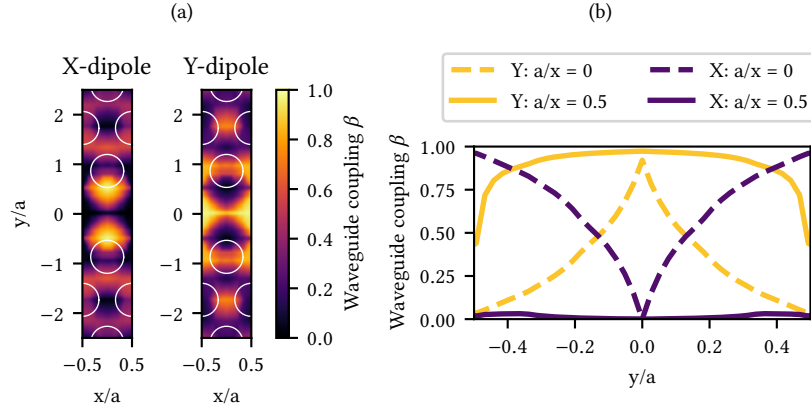


Figure 3.5: β factor (a) Spatial dependence of the β factor (for definition see main text) for an X and Y oriented dipole using $n_g = 20$ and assuming ideal dipole emission $y_{\text{nrad}} = 0$. (b) Cut-through (a) at a/x locations indicated in the legend. Data are a reprint of simulations from (Javadi et al., 2015).

3.2.2 Directional Coupling in Photonic Crystal Waveguide

In this section, we are going to take a closer look some areas in a PCW, where coupling of circular polarization is supported (Young et al., 2015). The circular coupling leads to an interesting property, which will be described below together with how the PCW geometry can be modified to maximize areas.

Following the dashed lines in figure 3.5(a), we see that at some locations slightly off-centered, both dipoles couple with equal β , meaning that circular polarization can be supported. These locations are rare in a PCW (only 0.8% of the waveguide area), and do not overlap with the field maximum, leading to weaker waveguide coupling (Coles et al., 2016). This can be overcome by modification of the PCW lattice geometry in a *glide plane waveguide* GPW (Lang et al., 2017).

We present here a brief summary of the GPW design, which is described in detail in Refs. Söllner et al., 2015 and Mahmoodian et al., 2017. In the PCW described above, a row of holes is removed, which makes it mirror-symmetric around the waveguide. Instead in a GPW, this symmetry is broken by shifting the photonic crystal on one side of the waveguide by half a lattice constant. This asymmetric geometry favours in-plane circular polarization of the guided modes. From time-reversal symmetry, two counter-propagating circularly polarized modes will have opposite helicity. This means that for an emitter placed inside the GPW with e.g. a left-hand circular dipole, it will couple unidirectionally to the left propagating mode, while the right-hand circular dipole will couple to the opposite propagation direction. Because of the coupling depending on the handedness of the polarization, this is referred to as *chiral points* and *chiral coupling*. In figure 3.6(a) the simulated band diagram of an optimized GPW geometry is displayed. We see two guided modes in the bandgap that overlap at the

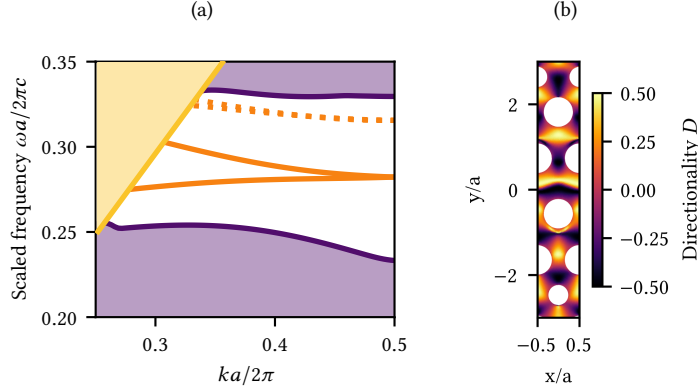


Figure 3.6: Band diagram of GPW (a) Dispersion relation from simulation of GPW. (b) Spatially dependent directionality D (see main text) in a unit cell of a GPW. The hole geometry shown is the one leading to the band diagram in (a), where rows of holes are shifted and shrunk to ensure single mode propagation in each direction (Mahmoodian et al., 2017). Credit for the simulations Nils Hauff.

band edge, and in this region it is possible to couple to both of them. The two modes represent the two counter-propagating modes, since they have opposite slopes for the dispersion.

In this glide plane geometry, almost all locations in the waveguide are circularly polarized with directional coupling. The design is optimized for maximal overlap of the chiral points with the field maxima for high β -factors. In figure 3.6(b) the spatially-dependent directionality defined as $D(\mathbf{r}) = (|\mathbf{E}(\mathbf{r}) \cdot \hat{\mathbf{e}}_L|^2 - |\mathbf{E}(\mathbf{r}) \cdot \hat{\mathbf{e}}_R|^2) / |\mathbf{E}(\mathbf{r})|^2$, where $\mathbf{E}(\mathbf{r})$ is the spatially-dependent electric field, and $\hat{\mathbf{e}}_L$ and $\hat{\mathbf{e}}_R$ are the circular unit vectors.

The GPW maintains the same advantageous properties as a regular PCW, in terms of β and F_p , but support chiral coupling of dipoles. In chapter 8 we are going to investigate how the biexciton cascade can benefit from being located in such a chiral point.

3.3 PLANAR INTEGRATION AND PHOTON OUTCOUPLING

In the above section, we have seen how the planar photonic crystal waveguide efficiently couple the single photons to an in-plane propagating waveguide mode. This allows for further integration with different devices on the same chip, photon routers, switches, phase shifters, filters, etc. (Bentham et al., 2015; Midolo et al., 2017; Papon et al., 2019; Shin et al., 2008; J. Wang et al., 2019). Routing and transportation of the photons on the chip is done using a simple suspended beam etched out of the membrane. We call this a *nanobeam waveguide*. A small section of nanobeam waveguide connects the PCW mode with the shallow etched grating outcouplers as sketched in figure 3.1.

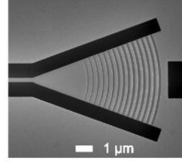


Figure 3.7: Scanning electron microscope image of a fabricated shallow etched grating outcoupler. Figure is from (Zhou et al., 2018).

3.3.1 Shallow-etched Grating Outcouplers

The in-plane propagating mode can be transferred out-of-plane by scattering via a grating structure. Traditionally, a simple second-order circular grating has been used to collect the photons from the chip as in e.g. (Arcari et al., 2014). While these circular gratings are easy to fabricate, the peak efficiency is limited to 10 %. Moreover, the circular gratings cause strong reflections back to the waveguide, thereby creating a weak resonator even when used with a waveguide (Hansen, 2017).

This was improved with the recently developed shallow etched gratings shown in figure 3.7 (Zhou et al., 2018), which was inspired by grating couplers used in silicon-on-insulator photonics (Roelkens et al., 2010). By etching the grating only partly through the membrane and optimizing the grating geometry such that the scattered mode has a slight angle with respect to sample normal, the back reflections can be fully suppressed. The pitch of the grating trenches defines the scattering angle θ and is given by $\Lambda = \lambda_0 / (n_{\text{eff}} - \sin(\theta))$. The waveguide mode is scattered to the out-of-plane propagating mode with $\sim 60\%$ efficiency (Zhou et al., 2018). This is the efficiency to be compared with the first lens efficiencies in figure 3.2, assuming no losses in the waveguide, which are typically $< 5\%$. A thorough loss characterization for a specific device will be presented in section 4.2. The profile of the scattered mode can be optimized to be nearly Gaussian ($M^2 < 1.5$), by varying the etch depth along the grating etches and is linearly polarized perpendicular to the waveguide. The light diffracted off the chip by the shallow-etched grating has been shown to couple into an optical fiber with an efficiency of $> 60\%$ (Zhou et al., 2018). Recent improvements in the sample design, which involves including a distributed Bragg reflector below the membrane has improved the scattering efficiency to $> 82\%$ (Uppu et al., 2020).

* * *

In this chapter, we have introduced the nanophotonic structure used in this thesis work, namely a PCW with shallow etched grating couplers, and discussed the key concepts. In contrast to the alternative approaches presented in section 3.1, we use planar structures. Planar structures allow interfacing the single-photon emission directly with integrated circuitry on the same chip. More importantly for this work, the spatially separated excitation and collection modes allow to efficiently suppress resonant later background

with no need to compromise on the laser polarization. Lastly, PCW works for a broad range of wavelengths in contrast to cavity designs.

Now that we have introduced the quantum dot as a single-photon emitter in chapter 2 and the device design employed to enhance and collect the single photons in this chapter, we are ready to take a look at the experimental setup, and characterization of a specific sample used to perform the single-photon measurements in chapter 5.

CHAPTER



OPTIMIZED EXPERIMENTAL DESIGN

Details of the experimental setup employed in this thesis, optimized and characterized to achieve high performance.

In the previous chapters, we have described the physical device which we use to generate, enhance, and collect the single photons, namely quantum dots embedded in a PCW. In order to realize an efficient single-photon source, it is necessary to supplement the excellent physical device with an optical experimental setup that is efficient and stable. A well thought-out design, optimization, and careful characterization of all components in the system is also crucial. If the setup suffers from too much loss or too much external noise, the intrinsic performance of the physical device cannot be resolved. To robustly characterize our devices, we therefore need a thorough understanding of the optical setup and losses, in order to decouple them from the device. This chapter first discusses all the optical components involved in single-photon generation. Subsequently, a thorough efficiency characterization of the setup and device is discussed. We round off by an electrical characterization of the *p-i-n* diode. This chapter is meant as a recipe that details the key aspects necessary to realize a scalable single-photon source that will be discussed in later chapters.

4.1 EXPERIMENTAL SETUP

The sample needs to be operated in a cold environment, to suppress phonon noise affecting the quantum dots. It is cooled to cryogenic temperatures, 1.6 K - 10 K, depending on the cryostat employed, and needs optical access to excite the quantum dot and collect the emitted single photons. The section is organized such that we start out with presenting the lasers we use for exciting the quantum dots, followed by a description

of the optical setup used both for directing the laser onto the sample and to collect the emitted single photons. After that, we present spectral filtering and detection equipment for the collected single photons.

Three different setups were used for the experiments in this thesis, all with slightly different excitation and collection designs. They share the same core components, but with different purposes and requirements in mind. In this chapter, we describe the setup that was used for the majority of the data presented in this thesis. This particular setup was rebuilt, thoroughly characterized, and optimized during this thesis work, with the result of high performance in both stability and efficiency.

4.1.1 Pulse stretching and excitation lasers

We primarily use two laser sources for exciting the quantum dot as shown in 4.1. One is a continuous wave (cw) diode laser⁽¹⁾ which has a narrow bandwidth of < 1 MHz. The cw laser is frequency locked using a wavemeter, with a resolution of 50 MHz. The laser has continuous mode-hop-free tuning over a spectral range of > 50 nm centered at 940 nm, which enables continuous scanning across the quantum dot resonances. The narrow bandwidth allows us to probe the linewidth of a quantum dot using resonant transmission or resonance fluorescence measurements, which will be discussed later.

To realize an on-demand single-photon source the quantum dot emission can be triggered by exciting the quantum dot with short laser pulses. An exciton is created when a quantum dot is excited by a laser pulse, which then decays to the ground state by emitting a photon. This ideally leads to a single photon emitted for each laser pulse at a rate defined by the laser pulse repetition rate. We use a mode-locked Ti:Sapph laser⁽²⁾, which outputs ~ 3 ps long laser pulses at a repetition rate of 76 MHz. The transform-limited frequency bandwidth of the pulses (assuming sech^2 pulses) is ~ 100 GHz. The quantum dot transitions that we address are much narrower, and therefore it can be beneficial to reduce the bandwidth. The impact of the excitation laser bandwidth on the source characteristics will be explained in more detail in chapter 6 but for now, we discuss a *pulse stretcher* setup employed for the tuning the pump laser bandwidth.

Pulse stretcher

The bandwidth of a laser pulse can be compressed in frequency, by in turn stretching the pulse in time, due to the constant time-bandwidth product. We call the setup to achieve this a pulse stretcher, and is sketched in figure 4.1. The pulse stretcher works the following way: The different frequency components of the 100 GHz wide laser pulse is dispersed using a diffraction grating. In our setup, we use a standard 1200 lines/mm blazed diffraction grating, optimized to diffract primarily into the first order with a dispersion of 0.75 nm/mrad. This means that different frequency components are reflected off the grating at slightly different angles, and can be spatially separated.

(1) Toptica DLC CTL 950

(2) Coherent MIRA

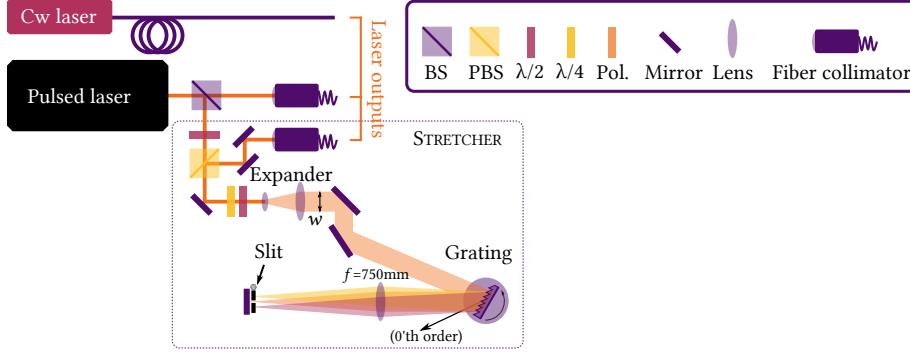


Figure 4.1: Resonant excitation laser sources a cw laser and a pulsed laser. The purple dotted line outlines the stretcher setup, which is used to stretch the length of the laser pulses in time. For an explanation of the working principle see the main text. The box with a solid line is a legend of the most used optical components.

The light from the pulsed laser first passes through a beam expander consisting of a pair of lenses before it is sent to the grating. The expanded beam size of $w = 25$ mm approximately matches the area of the grating. The large beam diameter ensures higher spatial resolution between different frequency components in the Fourier plane when imaging the reflected beam. The dispersed beam is imaged using a large focal length lens ($f = 750$ mm) which focuses it down to spatially distributed spots of diffraction-limited size of $\sim 34 \mu\text{m}$ for a single frequency. A tunable width mechanical slit placed at a distance f from the lens transmits a fraction of the spectral bandwidth in the pulse. The transmitted fraction is back-reflected through the setup by a mirror behind the slit. The spatial dispersion of the back-reflected pulse is reversed when passing the grating again. This is important, in order to avoid a chirp from the different optical path lengths of the frequency components. Due to the polarization flip upon reflection on the mirror behind the slit, the output can be separated from the input by using a polarizing beam splitter (PBS).

Blazed gratings are highly polarization-sensitive, especially when not operated at the blaze wavelength as in our case ($\lambda_{\text{blaze}} = 790$ nm). Therefore polarization control is added using a set of the quarter and half waveplates. The center frequency of the stretcher is tuned by rotating the grating using a motorized stage. The stretcher works across > 100 nm with minimal realignment.

The slit width is adjustable with a micrometer screw, which determines the resulting laser bandwidth. The maximal of possible bandwidth compression is limited by the diffraction-limited spot size, which for the designed setup leads to a bandwidth of ~ 11 GHz. A calibration measurement is performed, by recording the transmitted spectrum of the pulsed laser through the setup at several micrometer slit positions. The recorded spectrum is modeled with a Gaussian and the FWHM is extracted as the bandwidth estimate. The results are shown in figure 4.2. Due to limited resolution of the spectrometer, we cannot measure bandwidths lower than 28 GHz, which leaves a

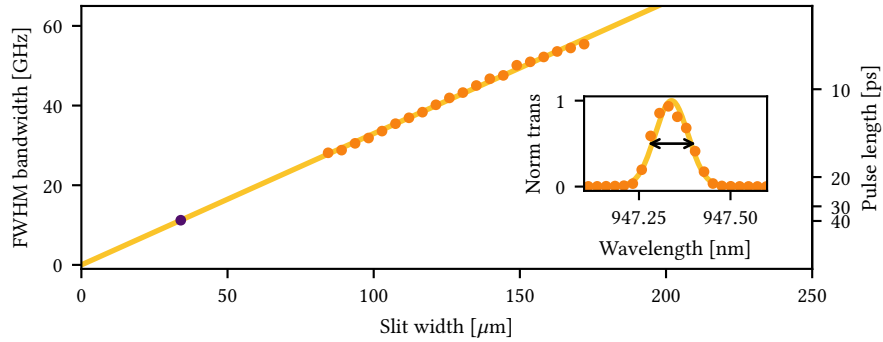


Figure 4.2: Stretcher bandwidth calibration. Each orange point is the FWHM extracted from a Gaussian fit similar to the inset and converted to frequency. The yellow line is a linear fit to the orange points. The purple point is the minimally reachable bandwidth calculated from the diffraction-limited spot size of the setup (see main text).

gap to the diffraction-limited bandwidth, plotted as a purple dot in figure 4.2. To have a calibration of the full axis we use a linear fit to the measured widths, which is plotted in yellow. We see that the fit overlaps exactly with the calculated diffraction-limited point. We use this fit to convert a given slit width to pulse bandwidth in frequency or pulse length in time.

4.1.2 Optical access

The sample is placed in a 1.6 K closed-cycle cryostat⁽³⁾, on top of nanopositioners (XY) as seen in figure 4.3. The sub liquid helium temperatures are expected to strongly reduce the phonon noise in the quantum dot coupled to PCW as explained in section 2.5.4 (Tighineanu et al., 2018). With the nanopositioners, we can move the sample around with respect to a fixed objective, allowing movement from device to device. The sample with nanopositioners is mounted at the bottom of a dipstick which is immersed into the cryostat. The cryostat has optical access along the dipstick with a low-temperature confocal microscope objective with focal length $f = 2.39$ mm and a $4f$ imaging system⁽⁴⁾. The $4f$ -relay images the collimated input laser beam to the back focal plane of the microscope objective, which has a numerical aperture $NA_{\text{obj}} = 0.81$.

Input

As shown in figure 4.3 the excitation laser can be connected to one of the two input fiber couplers that collimate the laser to different beam diameters. The two input paths

(3) Attocube: Attodry 2100

(4) The two alternative experimental setups are with cold finger type cryostats with external objective and stages.

are combined using a polarizing beam splitter to achieve maximal throughput for both. One coupler is chosen to fill the back focal plane of the objective, which then focuses the laser to a diffraction-limited laser spot on the sample. This input is used to focus maximal power onto a single quantum dot. The second outcoupler mode-matched to the shallow etched grating couplers, which will be detailed in the next section 4.2.1. The input path further contains a 50 : 50 beam splitter which splits off the input laser power to a power meter. The power meter signal is fed back to a PID control unit to stabilize and control the incident power. The same beam splitter also allows optical imaging of the sample using a CCD camera. The input path has a set of motorized half and quarter-wave plates which allows for precise control of the input polarization, used to address a specific quantum dot dipole, or couple into the polarization-dependent grating coupler.

The input beam is sent into the cryostat via reflection on a 10 : 90 (R:T) beam splitter, which has highly polarization-sensitive transmittance and reflection coefficients. The actual transmission ranges from 88 % to 95 % at our operation wavelength at around 950 nm. This can straightforwardly be corrected for by a calibration scan of the incident polarization using the motorized wave plates and the PID power control.

Output

The output from a shallow etched grating is collected through the same microscope objective and transmitted at the 10 : 90 beam splitter as seen in figure 4.3. The $4f$ -relay images the photons to the fiber coupler. A set of waveplates compensates for any rotation of the polarization along the out-coupling path. The setup contains two of such collection paths that split on a PBS. This allows the collection from two orthogonally polarized outcoupling gratings simultaneously. Finally, we use a source of white light with a diffuser lens, to illuminate the sample for optical imaging. The white light is placed on a flip mount with a 50 : 50 beam splitter in the collection path. This configuration is practical, since it allows simultaneous white light imaging and laser input for alignment, but can be removed from the collection path when performing experiments.

4.1.3 Filtering Equipment

We typically employ filters to extinguish spectral contributions that do not come from the desired quantum dot transition. These contributions could be from the laser background, the second exciton dipole or the phonon sideband. Table 4.1 shows a comparison of different filtering equipment we use.

We have a standard *grating filter* which works in a similar fashion as the stretcher described above and is sketched in figure 4.4(a). The rejection of wavelength components takes place when the collimated beam is fiber-coupled into a $NA_{\text{fiber}} = 0.13$ fiber. The efficiency of the grating filter is limited to around 65 % by the grating diffraction efficiency, and the number of optical components involved and a fiber coupling. We experimentally reach an efficiency of 58 %.

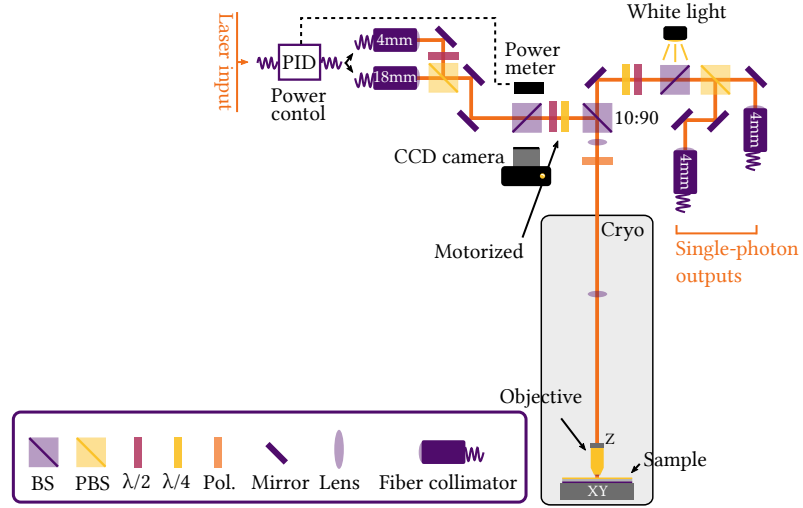


Figure 4.3: The optical access to the sample located in a the cryostat. Laser input is to the left, and sent through the optical components onto the sample. Photons are collected and the output is to the right. For full details see main text. The box with a solid purple line is a legend of the most used optical components.

To use the filtered photon stream as an efficient single-photon source a higher efficiency of the filtering state is desirable. This can be reached using an *etalon filter* as sketched in figure 4.4(a). We use a solid silica etalon where the cavity is formed by coated end faces of the silica block. The frequency is tuned using temperature, by heating a copper heat sink designed also as a mount for the etalon. The etalon is placed at a slight angle, to separate the reflected signal which is blocked. The transmission efficiency of the etalon is specified to 92 % and is limited by the design reflectivity at the end faces and the losses in the silica, but could be improved by using an air-spaced cavity. Experimentally, we reach 87 %, where the deviation from the specified transmission is diffraction losses in the optical components and fiber coupling.

The bandwidths of the two filters are measured by recording the transmitted signal of the cw laser, tuned across the center frequency of the filter. The transmission through the two filters is plotted in figure 4.4(b) and fitted to a Gaussian and Lorentzian for the grating and etalon respectively. The bandwidth is extracted as the FWHM of the fits.

The grating can also be designed to have two output ports at different wavelengths as shown in figure 4.4(a). We can choose geometrical parameters of the setup such that it is possible to spatially resolve wavelength separations of ~ 1 nm. This is enough to split the two wavelengths e.g. the exciton and biexciton into different paths using a D-shaped pickoff mirror.

Filter	Measured efficiency	Resolution (FWHM)
Grating	58 %	22.1 GHz
Etalon	87 %	3.5 GHz

Table 4.1: Table summarizing the properties of the two filters shown in figure 4.4.

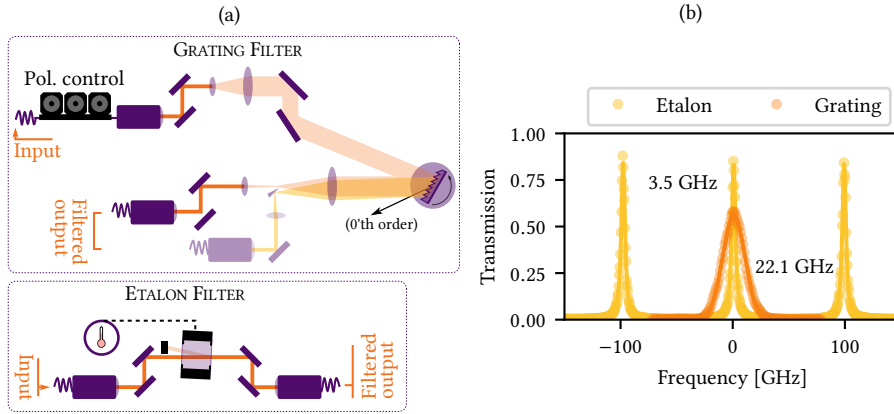


Figure 4.4: Filtering equipment. (a) Sketch of out two different filter types. See main text for description. Legend of optical components are found in figure 4.1. (b) Transmission scan through the two filters, showing their filter FWHM width and their relative efficiencies.

4.1.4 Detection

After filtering, the single photons are ready to perform experiments that will be described in the following chapters of this thesis. Different technologies for single-photon detection are used, generally with a trade-off between efficiency and timing jitter. A comparison between the detectors used in our experiments can be found in table 4.2 with typical performance values.

We have standard fiber-coupled avalanche photo-diodes (APD) which are more or less plug and play, and easy to use. The efficiency is not high but is very well-calibrated, however, the time resolution can be a limitation for some experiments. We therefore typically use superconducting nanowire single-photon detectors (SNSPD), which offer better timing resolution, higher efficiencies, and importantly very few detector dark counts.

Some experiments that will be introduced later, require very high timing resolution. For this, we employ a *fast* APD, which unfortunately has very poor efficiency at our operation wavelength. Very recently, we got access to SNSPDs optimized for timing resolution. The *fast* SNSPD have much better efficiencies and are used for the experiments in chapter 8.

Detector	Efficiency at 940 nm	Resolution (FWHM)	dark cts.
APD	30 %	450 ps	~ 100 Hz
SNSPD	70 %	200 ps	< 5 Hz
Fast APD	1 %	40 ps	~ 300 Hz
Fast SNSPD	~ 50 %	15 ps	< 10 Hz

Table 4.2: Typical performance of the single photon detectors used for experiments throughout this thesis. Resolution is here referring to the timing jitter of the detectors.

4.2 EFFICIENCY CHARACTERIZATION

Achieving high count rates from a single or multi-photon source is crucial, for any quantum information applications of the source. Therefore, outcoupling efficiency is a key task continuously addressed. The first fundamental step towards unity efficiency of a single-photon source is to fully account for all losses that the single photons experiences along the outcoupling route. We, therefore, spend some time on a comprehensive understanding of all components of the out-coupling path. In this section, we characterize all components, both on-chip and in the optical setup. In the remainder of this chapter, we characterize the specific sample and device used for single photon experiments in chapter 5 and 6. The characterization measurements are carried out using the CTL, locked to 950 nm which is the operational wavelength of the single-photon source that will be discussed later.

4.2.1 Mode Matching of Shallow Etched Grating

The goal is to most efficiently collect the photons scattered by the shallow-etched gratings on the current sample into the output fibers. This is maximized by a correct alignment of the sample along the optical axis of the dipstick and by choosing the correct focal length of the fiber coupling lens. The far-field pattern of the mode scattering of the gratings is designed to resemble a Gaussian profile with a low numerical aperture of $NA_{gr} \sim 0.21$ and 0.16 along two orthogonal axes. The beam is thus slightly elliptical, with the larger NA along the polarization axis of the grating. Light is collimated by going through the objective, which results in a collimated beam diameter of $d = 2f_{obj}NA_{gr} = 1.2$ mm, for the largest grating NA value. The beam is imaged to the collection fiber coupler via the $4f$ relay lenses. We can then estimate an approximate fiber coupling lens focal length, which should be around $f_{fiber} = d/(2NA_{fiber}) = 4.5$ mm. This estimate based on the design parameters, might not be the optimal choice, if the beam would be distorted, e.g., by optical components that it travels through. Furthermore, the beam shape is very dependent on the collection angle and exact location on the objective. To take all these possible distortions into account we take an experimental approach to maximizing the coupling.

In figure 4.5 we show an optical image of light coupling through a device, with the input on the right side. The image is without white light illumination and the contour of the nanobeam waveguide device is shown in yellow. The inset shows the beam

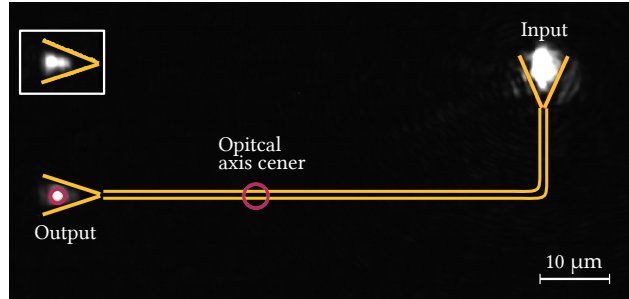


Figure 4.5: Beam shape of the scattered mode from the shallow etched gratings. The main image shows an ideal spatial location of the sample compared to the center of the optical axis of the dipstick marked with the purple circle at the center. Here the beam shape of the output marked with the second circle is round and symmetric. The inset shows the outcoupling grating placed further from the center, which leads to a distorted beam. The input is relatively far from the center, meaning that more power is needed to reach the same coupling to the waveguide mode, but this is not critical.

shape when the sample is located too far from the center of the optical axis of the dipstick. We see that the beam shape here experiences a shear, while the main image shows a more symmetric beam.

The shape of the light collected at the grating is measured using a beam profiler at the Fourier plane of the $4f$ system. The reflected light from the laser input is rejected using an aperture. We measure a beam clip width of $\sim 970 \mu\text{m}$ along the grating polarization axis and $\sim 770 \mu\text{m}$ orthogonally. This confirms the slight ellipticity of the beam, slightly smaller than the design. To find the best mode overlap we test several fiber coupling lenses with focal lengths around 4 mm. Each lens is tested both by fiber coupling, and the optimal lens configuration is found and installed in both in and out fiber couplers⁽⁵⁾. We reach a maximum fiber coupling efficiency of $\eta_{\text{fiber}} = (59 \pm 2) \%$. This is mainly limited by the ellipticity of the beam shape and sub-optimal diffraction-limited performance of the aspheric lens. The efficiency can be improved by using beam circularization optics and a monochromatic lens.

4.2.2 Setup Efficiency

We characterize the transmittance of the laser beam through each free-space optics component, and the measured efficiencies are listed in table 4.3. For simplicity in the list, we have merged all standard optical elements (mirrors, polarizers, and waveplates) into one average value, since the variation from this, is less than a percent nominally. Losses in lenses and the entrance window are too small to measure and are therefore neglected.

(5) The lens used is Thorlabs C230TMD-A.

Single optical element	η_{opt}	$(98 \pm 1) \%$
Objective	η_{obj}	$(82.0 \pm 0.2) \%$
Beam splitter	η_{BS}	$(95 \pm 2) \%$
PBS transmission	η_{PBS}	$(98.0 \pm 0.5) \%$
Fiber coupling	η_{fiber}	$(59 \pm 2) \%$

Table 4.3: Efficiencies of the different components in the collection path of the optical setup in figure 4.3. The value for a single optical element is an average over the measured efficiency for mirrors, waveplates and polarizer. The beam splitter efficiency is the transmission at the polarization that we collect on our main output.

This allows to calculate the setup collection efficiency following the components on the rightmost collection path in figure 4.3

$$\eta_{\text{setup}} = \eta_{\text{obj}} \eta_{\text{opt}} \eta_{\text{BS}} \eta_{\text{opt}}^4 \eta_{\text{PBS}} \eta_{\text{fiber}} = (41 \pm 3) \%. \quad (4.1)$$

The optical components here are; two of the $4f$ lenses, the optical window into the cryostat, two waveplates, a polarizer and two mirrors.

Sample Propagation Loss

We here shortly introduce how the propagation loss on a sample is estimated. We measure the transmission through nanobeam waveguides of different lengths, fabricated on the same sample as the photonic crystal devices. They are made as concentric waveguides, as shown in the scanning electron microscope image in figure 4.6(a). The measured transmission intensity for 6 waveguides of different lengths at a fixed input power is plotted in figure 4.6(b). The intensity decay is fitted to an exponential function and a propagation loss of 10.5 dB/mm is extracted, which is typical for our GaAs samples.

The propagation loss through a photonic crystal waveguide is higher than the nanobeams measured above. This can be because of more surface roughness from the many holes etched in the vicinity of the propagating mode. We estimate the additional PCW loss from the ratio of transmitted power through a PCW and Nanobeam of equal lengths. The estimated propagation loss in a PCW is 14 dB/mm.

Shallow Etched Grating Efficiency

We measure the grating efficiency of a specific device which we use as a single-photon source in the next chapter. The grating efficiency η_{gr} is defined as the fraction of light diffracted by the shallow-etch grating out coupler and is found following the method in (Zhou et al., 2018). Based on the efficiencies in table 4.3 and the power transmitted through the system, we can calculate η_{gr} . The incident power measured after the 10 : 90 beam splitter is $P_{\text{in}} = (16.2 \pm 0.2) \mu\text{W}$ which leads to a power of $P_{\text{out}} = (0.47 \pm 0.05) \mu\text{W}$ in the collection fiber. The amount of power in the waveguide after passing through

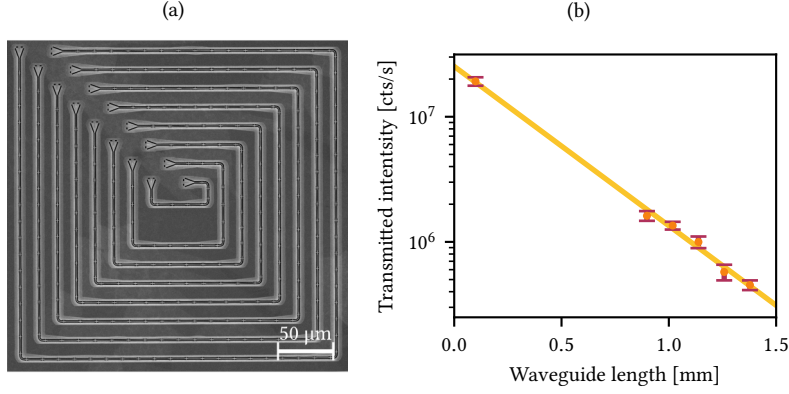


Figure 4.6: Sample propagation loss (a) SEM image of concentric nanobeam waveguides of different lengths. (b) Transmission through waveguides of different lengths like in (a). The yellow line is an exponential fit and leads to a propagation loss of 10.5 dB/mm.

the dipstick and coupling through the grating is

$$P_{\text{wg,in}} = P_{\text{in}} \eta_{\text{opt}} \eta_{\text{obj}} \eta_{\text{gr}} \eta_{\text{fiber}}, \quad (4.2)$$

where the grating efficiency η_{gr} is what we are trying to estimate. Note that η_{fiber} expresses the mode overlap between the mode coupling to/from a fiber and the grating mode.

The power that reaches the collection fiber can be written in the following way

$$P_{\text{out}} = P_{\text{wg,in}} \eta_{\text{prop}} \eta_{\text{gr}} \eta_{\text{obj}} \eta_{\text{opt}}^4 \eta_{\text{BS}} \eta_{\text{opt}}^4 \eta_{\text{PBS}} \eta_{\text{fiber}}. \quad (4.3)$$

For a waveguide of length $\sim 75 \mu\text{m}$ we have a total propagation efficiency of $\eta_{\text{prop}} \approx 84\%$. From equation 4.2 and 4.3 we calculate

$$\eta_{\text{gr}} = (47 \pm 3) \%. \quad (4.4)$$

This is a slightly lower than the reported values in (Zhou et al., 2018), most likely due to fabrication imperfections.

Total out Coupling Efficiency

With all sub-elements of efficiencies at hand, we can calculate the out-coupling efficiency all the way from the quantum dot to the collection fiber in the current setup

$$T = \eta_{\text{prop}} \eta_{\text{gr}} \eta_{\text{setup}} = (18.5 \pm 1.8) \%, \quad (4.5)$$

where the propagation efficiency is $\eta_{\text{prop}} \approx 96\%$ since for the actual experiments nanobeam section is $4 \mu\text{m}$ and PCWG section of $10 \mu\text{m}$ assuming that the quantum

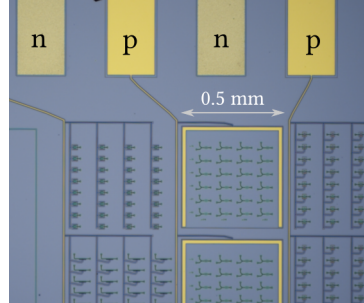


Figure 4.7: Optical image of the sample, displaying different sample sections containing multiple nanophotonic devices. Each sample section is connected to a pair of electrical contacts deposited on the p and n layer of the diode (see figure 4.8(a)). Electrical contacts are highlighted with yellow.

dot is located in the center of the device. We will later in section 5.4, see how this characterization allows us to fully account for all losses in the measured single-photon rate. The efficiency can be readily improved. Newly designed gratings as mentioned in section 3.3.1 reached efficiencies of $> 90\%$. Further, by sacrificing some flexibility in the setup and by replacing all components with state of the art optics, the setup efficiency could be improved to $> 85\%$.

4.3 ELECTRICAL CHARACTERIZATION

In the previous sections, we have focused on the optical parts of the experiment. There is another important aspect of a high-performance setup, we focus on here. As motivated in section 2.4, electrical control of the quantum dot charge environment is important for the quantum dot single-photon emission efficiency.

The electrical control is introduced using a p - i - n diode structure, with ohmic contacts deposited on the p and n layer. By application of an external bias voltage, the electric field across the diode is controlled. In order to actually obtain a more stable charge environment, the voltage source used should not introduce any extra noise. We use a high-resolution DC voltage source with multiple channels, designed to have ultra-low noise with $V_{\text{rms}} < 1\mu\text{V}$. Furthermore, the electrical connection lines entering the cryostat need to be well isolated, to not pick up electrical noise on the way. We found that proper termination and grounding of all unused channels on the voltage source led to significant suppression of electrical noise. Lastly, we carefully went through all electrical cabling in the experiment including all devices connected to the optical components and PC communication links to eliminate ground loops.

4.3.1 Sample Characterization

Typically, the sample is divided into sections sharing a pair of electrical contact pads. To not confuse these sections with references to sections of the thesis we will call them

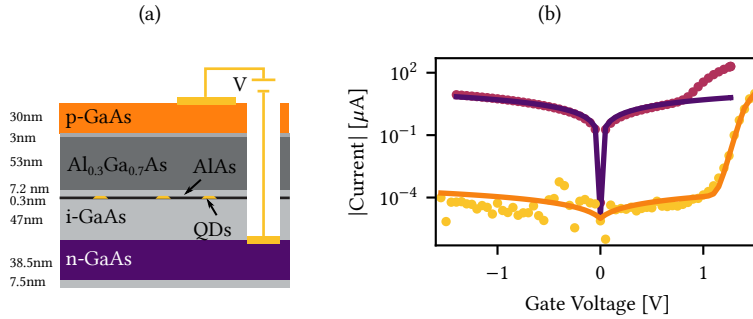


Figure 4.8: Diode characterization. (a) Layout of the p - i - n diode heterostructure in the membrane containing quantum dots. (b) Current-voltage (I - V) characterization of the p - i - n diode measured at temperature 1.6 K, of two different sample sections. The yellow points are recorded in a section with good electrical contacts. This can be seen by the good agreement with the solid orange line which follows an ideal diode (equation 2.1) in series with a $R = 7$ k Ω resistor and a parallel resistance of 10 G Ω . The red points are recorded from a different section with bad contacts and exhibit a large leakage current of ~ 5 μ A. The solid purple line is linear fit corresponding to a 200 k Ω resistor, which does not model the turn-on of the diode.

sample sections. An optical image of the sample used in the next chapters is shown in figure 4.7, where some of the sample sections and their contact pads are visible. The contact pads are highlighted with yellow, where the p contacts connect to the different sample sections. A block of nanophotonic devices is electrically isolated from the rest of the sample by making a trench around it, which reduces the size of the area where the voltage is applied. The trench is made around the U shaped contact in figure 4.7, and forms a local mesa (Pagliano et al., 2014). By bringing the contacts closer to the devices, the RC response time of the system is reduced⁽⁶⁾.

The vertical layout of the membrane heterostructure is shown in figure 4.8(a), where the p - and n -doped layers comprise the ultra-thin diode. To access the n -layer, the membrane is partially etched through before a metal contact pad is deposited. The contacts are wire-bonded to a printed circuit board, which is connected to the voltage source using four sets of twisted-pair cables. All steps involved in making the electrical contact can introduce short-circuits, and therefore impact the final quality of the contacts. We inspected the proper operation of each individual electrical-contacted sample section by recording a current-voltage (I - V) curve using a source meter. In figure 4.8(b) the I - V of two different sample sections on the same sample are shown. We see a very clear turn-on of the diode at a gate voltage > 0.7 V. The two sections show very different leakage currents defined by the current in reverse bias ($V < 0$). The yellow points follow a near-ideal I - V curve plotted in orange, which is a diode in series with a low resistance resistor and a finite parallel resistor. Here, the leakage current is mainly limited by the read-out noise of the source meter in reverse bias. At

(6) This can be even further reduced by bringing the contact to an individual device, which is what seen in the other sample section of figure 4.7.

voltages corresponding to neutral excitons ($1.2 \text{ V} < V < 1.3 \text{ V}$), the leakage current across the diode is $< 100 \text{ pA}$. In contrast, the I - V curve of the second section shown with red points exhibits a large leakage current. This could introduce more noise in the charge environment of the quantum dots. Indeed, all attempts of addressing quantum dots in this section (following the procedures described in the next sections) only led to noise-broadened spectral lineshapes

This shows that a well-performing diode can still be limited by a non-ideal fabrication of the electrical contacts. High-performance sample sections are identified by current-voltage characteristics described in this section.

* * *

This chapter rounds off the introductory part of the thesis, providing background information about the emitter, the photonic device, and the experimental setup to effectively drive the system. Equipment for filtering and detection was presented, together with the main laser sources that will be used. We have presented a thorough characterization of the setup efficiency, which accounts for all losses in our setup. Finally, a characterization of the electrical properties is presented, and a sample section showing near-ideal properties was identified. After introducing and characterizing the device we use, we are now ready to move forward and present single- and later on multi-photon experiments in the remaining chapters.

C H A P T E R



A SCALABLE SINGLE-PHOTON SOURCE

Thorough quantum dot characterization allows scalable single-photon emission. The procedures presented can be used as recipe for achieving high quality single photon emission from quantum dots in planar waveguides.

A single-photon source must meet a list of requirements to in order to perform as a resource in a quantum network. In summary, the requirements are 1) high single-photon emission rate 2) efficient generation and background free collection, for on-demand operation 3) noise-free emission with linewidths limited by the radiative decay time. In this chapter, we show how these requirements are fulfilled in our platform, which we have introduced in the previous chapters.

In sections 5.1 and 5.2, the photonic crystal device with quantum dots that is employed for these measurements is introduced and characterized. After this we characterize a selection of quantum dots with resonant spectroscopy in section 5.3. In the last sections 5.5, 5.6 and 5.7 we demonstrate noise- and background-free emission, by measuring the quantum dot linewidth, single photon purity and the indistinguishability of the emission. The experimental procedures and the discussions throughout this chapter can be used as a recipe for reproducible realization of this scalable single-photon source.

The work presented in section 5.5 led to the publication Pedersen et al., 2020. Further, the experimental data presented in section 5.4 and 5.7.1 led to the publication Uppu et al., 2020.

5.1 PHOTONIC CRYSTAL WAVEGUIDE CHARACTERIZATION

We start out by characterizing the spectral properties of the photonic crystal waveguides on the sample. The sample contains an array of PCWs (shown in figure 4.7), where the

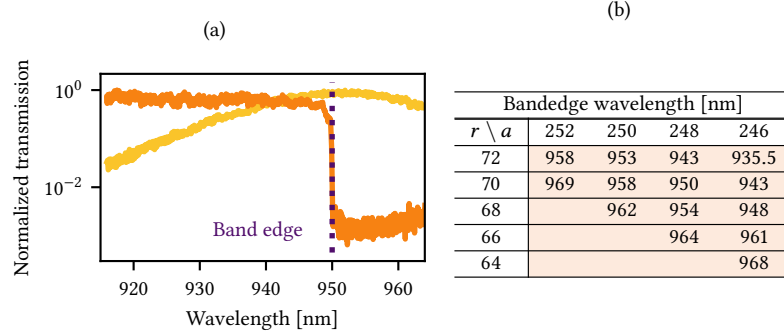


Figure 5.1: Band-edge identification of PCW. (a) Wavelength dependent transmission scan of a PCW shown as an orange curve. To remove the grating coupler dependence, the scan is normalized to a scan recorded through a nanobeam waveguide displayed as the yellow curve. (b) Band-edge identified using transmission scans similar to (a) in PCW of different lattice a [nm] and radius r [nm] parameters.

lattice parameter a and the hole size r is varied. This will change the spectral location of the band-edge, which due to fabrication imperfections, might be slightly different from design. Therefore, the first step is to identify the location of the waveguide cut-off by recording the wavelength-dependent transmission through the PCW. Such a scan is displayed with an orange curve in figure 5.1(a), where the dramatic drop in the transmission is seen at the band-edge. The PCW transmission curve is normalized to the transmission through a nanobeam waveguide shown as a yellow curve and thereby removing the spectral dependence of the shallow etched gratings. A table summarizing the parameters and the measured band-edge location for each PCW in the array is displayed in table 5.1(b).

The peak efficiency wavelength of the shallow etched gratings is measured from the transmission through a nanobeam waveguide. For this sample, it is at ~ 950 nm, and we are therefore most interested in PCW with a band-edge in this wavelength region. For the experiments presented in this chapter, we use the structure with $a = 248$ nm, $r = 70$ nm.

An SEM image showing the type of PCW device used for all measurements is shown in figure 5.2. The center marked in yellow is the slow light section as explained in section 3.2 with parameters $a = 248$ nm, $r = 70$ nm. On both sides, a fast light PCW section acts as an adapter between the slow light PCW and the nanobeam sections. The fast light regime is reached by decreasing the lattice parameter by a few percent to ≈ 236 nm. On the right end of the structure, the nanobeam waveguide is immediately terminated with a shallow-etched grating which we denote as (1) in figure 5.2. The left side is split into two ports using a Y-splitter and terminated with gratings (2) and (3). This design is optimized for a different type of experiment, and for the experiments presented here, a two-port or even one-port design would be more suitable. This type

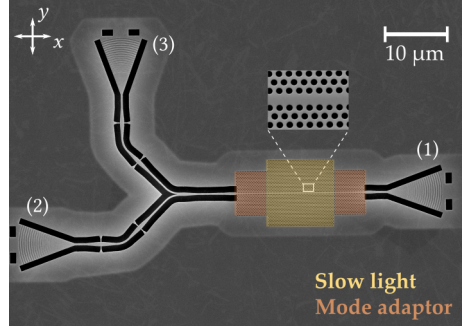


Figure 5.2: SEM image displaying the PCW device used for the measurements in this chapter. The PCW section contain both a slow light section and a fast light section which works as a mode adaptor to the nanobeam waveguides.

of device was the only one available within the section, where the electrical contacts were successfully fabricated (see section 4.3).

5.2 RESONANT TRANSMISSION FOR QUANTUM DOT SEARCH

In resonant transmission (RT) we study the interaction between a quantum dot in a waveguide and a weak coherent state transmitted through the waveguide mode. Coherent interaction between a single photon and the quantum dot leads to a reflection of the photon at the quantum dot location. This is an interference effect, which is only present if the incident light is on the single photon level (Javadi et al., 2015). Attenuated cw laser light is launched into the waveguide from grating coupler (2). Only photons that are on resonance with the quantum dot transition will be fully reflected. By tuning the laser across the quantum dot resonance and recording the transmitted signal on grating (1), we can identify the spectral location of all quantum dots strongly coupled to the waveguide in a single scan.

For the specific sample, we observe an average quantum dot density of $\approx 10 / \mu\text{m}^2$ on the sample which means that we can expect to see resonances for around 60 quantum dots within a $20 \mu\text{m}$ long waveguide including both fast and slow light sections. With this relatively high number of quantum dots in a single device, the RT scan has proven a very robust way to identify quantum dots with potentially good single-photon emission properties.

The profile of the RT-dip reveals a lot about the quality of the quantum dot. The RT-dips on this sample are resolved by scanning the laser with a step size of 100 MHz (locked to a wavemeter) over a range of ~ 2 THz in the vicinity of the band-edge. We search for neutral excitons and keep a constant bias voltage of 1.24 V applied during the scans. A full range scan showing sharp transmission dips as the laser crosses resonances is shown in figure 5.3, and zooms of four lines are shown in figure 5.4. The probability that a resonant laser interacts with the quantum dots increases with a better

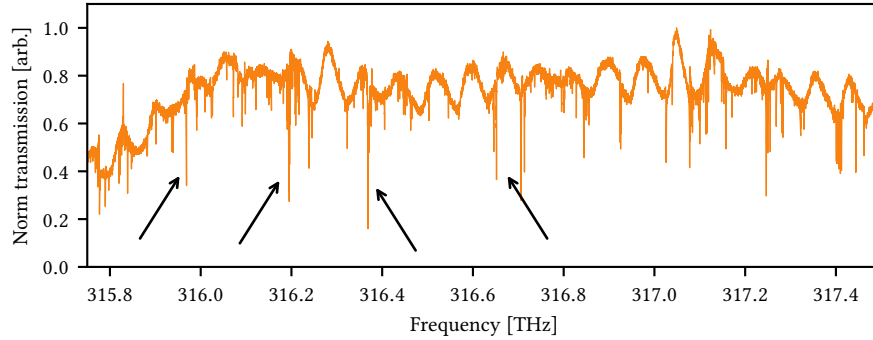


Figure 5.3: Resonant transmission scan, through a PCW device as the one shown in figure 5.2. RT-dips are observed as the laser is scanned across the resonance frequency of the quantum dots. A zoom in on the lines marked by arrows is found in figure 5.4. The laser is scanned in steps of 100 MHz, with an integration time of 50 ms. The y-axis is scaled to the maximal value of the scan, and the absolute scale is not important for line identification purposes.

coupling of the quantum dot to the waveguide mode, i.e. higher β . Therefore the depth of the dips gives an immediate signature about which dots are well coupled to the waveguide mode.

Charge noise in the vicinity of the quantum dot as introduced in section 2.5.4 will tune the quantum dot resonance via the Stark effect. This will broaden the line shape (or even appear noisy), while also resulting in shallower dips. This way, the RT scan can immediately reveal which resonances are heavily affected by charge noise.

Four prominent RT-dips are marked with arrows in figure 5.3, which we now investigate in detail. Even from a qualitative observation of each of the lines in 5.4, it is clear that some of them suffer from excess noise. Quantum dot 2 (QD2) is a typical example of a lineshape that is affected by spectral diffusion. The wide distribution of sharp peaks appears when the quantum dot resonance is shifted around on ms time scale while the laser is scanned across the lineshape with 50 ms/100 MHz. QD3 also appears broadened but the line shape appears more continuous, which could indicate noise on a faster time scale. The deep RT-dip suggests that it couples strongly to the waveguide, which is atypical for linewidth broadened quantum dots. Finally, QD1 and QD4 exhibit narrow, and clean RT-dips, with no significant broadening. One difference to notice is that for QD4 both of the exciton dipole transitions are visible, while for QD1 we only see one. This could indicate that QD1 is spatially located more at the center of the waveguide where only the Y-dipole couples, as seen in figure 3.5.

5.3 RESONANT SPECTROSCOPY

To generate single photons from a quantum dot, we need to resonantly excite them, with out of plane excitation. To do so, the physical location of the quantum dots needs

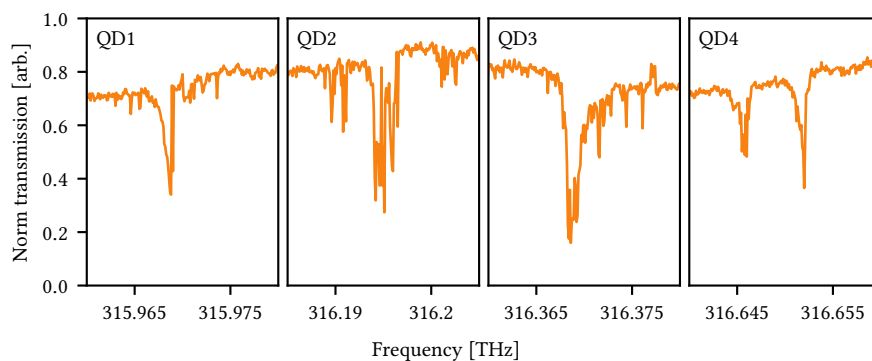


Figure 5.4: Zoom in on the 4 dots marked with arrows in figure 5.3. The laser is scanned in steps of 100 MHz, with an integration time of 50 ms. The y-axis is scaled to the maximal value of the scan, and the absolute scale is not important for line identification purposes.

to be identified, such that the excitation laser can be focused on the quantum dot from above. This is resonance fluorescence (RF) and is a challenging excitation scheme that requires simultaneous high performance of all the involved components. Much of previous work with quantum dots has been performed using quasi-resonant excitation schemes which have less strict requirements. Over the past year during this work, the combination of high-quality samples with excellent quantum dot behavior, low noise electrical wiring, carefully optimized optical setup, and a stably operating closed-cycle cryostat at 1.6 K, has made resonant excitation possible for nearly all well-coupled quantum dots.

5.3.1 Continuous-Wave Excitation

The quantum dot locations are identified by tuning the cw laser to a specific resonance frequency and scanning the laser spot along the PCW on the sample while monitoring the output on a spectrometer. This is in itself challenging, since we cannot spectrally distinguish quantum dot emission from laser background. However, by electrically tuning the quantum dot in and out of resonance with the laser, we search for positive differential photocounts in detection. Using this method the laser spot can be aligned to the quantum dot, typically with excellent laser suppression (better than 1 : 100) due to the spatial separation between the excitation and collection spots.

It is not certain that a quantum dot that does not show charge noise in the RT-lineshape, will also have a noise-free RF-lineshape. The two schemes use very different laser powers and are fundamentally different interactions. This can be checked using a voltage scan, where we typically scan with a step size of 0.2 mV and 50 ms integration. Such voltage scans performed for the three dots are shown in figure 5.5, where we see that QD3 is very noisy under RF. Based on these measurements we abandon QD3 as a potential source.

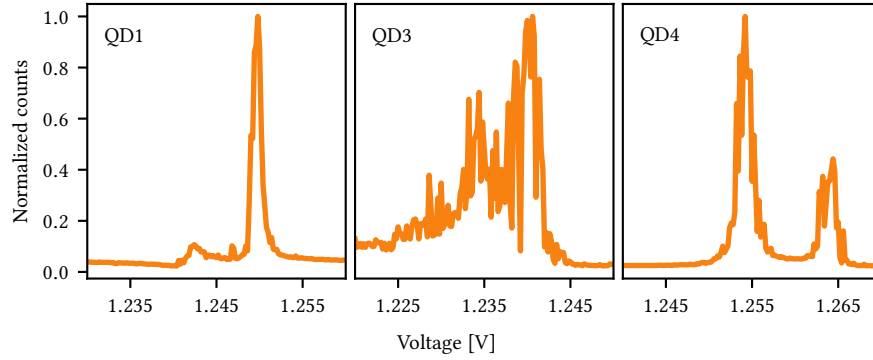


Figure 5.5: Voltage scans of three quantum dots under cw resonance fluorescence. The voltage is tuned in steps of 0.2 mV with 50 ms integration time for each point.

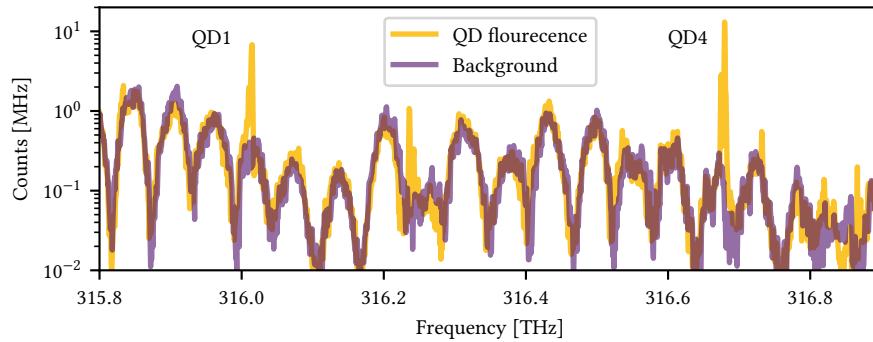


Figure 5.6: Yellow curve is resonance fluorescence under cw excitation, with constant applied voltage of 1.24 V. The laser frequency is tuned across the resonance of QD1 and QD4, which are spatially within one laser spot size. Purple curve is the same frequency scan but at gate voltage 1 V. Note the logarithmic scale.

The spatial location of QD1 and QD4 are within the same laser spot size, and we can therefore probe both of them in one RF frequency scan as shown in yellow in figure 5.6. We observe fringing of the background signal coupling through the waveguide. The period of the fringes corresponds to the free spectral range of a weak Fabry P erot cavity formed by the mode adaptors from the slow to fast light section. A background measurement is recorded at a gate voltage of 1 V where the quantum dots are tuned off. This shows that the fringes are not an effect coming from the quantum dots, but due to small amounts of reflections on the mode adaptors. The spectral location of the quantum dot emission compared to the fringe is important. A fringe maximum would lead to more laser background, which could be problematic for QD1, where QD4 on the other hand is located in-between two fringe maxima.

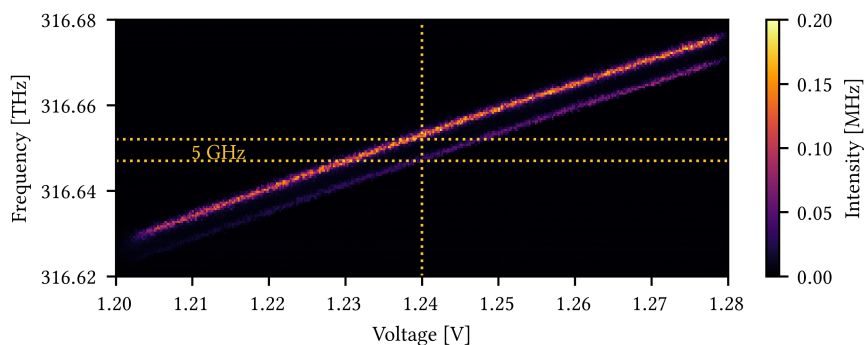


Figure 5.7: Frequency voltage plateau map under RF of QD4. The two exciton dipoles observed with same Stark tuning parameter and distinguished by the fine structure splitting indicated with dotted lines.

By simultaneously scanning both the frequency and voltage, we can map out the whole charge plateau of the Coulomb blockade regime for neutral exciton, shown in figure 5.7 for QD4. The quantum dot resonance frequency tunes with the Stark parameter, which can be extracted from the slope. The Stark parameter for this sample is ~ 0.5 GHz/mV and varies slightly for different dots. The two emission lines observed in figure 5.7 are the two exciton dipoles, since they tune with exactly the same slope. The fine structure splitting between the dipoles is 5 GHz, indicated with dotted lines. The tuning range is around 50 GHz corresponding to ~ 0.15 nm and is typical for the sample.

5.3.2 Pulsed Resonant Excitation

Triggered single-photon emission from the quantum dots can be realized using a pulsed resonant excitation. However, the spectral bandwidth of our pulsed laser is ~ 100 GHz, which is much wider than the transition we would like to excite. This means that only a small fraction of the laser pulse will be resonant with the quantum dot transition. Therefore, to excite more efficiently, the bandwidth is narrowed to ~ 22 GHz using the pulse stretcher. We filter the single-photon emission using the 3.5 GHz bandwidth etalon filter. Some laser background will remain in the collected mode, which we quantify by the *laser impurity*. We will now discuss contributions to this parameter for our device and experimental setup.

Laser Impurity

In most systems, as described in 3.1, a cross-polarized excitation-collection geometry is employed. In the planar nanophotonic structures, the excitation is spatially separated from the collection, which allows excellent extinction without compromising on the excitation polarization. The figure of merit used to express this is the single-photon

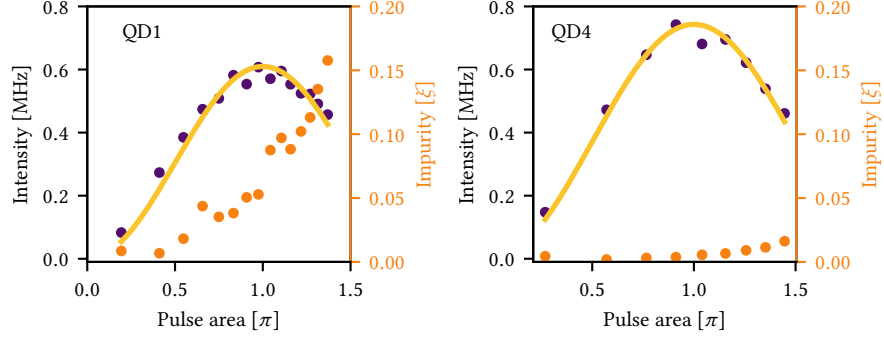


Figure 5.8: Rabi oscillations observed by increasing the pulsed laser power. The blue data points displayed are the raw detected count rate with the background (at gate voltage 1 V) subtracted. The solid line is a fit to the data using a squared sine. The laser impurity is defined in equation 5.1 calculated from the raw counts and the background measurement.

impurity, which is the residual laser pump intensity relative to the single-photon intensity

$$\xi = \frac{I_{\text{laser}}}{I_{\text{single photons}}}. \quad (5.1)$$

The impurity is measured by tuning the quantum dot in an out of resonance with the bias voltage, and effectively turning the emission on (I_{on}) and off (I_{off}). Experimentally we calculate

$$\xi = \frac{I_{\text{off}}}{I_{\text{on}} - I_{\text{off}}}. \quad (5.2)$$

By increasing the power of the pulsed excitation laser, the detected single-photon emission will exhibit Rabi oscillations. Such a power series is performed using an SNSPD, for both QD1 and QD4, and the recorded data are shown in figure 5.8. The solid line is a fit to a squared sine. The two data series are recorded under the same experimental conditions in terms of excitation polarization and in- and out-coupling efficiencies. We observe a dramatic difference in impurity at π -pulse excitation for the two series with $\xi = 0.08$ and $\xi = 0.006$ for QD1 and QD4 respectively. This could relate to the background fringe in the PCW observed in figure 5.6, where QD1 is spectrally overlapped with the maximum of a fringe, and more laser background couples through the waveguide at this frequency.

The PCW background fringe is only one of many effects playing into this ratio. To be able to minimize this ratio it is important to understand all these contributions. We, therefore, summarize the contributions:

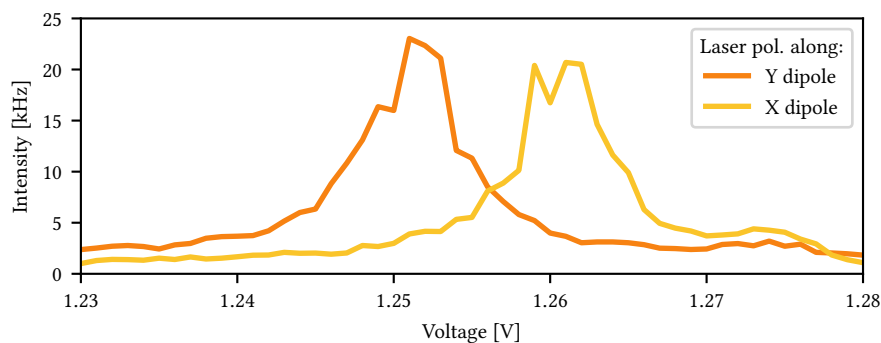


Figure 5.9: Voltage scan of single-photon emission intensity for the laser excitation polarization aligned with the waveguide (X-dipole) or orthogonal to the waveguide (Y-dipole). The etalon filter is applied to distinguish the emission two dipoles in frequency. This measurement was done on QD₄.

- β -factor
- Intrinsic quantum dot efficiency
- Spatial extinction
- Spectral width of the laser
- Waveguide coupled laser background
- Excitation polarization overlap with dipole
- Out of plane laser scatter on the PCW.

Many of the effects have already been touched throughout the chapter, but one important parameter has not yet been discussed, which is the excitation polarization overlap with the dipole. As we will see now the emission efficiency is highly affected by the excitation polarization.

Polarization Impurity Optimization

The overlap between the polarization of the excitation laser and the orientation of the dipole we want to excite has a dramatic impact on the impurity. By aligning the excitation polarization orthogonal (y , figure 5.2) or along the waveguide (x , figure 5.2), we can almost fully alter between exciting the X and the Y dipole as shown in figure 5.9. We typically choose the Y dipole since it should couple more efficiently to the waveguide if the quantum dot is approximately centered in the waveguide (see section 3.2.1).

In figure 5.10 the effect of changing the excitation polarization on Rabi oscillation data-series is illustrated. The highest count rate at π -pulse excitation is reached by

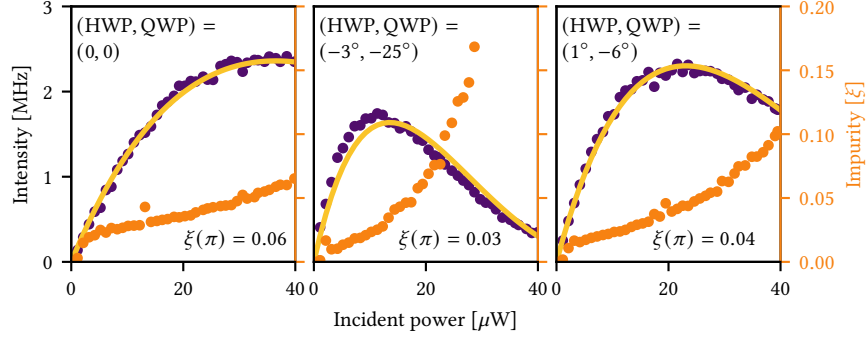


Figure 5.10: Polarization dependent Rabi curves, and impurity. Identical power series are performed, where only the excitation polarization is changed. The first panel is optimized to the maximal intensity at π -pulse excitation, the second panel is optimized to minimal impurity at π pulse excitation and the last panel is a compromise between the two. Measurements are here done on QD1.

aligning the excitation polarization along the Y dipole. This corresponds to the data series in the first panel. When the dipole is strongly coupled to the waveguide, it couples weakly to the out-of-plane field, from which we excite in RF configuration. This means that reaching π pulse excitation requires much more power applied to the sample. This effect can be mapped out by scanning the excitation polarization in a small range around the Y dipole, using the motorized quarter and half waveplates. The excitation power is kept low, to ensure not to cross the π pulse excitation during the scan. Using the basis of (HWP, QWP) = (0, 0) for exciting the Y dipole, the optimized laser background extinction is at (HWP, QWP) = (-3° , -25°). This on the other hand leads to much lower counts as seen in the second panel. This is because we also excite the second dipole at this polarization, but filter the emission out on the etalon filter. Therefore there is a trade-off between the two configurations. The last panel in figure 5.10 shows an optimized configuration from the scan where both the intensity is kept high and impurity low. Experimentally mapping this out methodically also takes backscattering of the incident light into account.

5.4 10 MHz SINGLE-PHOTON SOURCE

In this section, we are going to present how our device using QD4 can operate as a triggered 10 MHz single-photon source, using the fully optimized experimental parameters described above. First, we perform a time-resolved measurement revealing the exciton state lifetime as shown in figure 5.11(a). The decay rate γ can be extracted by fitting the data to an exponential decay convolved with the instrument response function (IRF). The resulting fit is shown in purple on top of the histogram along with the corresponding decay rate. We can calculate the lifetime-limited linewidth to be $\Gamma = \gamma/2\pi = (460 \pm 2)$ MHz.

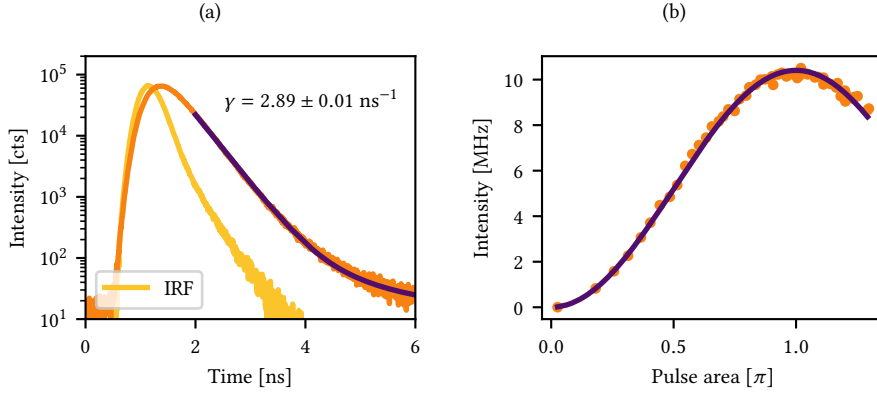


Figure 5.11: (a) Lifetime measurement of QD₄ displayed in orange. The instrument response function (IRF) for the APD is shown in yellow. The purple line is a fit to an exponential convolved with the IRF. (b) Rabi oscillation observed by increasing the power of the pulsed excitation laser. The purple line is a fit to a squared sine.

To maximize the count rate, we employ a pulsed laser source with a higher repetition rate. This laser can operate at 145 MHz and is otherwise similar to the one introduced in chapter 4. In figure 5.11(b) we present the power-dependent Rabi oscillations recorded using this laser. Here, the intensity is background subtracted and corrected for detection efficiency. We extract the maximal count rate at π -pulse area from a sine square fit, yielding a single-photon rate in the fiber of (10.41 ± 0.04) MHz. The error is the statistical error on the fit parameter assuming a Poissonian error on the data points.

5.4.1 Efficiency Breakdown

We will now show that using the characterization measurements, together with knowledge of the intrinsic efficiency of the source, we can fully account for the observed single-photon rate. All efficiencies are listed in table 5.1. Ideally, a single photon is emitted for every single excitation laser pulse, and therefore, we compare the laser repetition rate of 145 MHz to the measured single-photon rate.

Firstly, we have losses introduced in the experimental setup. The single photons couples to both directions of the PCW, which means that we only collect half of the emitted photons using one outcoupling grating (1). Secondly, the thorough efficiency characterization from section 4.2 allows accounting for the propagation losses of the emitted photon on- and off-chip up to the collection fiber. All these propagation losses are taken into account through the total out-coupling efficiency T in table 5.1. Further, the non-unity transmission efficiency of the etalon filter employed in suppressing the phonon sideband should also be taken into consideration.

	Component efficiency	Current device
SETUP	Directionality	50 %
	Total out-coupling T	(18.5 ± 2.0) %
	Spectral filter η_f	(87 ± 1) %
	Total setup efficiency $\eta_{t \text{ extrmsetup}}$	(8.0 ± 0.9) %
SOURCE	Dipole η_Y	> 98 %
	Zero phonon line η_{zpl}	(95 ± 1) %
	Radiative η_{dark}	~ 98 %
	β	> (92 ± 5) %
	Single-photon source efficiency η_S	> 82 %
	Expected single-photon rate	(9.8 ± 1.0) MHz
	Measured single-photon rate	(10.40 ± 0.04) MHz

Table 5.1: Breakdown of the efficiencies of the source and characterization setup, showing that we can account for all losses.

Apart from the propagation losses, the source efficiency is intrinsically limited by the quantum efficiency of the quantum dot itself. The contributions are listed in table 5.1 under SOURCE. (1) Loss of emission due to partially exciting the wrong dipole. This is estimated from power series like the one in figure 5.8, by comparing the maximal count rates at the polarization aligned with dipole to the rate at the polarization that is used for the experiments. (2) Under strict resonant excitation, inelastic scattering between the exciton and phonons in the suspended membrane, leads to red and blue shifted emission in a broad *phonon sideband*, which is filtered out by the etalon. The phonon side-band can be resolved under cw excitation using the spectrometer as seen in figure 5.12. From a comparison of the area under a Gaussian fit to the sideband and a Voigt fit to the emission line, we estimate the efficiency of emission into the zero phonon line. (3) Coupling to the dark exciton state via a spin-flip is another source of loss. We estimate the efficiency by solving the optical Bloch equations, including the dark state introduced in equation 2.18 for the excited state. The efficiency is extracted by fitting the measured bunching in the second order correlation function $g^{(2)}(\tau)$ ($\tau \neq 0$) with using this dark state model (Uppu et al., 2020). (4) Finally, non-unity β -factor accounts for loss of the QD emission into the non-guided modes. It is estimated from the radiative lifetime of the quantum dot coupled to the waveguide, compared to the lifetime of quantum dots that are not coupled (Arcari et al., 2014; Uppu et al., 2020).

Including all loss contributions listed in table 5.1, we arrive at an expected single-photon rate of (9.8 ± 1.0) MHz, which agrees with the measured single-photon rate within the estimation error. This highlights the importance of a well-characterized setup and device. Importantly, the careful characterization clearly highlights which are the key aspects that should be improved to achieve higher in-fiber single-photon rates. Excitingly, we observe that the intrinsic rates (i.e. each of the source related parameters in table 5.1 are close to unity and observe that our source device has an on-chip efficiency of > 82 %. This efficiency in the current device is limited by the β -factor

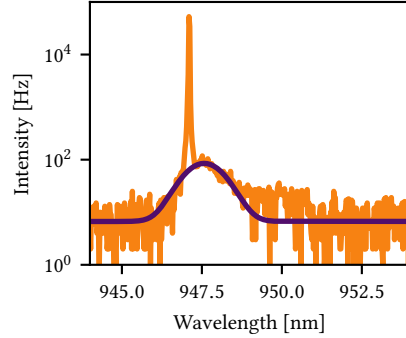


Figure 5.12: Resonance fluorescence spectrally resolved using the spectrometer. The quantum dot is excited with the cw laser to resolve the phonon sideband. The solid curve is a Gaussian fit of the emission in phonon sideband. The deviation from the Gaussian shape is caused by the PCW band-edge at 950 nm, which leads to a slight underestimation of the area.

and η_{zp1} . The β -factor can be improved to near-unity by deterministically positioning the QD within the waveguide (He et al., 2017; Pregnolato et al., 2020). Further, the emission in the phonon sideband can be reduced by either clamping the structure to reduce the phonon density of states or by cooling the sample further (Dreessen et al., 2019; Tighineanu et al., 2018).

We have now presented how to achieve the two first requirements listed in the introduction of the chapter, i.e. (1) efficient excitation of the quantum dot and (2) a high in-fiber single-photon rate while suppressing laser background. Now we are going to demonstrate the possibility to satisfy the last requirement, which is minimal linewidth broadening.

5.5 NEAR LIFETIME-LIMITED LINEWIDTHS IN PHOTONIC CRYSTAL WAVEGUIDES

The noise-induced spectral broadening of the quantum dot resonance can limit the indistinguishability of the emitted photons. Spectral fluctuations of the emission makes the photons distinguishable in frequency over the time-scale of the fluctuation. Therefore observing linewidths limited by the radiative decay rate $\Gamma = \gamma/2\pi$ is a continuously studied topic and strived to improve within the quantum dot community (Jahn et al., 2015; Löbl et al., 2017; Thyrestrup et al., 2018). In this section, we discuss the importance of embedding quantum dots coupled to PCW in a diode heterostructure to avoid broadening of quantum dot lineshape due to charge noise.

As discussed in section 2.5.4 the solid-state environment introduces charge noise on the quantum dot resonance frequency. This noise is on millisecond time scale and broadens the quantum dot linewidth above the lifetime-limited linewidth. Charge control using a p - i - n diode has proven to efficiently suppress such noise for quantum dots in bulk semiconductor material (Kuhlmann et al., 2015). In a nanophotonic structure,

the introduction of etched surfaces in the vicinity of the quantum dots introduces additional charge noise, due to the formation of surface charge traps (Ha et al., 2015; Houel et al., 2012; Liu et al., 2018; C. F. Wang et al., 2004). Typically, a linewidth broadening of $> 4\Gamma$ is observed for quantum dots without electrical gates, embedded in nanophotonic structures (Javadi et al., 2015).

As described in section 4.3, the sample employed for the measurements in this chapter is embedded in a near-ideal diode heterostructure. Therefore, the wide frequency range RT scan in figure 5.3 provides a measurement of the linewidth of quantum dots in a charge controlled environment. By identifying and fitting each RT-dip to a model for the lineshape model we can extract a large sample of linewidth measurements.

5.5.1 Resonant Transmission Lineshape Model

The model used to fit the lineshape of the transmission dip as a function of frequency detuning $T(\Delta\nu)$ is described in Javadi et al., 2015. The functional form is

$$T(\Delta\nu) = \frac{(\Gamma + 2\Gamma_{\text{dp}})[(\beta - 1)^2\Gamma + 2\Gamma_{\text{dp}}] + 4\Delta\nu^2(1 + \chi^2)}{(\Gamma + 2\Gamma_{\text{dp}})^2 + 4\Delta\nu^2 + 4\beta\Gamma\chi\Delta\nu + \left([\beta - 1]\Gamma - 2\Gamma_{\text{dp}}\right)^2 + 4\Delta\nu^2}\chi^2, \quad (5.3)$$

where γ and γ_{dp} radiative decay rate and dephasing rate respectively, and β is the waveguide coupling factor. A slight asymmetry observed in the RT lineshapes from a Fano resonance, described by the Fano parameter χ (Fano, 1961). The Fano lineshape comes from the interference between the quantum dot resonance and the weak reflection from the fast light mode adapters, the same reflections that are causing the fringing in the background in figure 5.6. Each RT dip can be fitted independently to equation 5.3, as shown in figure 5.13(a) for QD₄, exhibiting a slight Fano lineshape asymmetry. We extract an RT linewidth from the FWHM of the fitted function. For simplicity, the contribution from the Fano parameter is omitted when calculating the FWHM of the fitted curve. The FWHM obtained in this way will always over-estimate the linewidth, and thus provides an upper bound.

5.5.2 Linewidth Modeling of a Large Sample of Quantum Dots

We identify 78 RT dips from the PCW scan in 5.3 and include an additional dip from another scan for parts of our analysis. Among the RT dips that were analysed in the first scan, a large fraction (50) could be fit robustly with the model and the linewidths could be extracted. The remaining 28 lines do not fit the RT lineshape and their linewidths cannot be robustly extracted. These noisy RT-dips correspond to the quantum dots that are located close to an etched surface, and are therefore influenced by charge noise from surface charge traps. Under this assumption, it is possible to estimate a minimum distance that the quantum dot needs to be from the etched holes forming the PCW. The

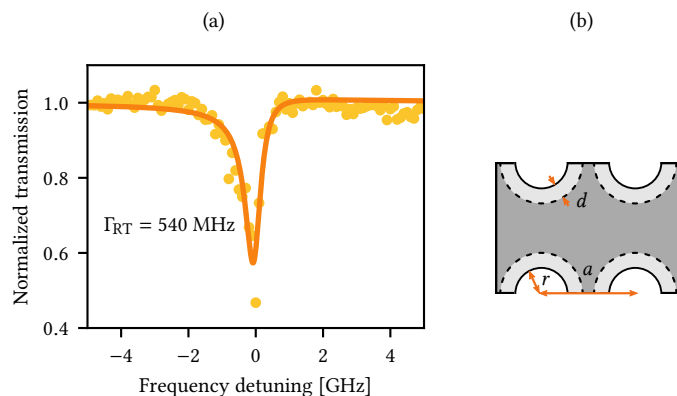


Figure 5.13: (a) Fit of the RT lineshape model defined in equation 5.3 to a RT scan of QD₄. The linewidth Γ_{RT} is estimated as the FWHM of the model, excluding the Fano parameter. (b) Section of a photonic crystal waveguide with a hole radius r and lattice constant a . Area shaded in light grey is a distance d from the holes. This illustrates the region where the quantum dots are affected by surface charges.

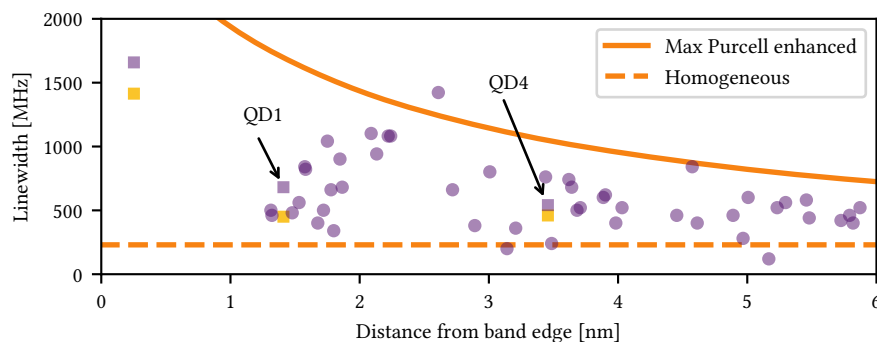


Figure 5.14: Purple plots is the extracted FWHM linewidth from fits like in figure 5.13(a). Three yellow points are the lifetime limited linewidth extracted from fits like in figure 5.11(a). The three specific lines including QD₁ and QD₄ where a lifetime limited measurement was also performed are marked with a square point and pairs with the yellow square at the same frequency. Solid line is the maximally possible purcell enhancement using the curve in figure 3.4(b). The dashed line marks the average homogeneous lifetime limited linewidth measured on a few dots outside the PCW.

total area within a section of the PCW shaded in figure 5.13(b) is denoted A_{total} , while the area which is a distance d away from the holes shaded in darker grey is denoted A_{lim} . By equating the ratio of the areas to the fraction of successfully fitted quantum dots $f = 50/78 = A_{lim}/A_{total}$, the limiting distance is estimated to be $d < 44$ nm.

In figure 5.14 the linewidths are plotted with purple points as a function of spectral distance from the band-edge. Finding quantum dots very close to the band-edge is challenging due to the steeply changing background from the photonic crystal cut-off. No lines in this region were present in the first scan. Therefore, in figure 5.14 we have included an RT dip that is ~ 0.25 nm from the band-edge measured on another identical PCW. Yellow squares represent linewidths limited by the radiative lifetime measured separately for three quantum dots. The corresponding three RT linewidths are distinguished from the rest by a square purple marker instead of a circle. The lifetime limited natural linewidth is extracted from time-resolved resonant lifetime measurements as in figure 5.11(a). Comparing the natural linewidths to the RT linewidths we get $\Gamma_{\text{RT}}/\Gamma = 1.17, 1.51, \text{ and } 1.18$, respectively. This shows a significant suppression of linewidth broadening for all three quantum dots compared to previously achieved in nanophotonic structures without electrical control.

For comparison we plot an estimate of the lifetime limited homogeneous linewidth with a dashed line. The homogeneous linewidth is extracted as an average over a few lifetime measurements of quantum dots located in the bulk material without any nanophotonic structure. The transform-limited linewidth of quantum dots coupled to the PCW increases with Purcell enhancement of the decay rate. This explains the rising trend of the extracted linewidths towards the band-edge where the higher Purcell factors are reached. In figure 3.4(b) we discussed the frequency dependence of the maximum Purcell factor that can be achieved in a PCW. From this, the maximal achievable Purcell enhancement is plotted as a solid line in figure 5.14, and we see that the line follows the extracted linewidths as an upper bound. This indicates that the observed spread in linewidths is primarily induced by frequency and position dependent Purcell enhancement and hence contributions from other linewidth broadening effects are very limited.

The spread of the RT linewidths in figure 5.14 can be explained by the wavelength and position-dependent Purcell factor. The three comparative lifetime measurements suggest only a small fraction of broadening above the transform-limited linewidth. Based on this we see strong indications of near lifetime limited linewidth for a large fraction of the quantum dots. This demonstrates the large potential for using quantum dots in the sample as single-photon sources. In the remainder of this chapter, we are going to perform single-photon purity and single-photon indistinguishability measurements using QD₄, which characterizes the quality of the emitted single-photons.

5.6 SINGLE-PHOTON PURITY

A stream of photons emitted from an ideal two-level quantum system under continuous excitation will never contain two photons at the same time. Therefore, can the single-photon nature of the source be quantified by measuring the photon correlations. The second-order intensity correlation function is given by

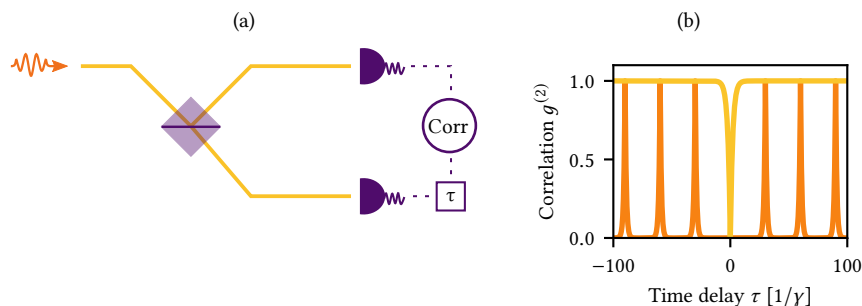


Figure 5.15: Hanbury Brown Twiss experiment. (a) Experimental setup to perform a HBT measurement. A single photon is incident to a 50:50 BS, and the output is detected. (b) Expected correlation histogram from a HBT measurement under cw (yellow) and pulsed (orange) excitation.

$$g^{(2)}(t, \tau) = \frac{\langle a^\dagger(t) a^\dagger(t + \tau) a(t + \tau) a(t) \rangle}{\langle a^\dagger(t) a(t) \rangle^2}, \quad (5.4)$$

where $a(t)$ and $a^\dagger(t)$ are the single-mode field operators and τ is the correlation time delay. At $\tau = 0$, the second-order correlation function for Fock-states is $g^{(2)}(\tau = 0) = 1 - 1/n$, where the expectation value is $\langle a^\dagger a \rangle = n$, and n is the mean number of photons. For single photons $n = 1$, and it can further be shown that in the other cases (Gerry & Knight, 2004)

$$g^{(2)}(\tau = 0) = 0 \quad \text{Single photon state}$$

$$g^{(2)}(\tau = 0) = 1 \quad \text{Coherent state}$$

$$g^{(2)}(\tau = 0) = 2 \quad \text{Thermal state.}$$

For a single-photon source, after the emission of one photon, it takes time on the order of the Rabi frequency before the system is re-excited. Therefore two concurrent photo-emission events will never be observed in the same time bin in an ideal two-level system. This is so-called *anti-bunching* and leads to $g^{(2)}(\tau = 0) = 0$.

The second-order intensity correlation is experimentally quantified through a Hanbury Brown Twiss (HBT) experiment (Brown & Twiss, 1956). The experimental setup is sketched in figure 5.15(a). The quantum dot emission is sent to on a 50:50 beam splitter and detected at each of the output ports. The quantized nature of photons forbids simultaneous detection events on both detectors if the input is a single photon. In practice, we measure a correlation histogram of coincidence counts between the two detectors as a function of the time delay between detection events. From the steady-state solutions of the optical Bloch equations introduced in section 2.5.2 the

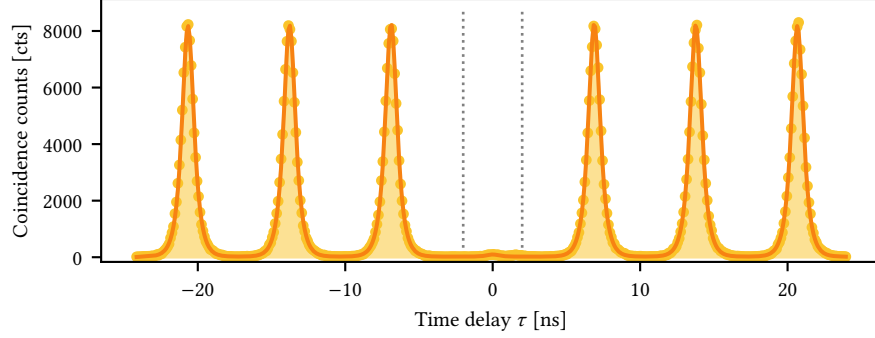


Figure 5.16: Correlation histogram recorded from an HBT experiment displayed in yellow. The orange curve is a fit to the data using equation 5.6. All data presented are raw with no background subtracted.

correlation can be calculated using the quantum regression theorem as introduced in section 2.5.2. In the simplest limit, where the Rabi frequency Ω and the dephasing rate γ_{dp} are much smaller than the spontaneous decay rate γ , it simplifies to

$$g^{(2)}(\tau) = \left(1 - e^{-|\tau|\gamma/2}\right), \quad (5.5)$$

which is plotted in yellow in figure 5.15(b).

Under pulsed excitation, ideally, a single photon is emitted for every excitation pulse. This leads to a correlation histogram of the form in figure 5.15(b) with orange. Correlation peaks appear at times corresponding to the repetition rate of the laser τ_{rep} . The peaks fall off as a two-sided exponential with the decay given by the radiative decay rate of the quantum dot exciton. At $\tau = 0$ the photons are anti bunched and the central peak is suppressed. The single-photon purity is quantified by the ratio $g^{(2)}(0) = A(0)/A(\tau \rightarrow \infty)$ where A is the integrated area under the peak. This ratio tells how much the central peaks are antibunched compared to a bunching peak at long time scales.

5.6.1 Experimental Demonstration of High Purity Single Photons

The HBT experiment is carried out on the spectrally-filtered emission from QD4 under pulsed resonant excitation at π -pulse area. Photons are counted using SNSPDs and the correlation histogram is generated using a time-tagger with a timebin-width of 100 ps. The experimentally measured histogram is plotted in yellow, together with the fit in orange in figure 5.16. The $g^{(2)}(0)$ anti-bunching is pronounced with the nearly absent central peak.

In order to fit the $g^{(2)}(\tau)$ function we need to take the instrument response function (IRF) into account by fitting to the convolution $g^{(2)} \otimes \text{IRF}$. The IRF can be modeled as a

Gaussian and included in the fit (or measured and included). We also account for the contribution from the neighbouring peaks by fitting all 7 peaks simultaneously. The fitting function employed is

$$f(\tau) = \left(a_0 e^{-|\tau-\tau_0|\gamma} + a \sum_n e^{-|\tau-\tau_0-n\tau_{\text{rep}}|\gamma} + c \right) \otimes e^{-\frac{1}{2} \left(\frac{\tau}{\sigma} \right)^2}, \quad (5.6)$$

where $n = [-3, -2, -1, 1, 2, 3]$ is the peak number. The fit parameters a_0 and a are the amplitudes of the center and side peaks respectively, γ is the decay rate, c is an offset accounting for accidental coincidences from background or detector dark counts and σ is the standard deviation of the IRF. We assume that the coincidence counts follow Poissonian statistics to estimate the error on the data.

The area A_0 under the central peak is found by integration of the interval marked by the dotted line in figure 5.16. Before integration we subtract the small contributions from the background offset and the side peaks from the fit function. A similar fit is performed for peaks at $\tau \sim 50 \mu\text{s}$ and integrated to calculate A_{50} . From the areas we estimate that

$$g^{(2)}(0) = \frac{A_0}{A_{50}} = (0.98 \pm 0.13) \%, \quad (5.7)$$

demonstrating very high single-photon purity of the quantum dot emission.

The error on the integrals is estimated numerically by propagating the statistical error and their correlations via the covariance matrix $\text{cov}(x_i, x_j)$ from the fitted parameters. The error on a given function $F(x)$ where x is a set of N parameters, is given by

$$\sigma_F^2 = \sum_i^N \sum_j^N \frac{\partial F}{\partial x_i} \frac{\partial F}{\partial x_j} \text{cov}(x_i, x_j), \quad (5.8)$$

where i and j run over all parameters. Since F here is a numerical integral we can estimate the derivative with respect to each parameter by

$$\frac{\partial F}{\partial x_i} \approx \frac{\Delta F}{\Delta x_i} = \frac{F(x_{k \neq i}, x_i + \sigma_i) - F(x_{k \neq i})}{\sigma_i} \quad (5.9)$$

where, we assume that stepping σ_i away from the optimum parameter is small enough to approximate the derivative (the validity was tested by taking fractional steps of σ_i , leading to no change in the calculated derivative). By using equation 5.8 the error on A_0 and A_{50} can be calculated and propagated to the error on $g^{(2)}(0)$. When the number of counts in the correlation histogram is small, the fits do not converge robustly enough to estimate the errorbars. In those cases, the error bars are estimated as the square root of the integrated coincidence counts under the peak.

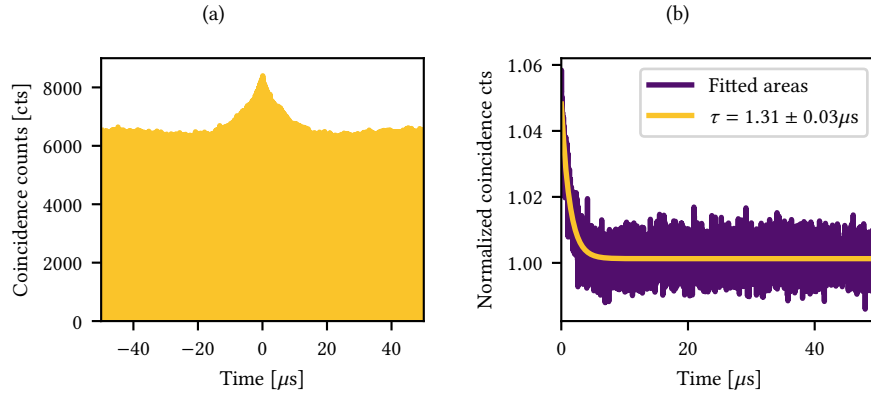


Figure 5.17: Blinking observed in the auto-correlation histogram. (a) The correlation histogram from figure 5.16 shown at long time scales. Note that the individual peaks cannot be distinguished in the figure. (b) The area under a fit to each peak for $\tau > 0$. An exponential is fitted to the areas, showing the time scale of the blinking process.

5.6.2 Blinking

Blinking of the bright exciton to the dark exciton caused by a spin-flip as described in section 2.3 can be directly observed in a $g^{(2)}(\tau)$ measurement by looking the histogram at longer timescales. This is plotted in figure 5.17(a), where we observe a bunching towards $\tau = 0$. This bunching effect can be understood as follows: after a spin-flip from the bright to the dark exciton state, it is possible re-excite the quantum dot, creating a second bright exciton. This second exciton recombines and emit a photon and is shortly after followed by one more photon, resulting from a spin flip back from the dark state to the bright state.

While the effect appears dramatic (i.e. suggesting a large amount of bunching), it is mainly due to an artefact of the time-tagger. The time-tagger (Swabian TimeTagger 20) has a intrinsic delay-time-dependent jitter in coincidence detection, where shorter delay times has lower jitter in comparison to longer delay times. This results in a time-dependent σ for the IRF, which increases with longer delay times. This artefact can be circumvented by calculating the area under the peaks instead of picking the maxima of the peaks. Figure 5.17(b) displayed the area extracted from a fit to each individual peak from $\tau = 0$ to $\tau = 50 \mu\text{s}$. The areas follow an exponential decay with a time scale of $1.31 \mu\text{s}$ which is a typical time-scale for blinking in quantum dots (Johansen et al., 2010). This also illustrates the importance in normalizing the $g^{(2)}(0)$ to a peak at long time-scales in order to correctly estimate the purity.

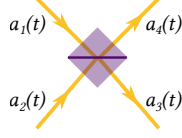


Figure 5.18: Beam splitter with two input modes and two output modes.

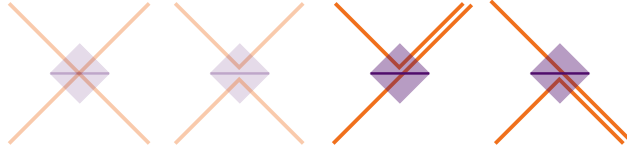


Figure 5.19: HOM quantum interference on a beam splitter. Two indistinguishable photons entering at the input modes will always exit in the same output mode. This means that only the last two configurations are possible.

5.7 PHOTON INDISTINGUISHABILITY

In order to employ a single-photon source for protocols in a quantum network, the single photon stream must contain *indistinguishable* photons. In this section we demonstrate that the single photons emitted from a quantum dot can reach near unity indistinguishability, which is maintained over more than 100 photons in the stream. Our quantum dot source thus has the potential to realize a scalable single photon source.

The indistinguishability of photons emitted by the quantum dot is measured through a Hong-Ou-Mandel (HOM) experiment (Hong et al., 1987). In a HOM experiment, two photons from the single photon stream are interfered on a beam splitter, and the visibility of this interference determine how indistinguishable the two photons are from each other. We therefore start out by briefly summarizing the interference of two single photons on a beam splitter. We consider a 50:50 beam splitter with the modes illustrated in figure 5.18, with two input modes $a_1(t)$ and $a_2(t)$ and two output modes $a_3(t)$ and $a_4(t)$. The modes follow the input-output relations

$$\begin{bmatrix} a_3(t) \\ a_4(t) \end{bmatrix} = \frac{1}{\sqrt{2}} \begin{bmatrix} 1 & i \\ i & 1 \end{bmatrix} \begin{bmatrix} a_1(t) \\ a_2(t) \end{bmatrix}, \quad (5.10)$$

where a $i = e^{i\pi/2}$ phase-shift is introduced upon reflection from the beam splitter.

For two indistinguishable single photons, one sent to each input mode of the beam splitter the state can be written

$$a_1^\dagger(t)a_2^\dagger(t) |0, 0\rangle_{1,2}. \quad (5.11)$$

The beam splitter transformation leads to the output state

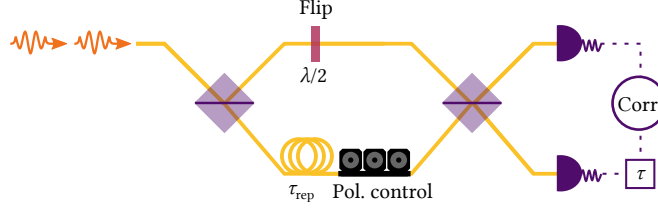


Figure 5.20: Schematic of a Hong Ou Mandel experiment, where two photons interfere in a Mach-Zehnder interferometer. The lower arm is delayed by τ_{rep} in a fiber delay. Parallel polarization of the light in the two arms is ensured by polarization paddles. A half-wave plate is introduced in the upper arm to change between co- and cross-polarized configurations. The number of photons exiting the interferometer is detected and their correlation is measured.

$$\xrightarrow{\text{BS}} \frac{i}{2} (a_3^\dagger(t)a_3^\dagger(t) + a_4^\dagger(t)a_4^\dagger(t)) |0, 0\rangle_{3,4}. \quad (5.12)$$

The only possible outcome for both photons to go to the same output port as illustrated in figure 5.19. This is an interference phenomenon that only takes place when the two photons are identical, in terms of frequency, temporal shape, polarization, and arrival time. In this case, no coincidence detection events will occur at the two outputs of the beam splitter. This is therefore an experimental measure of the indistinguishability of a single-photon source. HOM interference of two photons emitted by a quantum dot under repeated excitation is also a good measure for quantifying the coherence of the single-photon source (i.e. its ability to repeatedly generate indistinguishable photons).

We employ an unbalanced Mach-Zehnder interferometer for these measurements as illustrated in figure 5.20. The time delay τ_{rep} in one of the arms is matched with the repetition rate of the excitation laser. In this way two consecutively emitted photons interfere on the second beam splitter. To determine the degree of interference, the HOM experiment is performed both in a distinguishable and in an indistinguishable configuration. The two photons are made distinguishable in polarization by introducing a half-wave plate placed in the upper arm (see figure 5.20). We refer to these two measurements as the co-polarized (interfering) and cross-polarized (non-interfering) configurations.

We measure the second-order cross-correlation between the two output modes $a_3(t)$ and $a_4(t)$

$$G_{3,4}^{(2)}(t, \tau) = \langle a_3^\dagger(t)a_4^\dagger(t+\tau)a_4^\dagger(t+\tau)a_3^\dagger(t) \rangle. \quad (5.13)$$

$G_{3,4}^{(2)}(t, \tau)$ is found by applying the quantum regression theorem and solving the optical Bloch equations as described in section 2.5.2. The central peak where the two photons are interfering is given by (Madsen et al., 2014)

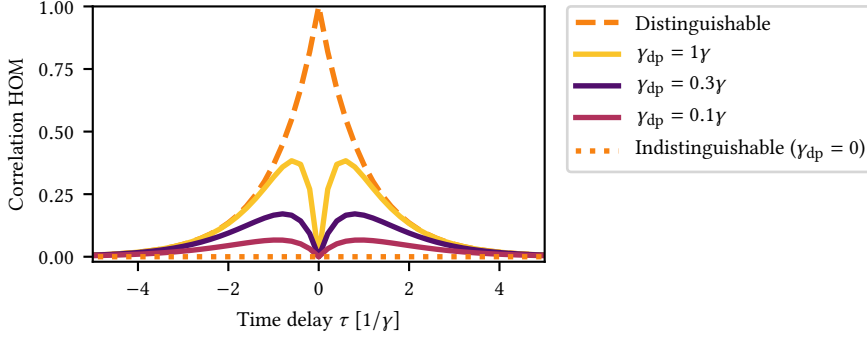


Figure 5.21: The HOM-interference peak from equation 5.7 with different dephasing γ_{dp} rates relative to the radiative decay rate γ . The distinguishable case is represented with a double sided exponential.

$$G_{3,4}^{(2)}(\tau) = \frac{1}{4\gamma} e^{-\gamma|\tau|} (1 - e^{-2\gamma_{dp}|\tau|}), \quad (5.14)$$

where γ is the decay rate and γ_{dp} is the pure dephasing rate. In the case of no dephasing ($\gamma_{dp} = 0$), this expression becomes 0, which is the fully indistinguishable case. In figure 5.21 $G_{3,4}^{(2)}(\tau)$ is plotted for the $\tau = 0$ region using different dephasing rates, together with the fully distinguishable case represented as a two-sided exponential decay and plotted with a dashed line.

We quantify the indistinguishability by the HOM visibility

$$V = \frac{A_{\perp} - A_{\parallel}}{A_{\perp}}, \quad (5.15)$$

which compares the area of the peaks in co- and cross-polarized configuration denoted by A_{\parallel} and A_{\perp} respectively.

We call the visibility extracted directly from correlation histogram measurements the *raw visibility* V_{raw} . We will show later on that the raw visibility is primarily limited by the single photon purity, mainly introduced by laser impurity. This imperfection is introduced in the excitation setup and can be improved using optimized excitation methods: pulse bandwidth engineering (in section 6.1) or wavefront corrections (Olesen, 2020). We therefore correct for this and extract the intrinsic visibility of the interference. Further, the intrinsic visibility of the source is affected by the performance of the HOM interference setup. Including both single photon impurity and setup imperfections the remaining effects are (1) the classical interference fringe contrast $(1 - \epsilon)$ of the interferometer, (2) imperfect HOM interference due to an imbalanced reflection (R) and transmission (T) coefficient of the beam splitter, and (3) impurity of the single photons $g^{(2)}(0)$. These will affect the coincidences in the central peak in the following way (Santori et al., 2002)

$$A_{\parallel,\perp} \propto (R^3T + RT^3)[1 + 2g^{(2)}(0)] - 2(1 - \epsilon)^2 R^2 T^2 V. \quad (5.16)$$

For an ideal source emitting fully indistinguishable single photons, we know the intrinsic visibility V , which allows us to write two equations $A_{\parallel}(V = 1)$ and $A_{\perp}(V = 0)$. Using equation 5.15 we can express the ideal visibility

$$V_{\text{ideal}} = \frac{2RT(1 - \epsilon)^2}{(R^2 + T^2)[1 + 2g^{(2)}(0)]}. \quad (5.17)$$

The ideal visibility is used as a normalization of the measured raw visibility leading to the expression for the intrinsic visibility

$$V = \frac{V_{\text{raw}}}{V_{\text{ideal}}} = \frac{(R^2 + T^2)[1 + 2g^{(2)}(0)]}{2RT(1 - \epsilon)^2} V_{\text{raw}}. \quad (5.18)$$

The intrinsic visibility allows a comparison of the indistinguishability across different interferometric setups.

5.7.1 Short and Long Timescale HOM

We operate QD₄ under π -pulse excitation as the source of single photons and perform a HOM interference experiment. Two consecutively emitted photons are interfered in the HOM-setup, and the coincidence counts are recorded. The resulting coincidence histogram is shown in figure 5.22(a), displaying the central interference region and two side peaks, corresponding to a time delay where the photons do not interfere. The HOM interference peaks can be modeled with a similar multi-peak fitting function used for $g^{(2)}(\tau)$ in equation 5.6, with the additional contribution of dephasing described by equation 5.14 added to the central peak. The resulting fits to the data are plotted in figure 5.22(a). A similar fit is performed for the cross-polarized configuration and the fits to the central peaks of the co- and the cross-polarized data are shown in figure 5.22(b) in purple and orange respectively.

We observe clear suppression of the peak in the co-polarized configuration, in comparison to the cross-polarized configuration. The residual counts in the central peak of the co-polarized configuration could be due to: 1) presence of laser background photons (weak coherent states) due to imperfect single photon purity, 2) imperfections in the HOM interferometer, and 3) partial distinguishability of the emitted single-photons.

The measurement presented in figure 5.22 was performed with the time delay corresponding to the repetition period of the excitation laser. By adding a longer time delay $N\tau_{\text{rep}}$ in figure 5.20 and using the 145 MHz repetition rate laser, we interfere photons further away from each other in the photon stream. Our experimental setup

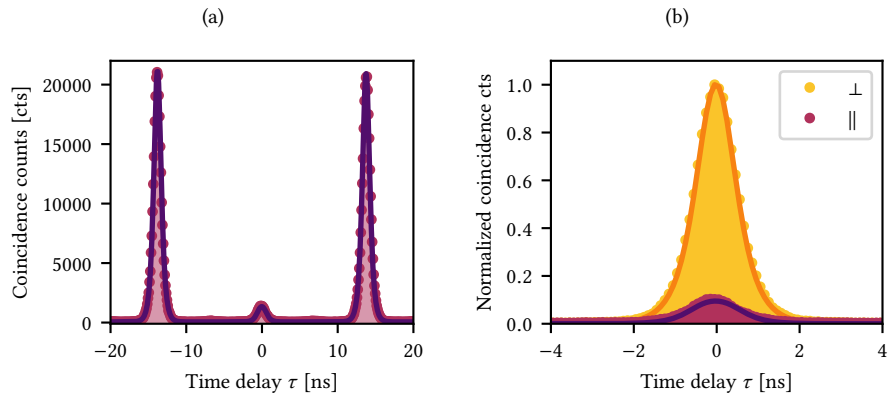


Figure 5.22: HOM interference coincidence histograms. (a) Co-polarized configuration showing the central and two side peaks, together with a fit to the multi peak function in equation 5.6, with the addition of equation 5.7 to the central peak. (b) Central peaks in the co- and cross polarized configuration. Both co- and cross polarized peaks are normalized to at peak a longer time scale (~ 500 ns), and rescaled to the $\tau = 0$ value on cross polarized configuration. All data presented are raw with no background subtraction.

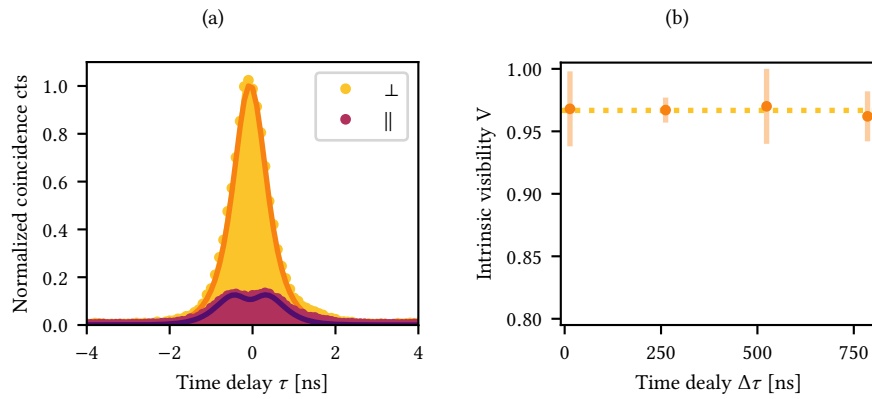


Figure 5.23: HOM interference at long time scales. (a) Interference peaks in co- and cross-polarized configuration, for a long time delay of $114\tau_{\text{rep}} = 785.7$ ns. The data presented are raw with no background subtraction. (b) Calculated intrinsic HOM interference visibility for four different time delays. The integrated peak areas are corrected for detector after-pulsing (see main text).

allows four delays of $N = \{1, 38, 76, 114\}$, number of pulse cycles that separate the two photons. Therefore, in the configuration with the longest delay, we interfere photon number 1 with photon number 115. The HOM interference histogram for this long time delay is plotted in figure 5.23(a). The area under the co-polarized peak is almost unchanged compared to figure 5.22(b), demonstrating maintained indistinguishability all the way across more than 100 photons. The peak is broadened a bit compared to the short delay due to a slight amount of increased dephasing, which is also apparent from the small dip appearing in the center.

The HOM experiments presented in figure 5.22 and 5.23 were recorded using the APDs. In order to estimate the HOM visibility correctly from the histograms, we need to correct for detector imperfections, due to after-pulsing in the detector instrument response. This was done following the methods described in C. Wang et al., 2017 using the formalism in Uppu et al., 2016. Our detectors has an after pulsing probability of 1.5 %, which leads to a correction to the visibility of 4 %. Figure 5.23(b) shows the corrected intrinsic visibility for the four-time delays. We see that the intrinsic visibility is almost perfectly constant at all time delays, demonstrating the excellent coherence of the source. The HOM visibility measurement was repeated on the same quantum dot using the SNSPDs which do not have any measurable after-pulsing effects. Such a measurement is shown in figure 5.25(b) and confirms the after-pulsing-corrected value for the visibility. All remaining HOM-measurements presented in this thesis were recorded using the SNSPDs.

5.7.2 State-of-the-art HOM visibility

In the above section, we have demonstrated excellent intrinsic indistinguishability of the single photons emitted from QD₄ maintained over long time scales. After these measurements were performed, we made further improvements to our HOM experiment to reduce the interferometer imperfections and to precisely measure its classical interferometric visibility.

We have introduced the following modifications and optimizations to the interferometer. We employ a fiber beam-splitter for the interference, and it is therefore important to properly stabilize all fiber elements to not introduce any polarization shift during measurements. All fibers were carefully secured by taping them to the optical table ensuring mechanical stability. The path length difference of two arms of the interferometer were re-aligned using the fast APDs, and hence time-matched up to 40 ps.

Before each HOM measurement, the polarization overlap of the two interferometer arms is maximized using fiber paddles. This was previously done by maximizing the classical interference visibility of the cw-laser passing through the setup while introducing path length modulation by tapping the optical table with the finger. To improve this procedure, two new components were introduced to the setup as sketched in figure 5.24(a). A piezoelectric mirror was installed, which allows modulation of the interferometer path length in a controlled way. From this we can optimize and measure the classical interference visibility $(1 - \epsilon)$ very precisely. Secondly, the $\lambda/2$ waveplate

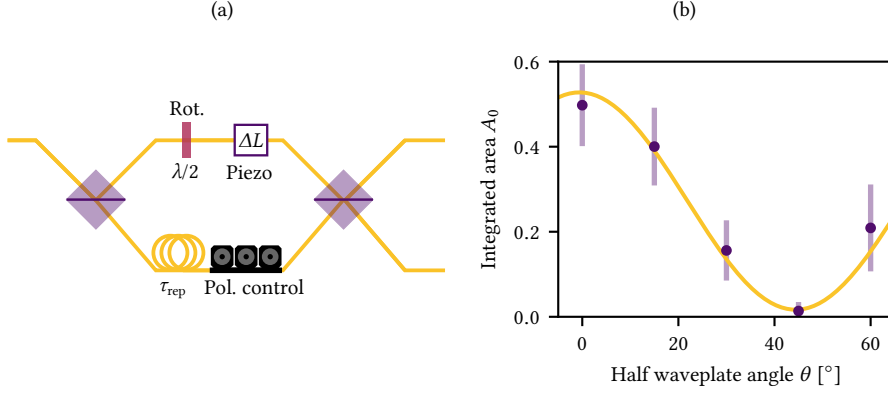


Figure 5.24: (a) HOM interferometer with the $\lambda/2$ waveplate mounted on a rotation stage. A piezoelectric mirror is added in the upper arm to modulate the path length that adds a phase shift in one of the arms. The piezo element is employed during alignment of the interferometer to maximize the classical interference contrast. (b) HOM visibility fringe measured at various waveplate angles is fitted to equation 5.19 shown with a solid line. The errorbars here are the Poissonian errors on the number of coincidence counts in the peaks.

was mounted on a rotation stage. This allows to map out the HOM visibility fringe as a function of waveplate angle θ . In figure 5.24(b), the resulting area under the central peak is plotted as a function of waveplate angle. The area follows

$$A(\theta) = A_m - A_c \sin^2(2\theta + \phi) \quad (5.19)$$

where A_m and A_c are related to the raw visibility as $V_{\text{raw}} = A_c/A_m$ and ϕ is an offset in the wave plate angle defined by the polarization alignment reached using the fiber paddles. The fit to this equation is plotted along with the data points. By calculating the visibility from the fit parameters, we ensure to always measure the maximal fringe contrast, and therefore to account for small offsets in the polarization alignment. We note that the fitted fringe in figure 5.24(b) has a very small phase offset of $\phi < 1^\circ$, which shows the robustness of the polarization alignment using the piezoelectric mirror.

In figure 5.25(a), we present the HOM interference histograms using the optimized setup and single-photon emission from QD₄. We see that interference in the co-polarized configuration is almost perfect, exhibiting close to complete suppression of the peak. Figure 5.25(b) displays a single photon purity measurement performed in connection with the HOM measurement. The calculated $g^{(2)}(0)$ value given in the plot is marginally higher than earlier reported due to a slightly more laser background.

Since this measurement is performed on the SNSPDs, we can calculate the raw HOM visibility directly from the area under the fitted curves, with the minimal background

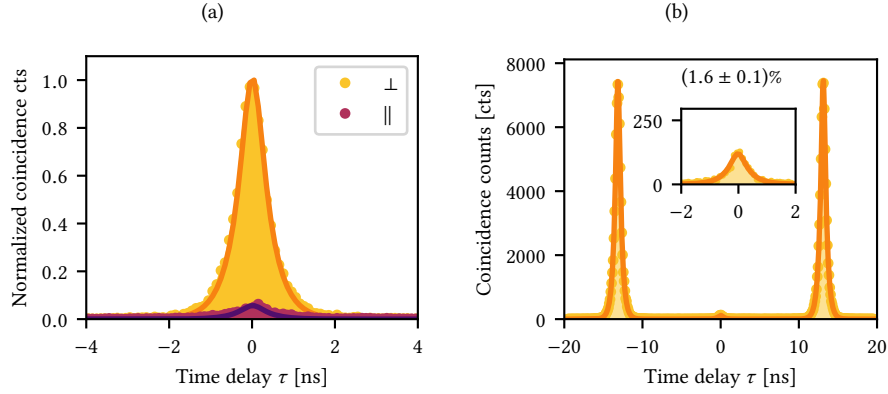


Figure 5.25: Coincidence histograms shown with dots and fit to the multi-peak function in equation 5.6 shown with solid lines. (a) HOM interference measurement, recorded under optimized excitation pulse length using the optimized interferometer. (b) $g^{(2)}(\tau)$ auto-correlation measurement. The number quoted is the purity calculated from the area under the fit with the minimal background and side peaks subtracted. The measurement was recorded in the same experimental run as in (a). All data presented are raw with no background subtracted.

Parameter	Value	Error	V_{raw} correction
R	0.476	0.001	0.5%
T	0.524		
$1 - \epsilon$	0.998	0.002	0.4%
$g^{(2)}(0)$	0.016	0.001	3%

Table 5.2: Breakdown of the contributions of the different parameters when correcting the raw visibility in equation 5.20 to the intrinsic visibility from equation 5.21.

subtracted. The raw visibility is

$$V_{\text{raw}} = (94.6 \pm 1.9) \%. \quad (5.20)$$

The uncertainty is propagated from the fit parameters in a similar way as used for $g^{(2)}(\tau)$ in equation 5.8. The raw visibility could be improved by having a better excitation alignment reaching $g^{(2)}(0) < 1$ percent as in figure 5.16. We correct for the impurity and setup imperfection to extract the intrinsic visibility. Using carefully calibrated contributions of all correction factors summarized in table 5.2, we reach an intrinsic visibility of

$$V = (98.4_{-2.0}^{+1.6}) \%. \quad (5.21)$$

This high intrinsic visibility is among the highest reported to date for quantum dot single-photon sources. Table 5.3 summarizes reported intrinsic visibilities from different

Ref.	This work	Ding et al., 2016	Tomm et al., 2020	Somaschi et al., 2016	Schöll et al., 2019
V	98.4 %	98.5 %	96.7 %	98.6 %	95 %
$\Delta\tau$	13 ns	12 ns	13 ns	2 ns	2 ns
Struct.	PCW	Micropillar	Microcavity	Micropillar	Planar sample

Table 5.3: Summary of reported intrinsic HOM visibilities V measured at with a time delay of $\Delta\tau$ between the two interfered photons.

quantum dot devices, and our performance is clearly comparable. Here, we emphasize that our experiment was performed with a $\Delta\tau = 13$ ns time delay, similar to both Ding et al., 2016 and Tomm et al., 2020. In contrast, in Somaschi et al., 2016 and Schöll et al., 2019 the interference was performed with only 2 ns delay which leads to overlap of the central peak and the side peaks of the interference histograms. This leads to a large background contribution from the side peaks and estimating of the small area of central peak is less reliable, and highly dependent on the background correction. Furthermore, the number of integrated coincidence counts in Somaschi et al., 2016 and Schöll et al., 2019 is not very high⁽¹⁾, which makes robust fitting of the peaks challenging. These facts should be taken into account when assessing the quality of the experiment and comparing the reported values to this work.

Our experimentally measured intrinsic visibility is remarkably close to the fundamental limit on the visibility limited by phonon decoherence, as was calculated in Tighineanu et al., 2018. For a 2D suspended membrane this limit is $\sim 99\%$ at 1.6 K. This high intrinsic interference visibility demonstrates almost perfect indistinguishability of our single-photon source operated under resonant π -pulse excitation.

* * *

In this chapter we have presented a state-of-the-art single-photon source, and detailed the full recipe to reach high performance, all the way from device and quantum dot characterization to high efficiency operation of indistinguishable single photons. We started this chapter off by detailing how a suitable quantum dot is identified. We demonstrated 10 MHz operation of the source and fully accounted for all possible losses in the setup. The high quality of the quantum dots coupled to the PCW was demonstrated using resonant transmission measurements, exhibiting near lifetime-limited linewidths. We have demonstrated high purity of the quantum dot source in an HBT experiment and reached intrinsic HOM interference visibilities almost at the fundamental limit of phonon decoherence. The high visibility is maintained over more than 100 photons on the single-photon stream. This realizes a scalable single-photon source that can be employed for e.g. boson sampling algorithms (Uppu et al., 2020).

(1) Peak value of their reference peak is ~ 300 cts where we have ~ 1500 cts.

CHAPTER


OPTIMIZING RESONANT EXCITATION SCHEMES

Two approaches to resonant excitation schemes, which has the potential to improve the single-photon quality are studied and discussed.

In the previous chapter, we saw excellent single-photon properties of the photons emitted from a quantum dot embedded in a PCW. We ended the chapter by presenting intrinsic HOM interference visibilities exceeding 98 %. This measurement was performed with an optimized excitation laser bandwidth. In this chapter, we are going to investigate the effect of changing the excitation laser bandwidth on the single-photon purity and HOM visibility. We will show how the optimal pulse bandwidth was found, constituting a highly efficient resonant excitation scheme.

In the second section, we will present another widely employed approach of coherent excitation, called *two-photon resonant excitation*. This scheme allows coherent excitation while being detuned from the single-photon transitions leading to nearly perfect laser background suppression and hence, extremely high single-photon purity (Schweickert et al., 2018). While this scheme appears appealing, we will see that the cascaded decay limits the indistinguishability of the emitted photons.

6.1 OPTIMIZED EXCITATION LASER PULSE BANDWIDTH

The efficiency of resonant excitation of a quantum dot depends on several system parameters, e.g. the laser polarization as discussed in section 5.3. As mentioned earlier we typically narrow the spectral bandwidth of the excitation laser pulse to more efficiently excite the quantum dot transition and suppress laser background. The

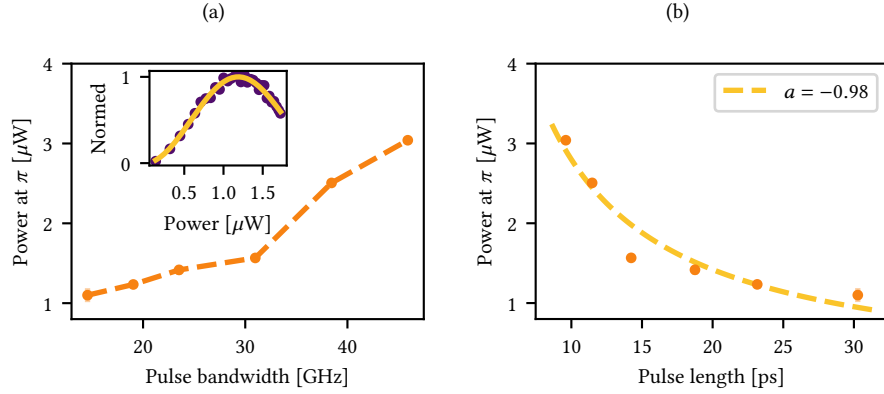


Figure 6.1: Power required to reach π -pulse excitation, as a function of pulse bandwidth (a) and pulse length in time (b). Inset in (a) is an example of a Rabi oscillation power series, fitted to a sine squared to extract the π -pulse power. The power given is measured at the power meter in 4.3. (b) The dashed line is a fit to $P_{\text{avg}} = bT^{-a}$, with the extracted value for a displayed in the legend.

spectral bandwidth of the pulsed excitation laser is narrowed using a pulse stretcher (see section 4.1.1), which in turn elongates the pulse in time. At longer excitation pulses in time, there is an increasing probability to excite the quantum dot twice within one laser pulse. This leads to the emission of two photons within one time window and hence lowers the single-photon purity, i.e. increases $g^{(2)}(0)$. This effect was modeled and measured experimentally in Fischer et al., 2018. Therefore, there is a limit to the stretching of the excitation pulses before re-excitation cancels the benefit of narrowing the bandwidth.

In this section, we are going to experimentally investigate the dependence of the single-photon purity and HOM visibility, on the excitation pulse length.

6.1.1 Pulse Bandwidth Dependent Single-photon Purity and Indistinguishability

We again employ QD4 under pulsed resonant excitation with the emission filtered using the etalon, for two series of experiments. For each series, the laser bandwidth is changed and the following three measurements are recorded. (1) A power-dependent Rabi oscillation series to identify π -pulse excitation power, (2) an HBT experiment and (3) a HOM experiment both at π -pulse excitation. Our pulse stretcher accommodates bandwidths in the range $\Delta f = \{11 \text{ GHz} - 100 \text{ GHz}\}$, which correspond to the excitation pulse lengths $T = \{4 \text{ ps} - 40 \text{ ps}\}$.

We start by checking how much power is needed to reach π -pulse area, depending on the laser bandwidth. Each Rabi oscillation data set is fitted to a squared sine, and the extracted power at π -pulse is plotted as a function of laser bandwidth in figure 6.1(a). At shorter pulse lengths (much shorter than the lifetime of the quantum dot),

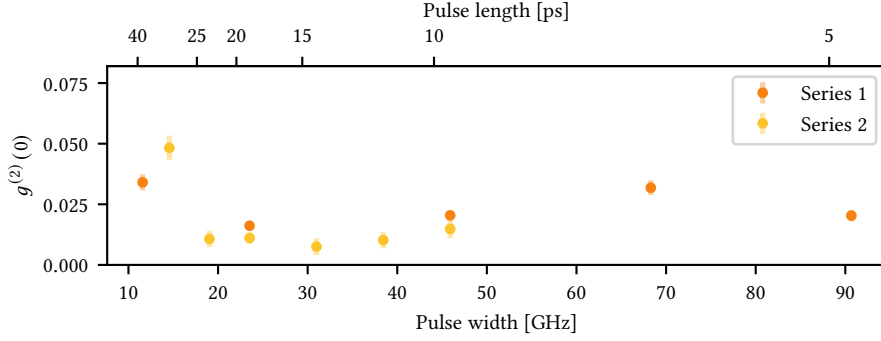


Figure 6.2: Two series on QD4 of single photon-purity $g^{(2)}(0)$ extracted from autocorrelation histograms of an HBT measurement, for two series of laser bandwidths. The $g^{(2)}(0)$ is extracted following the methods in section 5.6.

the wider bandwidth of the excitation pulse results in higher pump powers to reach π -pulse excitation. In figure 6.1(b) the bandwidth axis is converted to pulse length in time, assuming a Gaussian time-bandwidth product. The peak power of the pulse P_{peak} and pulse length T are related through the pulse area $\Omega T = \pi$, where $\Omega \propto \sqrt{P_{\text{peak}}}$ and hence $P_{\text{peak}} \propto T^{-2}$. Since the power, measured on a power meter is a time average over the laser pulses, the relation is $P_{\text{avg}} \propto T^{-1}$. A fit to the function $P_{\text{avg}} = bT^{-a}$, is displayed with a dashed line and the extracted fit parameter a is close to the expected value of -1 .

The effect of the increased laser power at wide bandwidths can be seen in the single-photon purity. For each of the auto-correlation histograms, the $g^{(2)}(0)$ value is extracted following the methods described in section 5.6. In figure 6.2 we present the extracted single-photon purities as a function of pulse bandwidth for both series 1 and 2. The effect of re-excitation is only just coming into effect at the longest pulse lengths (i.e. narrowest frequency bandwidths). Furthermore, at very short pulses, or at the largest frequency bandwidths, the single-photon purity $g^{(2)}(0)$ shows an increasing trend again. We find the optimal point for this quantum dot is reached at around 23 GHz bandwidth, corresponding to approximately 19 ps pulse length.

In collaboration with the Theoretical Quantum Optics group at the Niels Bohr Institute, we are investigating this effect. The optimal point between the two competing limits of narrow and wide laser bandwidths was predicted by a theoretical model developed by Johannes Bjerlin. The theoretical model is based on the wave-function ansatz presented in Das et al., 2019 which can simulate $g^{(2)}$ for a two-level system including two excitations. This formalism further allows us to include the effect of spectral filtering, which is important to model the experimentally recorded data. The addition to this formalism is to include the laser background coupling into the

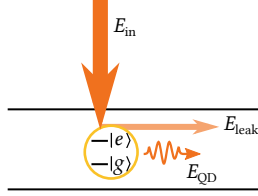


Figure 6.3: Illustration of the addition to the model in Das et al., 2019, to include laser background leaking into the waveguide, when exciting the quantum dot.

waveguide when the quantum dot is excited, as illustrated in figure 6.3. The resulting field in the waveguide is described by

$$E_{\text{wg}} = E_{\text{QD}} + E_{\text{leak}}, \quad (6.1)$$

where $E_{\text{leak}} = E_{\text{in}}|x|e^{i\phi}$ is the amount of field leaking into the waveguide without exciting the quantum dot. Here $|x|$ is a leakage amplitude and ϕ is the phase between the incoming and leaked light. The leakage amplitude relates to the experimental laser impurity described in section 5.3.2 as $\xi = E_{\text{leak}}/E_{\text{QD}}$, assuming that all laser background couples through the waveguide. It is work in progress to fit the experimental data to this model.

A HOM interference experiment was performed in conjunction with the $g^{(2)}$ measurements, and the raw visibility was extracted following the methods described in section 5.7. The extracted raw visibilities are plotted in figure 6.4 for the two data series. That the raw visibility is mainly limited by the single-photon purity is seen from the overall shape, which follows the $g^{(2)}(0)$ data points figure 6.2. The optimum raw visibility of 94 % is therefore reached in the same region of laser bandwidths.

We repeat the measurement series for a different quantum dot namely QD1 from the previous chapter 5. We choose laser pulse bandwidths equivalent to series 2 for QD4. The resulting single-photon purity $g^{(2)}(0)$ and raw HOM visibilities are displayed in figure 6.5 together with the corresponding data from figures 6.2 and 6.4. We observe a consistent trend in $g^{(2)}(0)$ across the two quantum dots but with the values offset. This offset could be explained by the higher impurity also observed under resonant spectroscopy of QD1 in section 5.3. The measured impurities recorded with the power series at the optimal laser pulse bandwidth was $\xi_{\text{QD1}} = 0.011$ and $\xi_{\text{QD4}} = 0.006$.

Lastly, we note that the three data sets reported here were recorded over a time span of approximately a month, with a thermal cycle between series 1 and 2. The consistency of the measurements highlights the stability and repeatability of the experimental setup (that had to be realigned) and of the quality of our quantum dot single-photon source.

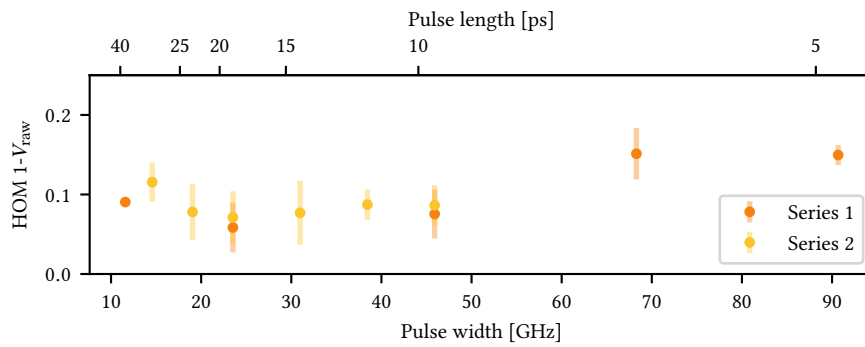


Figure 6.4: Two series on QD4 of interference visibility extracted from correlation histograms from HOM measurements, for two series of laser bandwidths. The raw visibility V_{raw} is extracted following the methods in section 5.7.

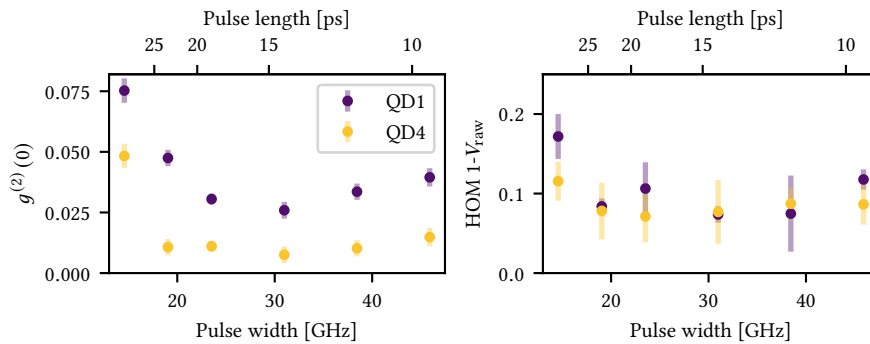


Figure 6.5: Comparison of two series of $g^{(2)}(0)$ and HOM visibility on two different quantum dots. The data series in yellow is the same as series 2 in figures 6.2 and 6.4. Note the narrower range of laser pulse bandwidths displayed here.

6.2 TWO-PHOTON RESONANT EXCITATION

In this section, we are going to investigate coherent detuned excitation of the quantum dot realized through the doubly excited quantum dot state, the biexciton $|XX\rangle$ introduced in section 2.3. It consists of two electron-hole pairs, which due to Coulomb forces between the two electrons lead to a smaller energy difference between the $|XX\rangle$ and the $|X\rangle$ than the exciton energy, i.e., between $|X\rangle$ and the ground state $|0\rangle$. The biexciton can be resonantly excited via two-photon excitation through an intermediate virtual level. The photon energy of the excitation laser corresponding to half the energy difference between the ground state $|0\rangle$ and the biexciton state $|XX\rangle$, as illustrated in figure 6.6(a). The biexciton state decays to the ground state in a cascade process, first to the exciton state followed by a decay to the ground state by emitting two photons of energy E_{XX} and E_X , respectively. Since the excitation process requires two photons at the same frequency in the same time bin, the biexciton is most efficiently populated using high power pulsed excitation, leading to the strong but spectrally distinct laser background.

6.2.1 Two-photon Resonant Spectroscopy

We start by presenting spectroscopy measurements of QD₄ using the pulsed two-photon resonant excitation scheme, to characterize the emission from this process. Figure 6.6(b) shows the spectrally resolved quantum dot emission under pulsed two-photon resonant excitation. We see the strong laser background spectrally centered between X and XX emission lines. Note that the laser pulse is stretched to 20 ps in order to minimize the spectral bandwidth, such that the tails of the laser background do not overlap with the emission lines, which can easily be filtered out.

Since the biexciton is also a neutrally charged state, it appears at the same bias voltage as the neutral exciton, which for this sample is around 1.24-1.26 V. By recording the spectra at regularly spaced voltage steps within this range (see figure 6.7), we can see the exciton and biexciton emission lines tune with the same slope. With the voltage map, the exciton and biexciton transitions can be robustly identified. They typically appear at ~ 2 nm spectral distance, has the same tuning slope, and an identical turn-on and -off voltage points. In figure 6.7 the identified emission lines X and XX are marked and can be distinguished from a third unidentified line, at a higher wavelength.

By filtering either the X or XX emission line we can use this scheme as an effective laser background-free source. In general, the two-photon excitation scheme requires higher excitation power. For a sample as this one, with a relatively high density of quantum dots, the laser can quasi-resonantly excite other quantum dots in the vicinity, which results in unwanted emission that needs to be spectrally filtered out.

Figure 6.8 shows a time-resolved lifetime measurement for the X and XX transitions, respectively. The decay rates of the two transitions are very different, in fact, the decay rate of the biexciton is almost exactly twice the rate of the exciton transition. This is expected as the biexciton state has two decay channels (i.e. the two different exciton dipole states) while each of the exciton states has only one as illustrated in the right

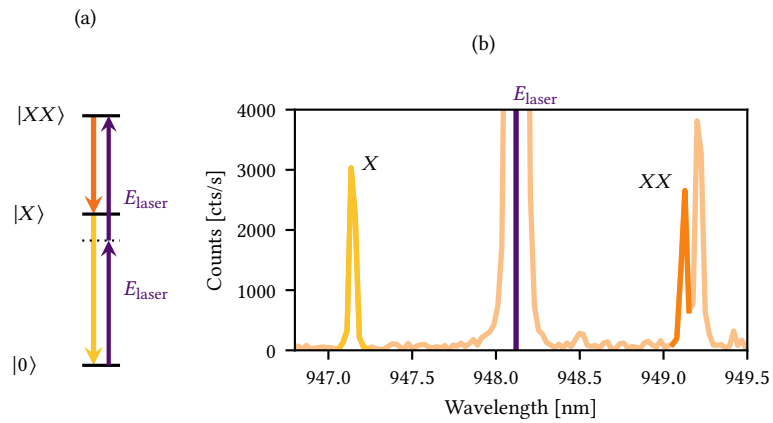


Figure 6.6: (a) Illustration of the two-photon resonant excitation scheme, leading to different emission energies for the X and XX transition. (b) Spectrally resolved emission under two-photon resonant excitation. The laser frequency center is indicated by a purple line, and quantum dot X and XX emission lines are also marked.

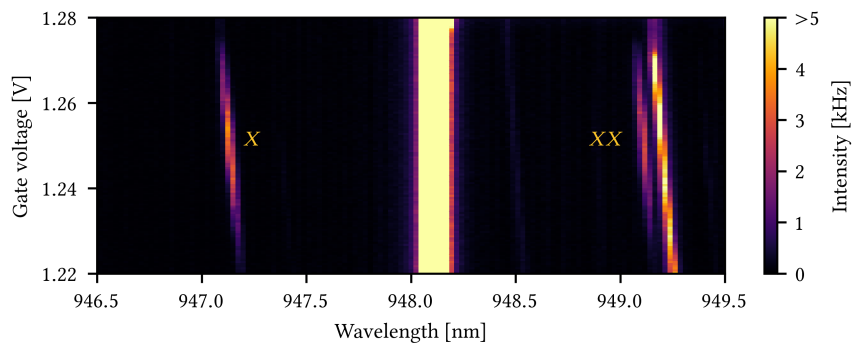


Figure 6.7: Spectrally resolved voltage tuning map, showing the charge plateau of both the X and XX emission lines. They tune at the same slope, and exhibit the same gate voltage turn-on and -off points.

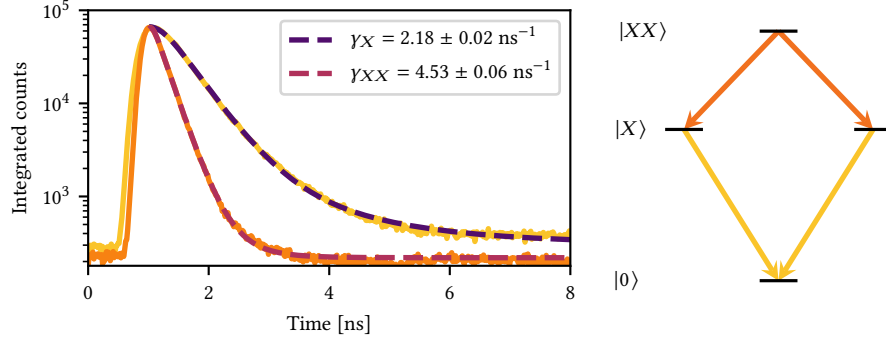


Figure 6.8: Time-resolved measurement of the exciton X and biexciton XX emission. The data are fitted to exponential decays and the extracted lifetimes are shown in the legend. The energy level diagram illustrates the one and two decay channels for X and XX respectively.

panel of figure 6.8. The cascaded nature of the decay is also visible in the rise time of the exciton emission time-correlation histogram. We observe a slightly longer rise time for X histogram since this state is populated only when the $|XX\rangle$ state has decayed. This effectively gives more timing jitter for the X emission than the XX emission, and therefore it is typically the XX transition that can be employed as a single-photon source.

To demonstrate the coherence of the two-photon excitation scheme, we record Rabi oscillations of both the X and XX transitions. If the detuning from the single-photon transition is sufficiently large, the state population follows the same optical Bloch equations, shown in Linskens et al., 1996, with an effective Rabi frequency between the ground state and the $|XX\rangle$ state. The effective Rabi frequency is $\Omega_{\text{eff}} \propto \Omega_{\text{Laser}}^{(1)} \Omega_{\text{Laser}}^{(2)}$ when two laser photons are involved in the process. As the two laser frequencies are identical, the optical power P is proportional to Ω_{Laser} . In contrast, resonant excitation of the exciton state has a square root dependence, i.e. $P \propto \sqrt{\Omega_{\text{Laser}}}$.

We record power-dependent Rabi oscillations and plot the recorded emission intensity, corrected for detector efficiency in figure 6.9. We attribute the peak emission to an effective pulse area of π . Using the two-photon Rabi model the data are fitted and we extract peak emission of (0.91 ± 0.01) MHz and (0.64 ± 0.02) MHz for X and XX respectively. The nominal power needed to reach π -pulse excitation for the two-photon excitation is around $40 \mu\text{W}$ whereas the resonant excitation scheme only requires $\sim 1 \mu\text{W}$ to reach π -pulse area. However, this does not limit the laser impurity as seen in figure 6.9, since the laser background is very efficiently filtered out. Note that at low powers, very few background counts are recorded, and the impurity estimation is not valid ⁽ⁱ⁾. We observe a slightly higher single-photon intensity from the X than

(i) This can be avoided by integrating counts over a longer time.

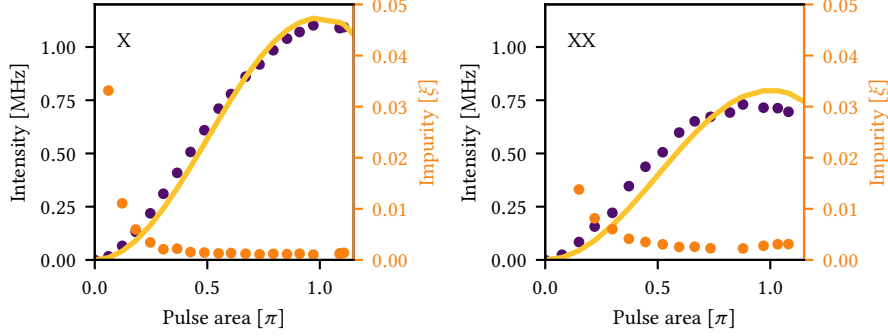


Figure 6.9: Rabi oscillations recorded for the X and XX transitions under two-photon resonant excitation. The data is fitted with a squared sine using that $P \propto \sqrt{\Omega_{\text{Laser}}}$ where we attribute the peak intensity to π -pulse area. The impurity was calculated using equation 5.2, which breaks down for very low laser background.

the XX transition. The two data sets are not collected in the same measurement runs and could have small variations in the collection efficiency.

The displayed measurements are the best effort performance in terms of efficiency and carefully corrected for detection efficiencies and fiber losses, the same way as figure 5.11. In order to be able to fully compare the count rates between the two different excitation methods, we take into account the different types of filters used for the measurements. For the two-photon excitation scheme, the grating filter was used instead of the etalon to avoid leakage of the laser and the emission from other quantum dots. If the Etalon filter was employed, then these frequencies could be transmitted by the frequency comb of transmission windows. The corrected intensities are 1.36 MHz and 0.96 MHz are lower by more than a factor of 3 in comparison to resonant excitation, indicating a much more inefficient excitation process. Note that for the measurements presented here the laser repetition rate was 76 MHz while the ~ 10 MHz single-photon rate reported in section 5.4 employed a laser repetition rate of 145 MHz and we should compare to ~ 5 MHz.

6.2.2 Single-photon Purity and Indistinguishability

We have seen above, that we can coherently excite the biexciton state validated by observing Rabi oscillations of both the exciton and biexciton photons. We now test the single-photon properties of the emitted photon from the exciton and biexciton transitions using QD₄ under two-photon π -pulse excitation.

First, we perform an HBT experiment to measure the single-photon purity as described in section 5.6. Since the excitation laser is far detuned from the two individual transitions, we expect vanishing $g^{(2)}(0)$ values as was reported in Schweickert et al., 2018, where for the XX transition $g^{(2)}(0) \sim 10^{-5}$ was demonstrated. Both X and XX transitions are filtered using the grating filter and the recorded coincidence histograms

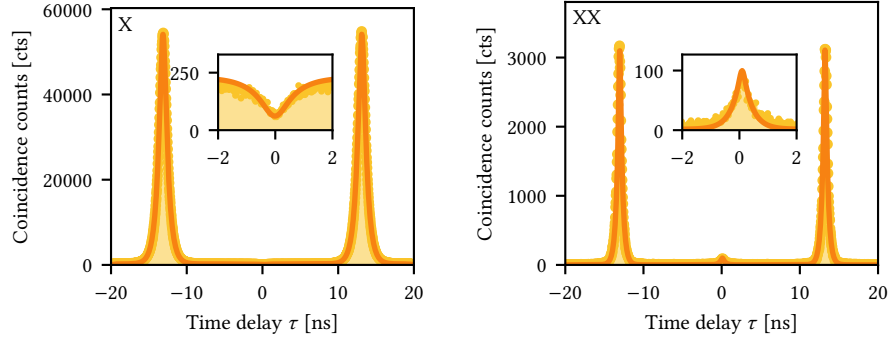


Figure 6.10: Autocorrelation histograms recorded in an HBT experiment for the exciton X and biexciton XX transition in the two panels respectively. The data are fitted equation 5.6, but as described in the main text this does not describe the behavior. Note the factor of 20 scaling between the two data sets, due to different integration times.

are displayed in figure 6.10 together with a fit to the multi-peak function in equation 5.6. We immediately notice a curious feature for the central region of the X histogram, shown in the inset. The coincidence events in this region seem to exhibit a dip, below the background level. The non-zero background level stems from a second, much slower decay rate of the side peaks due to the dark exciton decay. In order to fully resolve the dip, the HBT coincidence counts were integrated longer, hence the large difference in maximum counts of the side peaks between the X and XX histograms. In contrast, the center region of the XX histogram shows a significant peak, which is much larger than expected from the excellent laser impurity extinction measured in the Rabi oscillation power series above. This effect is due to the re-excitation of the XX transition in the two-photon resonant excitation scheme. After the emission of an XX photon, the quantum dot is in the exciton state, where there is a probability to be re-excited and hence emit another XX photon leading to bunching, while blocking coincidence events from the X transition. This re-excitation is driven by the spectral tails of the laser pulse, see figure 6.11(a). This re-excitation limits our achievable $g^{(2)}(0)$.

We can simulate the emission from the system by solving the optical Bloch equations for the cascaded three-level system in equation 2.19 numerically. We use the parameters extracted from measurements in the above section for the decay rates γ_X and γ_{XX} , and the laser bandwidth from our calibration measurement of 22 GHz. We simulate the case where the laser frequency is chosen such that the detuning Δ_X is half of Δ_{2X} , where we use $\Delta_{2X} \sim 2$ nm from figure 6.6(b). A preliminary resulting $g^{(2)}(\tau)$ for the two transitions are shown in figure 6.11(b), which clearly exhibit the same dip and peak feature as the recorded data. The absolute scale here is not considered in the solutions and should be fitted to the experimental data to get the correct normalization. However, we observe that there is a fundamental limit on $g^{(2)}(0)$, and their relative height shows that it is more severe for the XX transition, as confirmed by our experimental results.

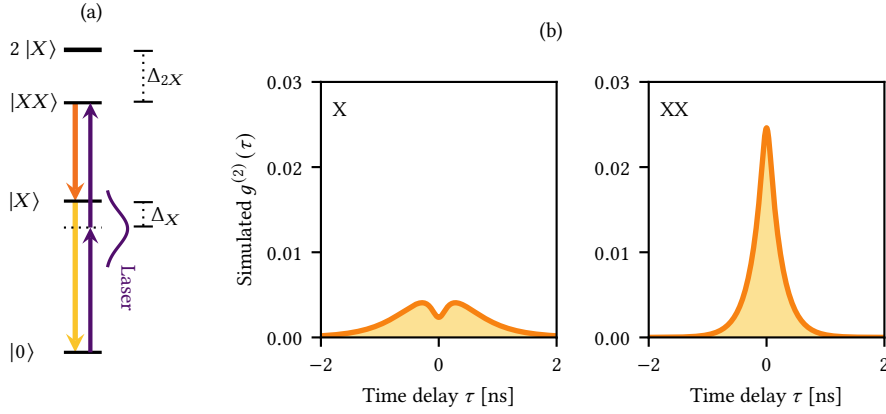


Figure 6.11: Effect of re-excitation on $g^{(2)}(\tau)$. (a) Energy level diagram of the biexciton cascaded system under two-photon resonant excitation. The broad bandwidth Gaussian laser pulse can re-excite an exciton state $|X\rangle$ back into the biexciton state $|XX\rangle$. (b) Numerical solutions to the optical Bloch equations 2.19 for a three-level cascaded system as illustrated in (a). The equations are solved using the parameters $\{\Delta_X, \gamma_X, \gamma_{XX}\}$ where experimentally measured above, using $\Delta_X = \Delta_{2X}$ and $\gamma_{\text{dp}} = 0$.

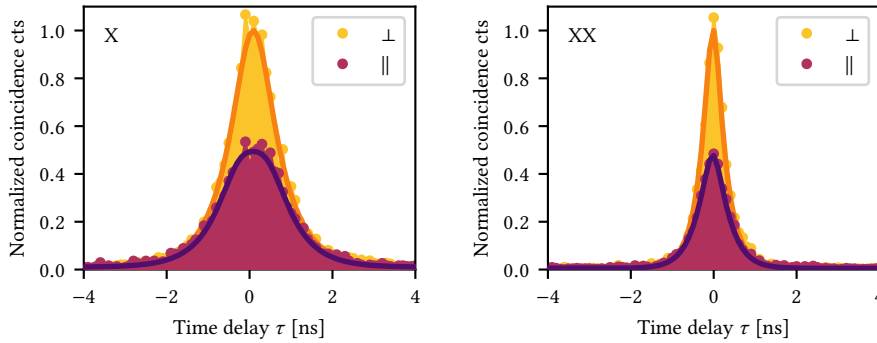


Figure 6.12: Coincidence histograms recorded in a HOM interference experiment on co- and cross-polarized configuration, for photons from the exciton X transition, and the biexciton XX transition.

This differs from the earlier reported values (Schweickert et al., 2018), but this could be due to a different Δ_{2X} , laser bandwidth, or lower excitation power.

We continue our study of the single-photon properties by performing HOM interference experiments for both the X and XX transition. The center peaks in co- and cross-polarization is plotted in figure 6.12 together with fits as described in section 5.7. The measurements were performed using the optimized HOM interferometer setup

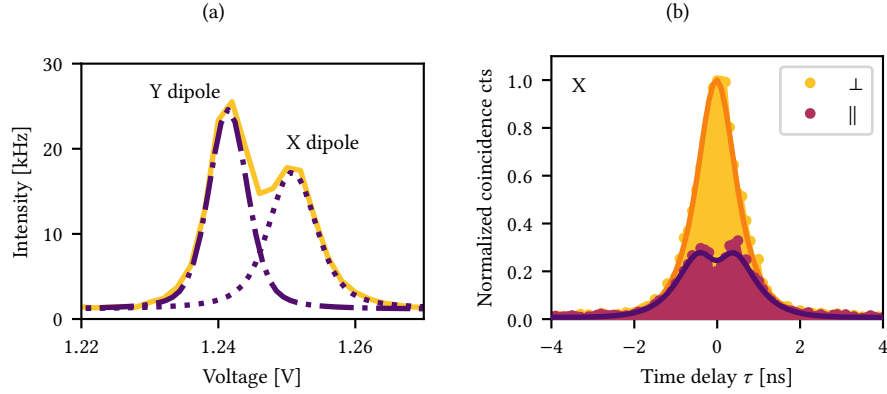


Figure 6.13: (a) Voltage scan of the exciton X transition under two-photon resonant excitation. The emission is filtered with both the grating filter and the etalon filter, enabling the distinction between the Y and X dipoles. The dashed lines is a fit to two Voigt functions. (b) HOM interference experiment performed with both filters and a gate voltage of 1.24 V selecting the Y dipole in (a).

discussed in section 5.7.2 and hence are reliable estimates of the indistinguishability. The interference in co-polarized configuration is very low and we calculate low raw visibilities of $V_{\text{raw}}^X = 35\%$ and $V_{\text{raw}}^{XX} = 37\%$.

As mentioned, we employ the grating filter when using the two-photon excitation scheme, to avoid contributions of the laser and the emission from other quantum dots overlapping with the other transmission windows of the etalon. This means that both of the dipole transitions in the fine structure split exciton state (5 GHz), is collected within the filter window (22 GHz), and cannot be distinguished with polarization as we do in resonant excitation. Therefore we use a combination of both the grating filter and the Etalon filter, which allows distinguishing the two dipoles in a voltage scan, as seen in figure 6.13(a).

The Y dipole can be selected by applying a gate voltage of 1.24 V and another HOM experiment is performed. The result is shown in figure 6.13(b), where we calculate a slightly improved raw visibility of 49%. We emphasize that this measurement was performed on the same quantum dot which shows excellent raw visibility of $> 94\%$ under strict resonant excitation.

We perform a second series of measurements on a different quantum dot. The quantum dot was first carefully characterized in RF using the procedures described in section 5.3, and the resonant HOM visibility for this quantum dot is $> 90\%$. Under two-photon resonant excitation, we observe the similar features in the $g^{(2)}(\tau)$ measurements. We perform HOM interference experiments and the recorded histograms are shown in figure 6.14, which again is limited to $< 50\%$ for both the excitation and biexciton emission. These two separate demonstrations of limited indistinguishability appearing

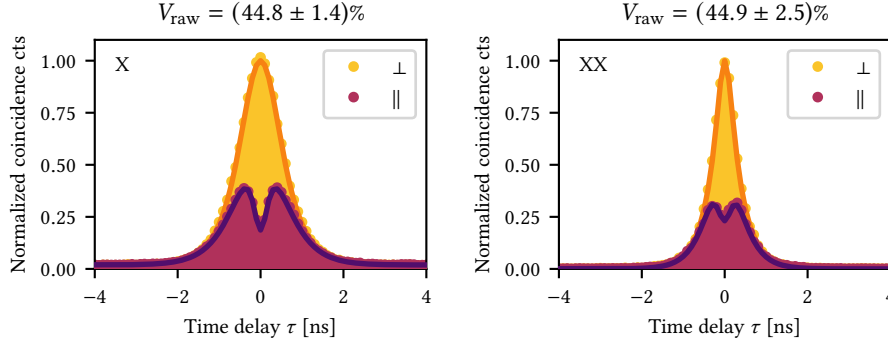


Figure 6.14: Consistency check of indistinguishability measurement on a different quantum dot. Coincidence histograms recorded in a HOM interference experiment on co- and cross-polarized configuration, for photons from the exciton X transition and the biexciton XX transition.

when changing from resonant to two-photon resonant excitation schemes is strong experimental evidence of the limitations of this scheme.

We can understand this limitation of the cascaded decay in the following way. The biexciton transition is limited due to a finite lifetime of its ground state, the exciton. The exciton transition is limited because of timing jitter on the 'loading' time through the biexciton, which we saw in figure 6.8.

Recently in the preprint Schöll et al., 2020 they report similar limited HOM interference under two-photon resonant excitation. They further argue that the fundamental limit for the visibility can be calculated from the trace purity in the case of single-photon emission as

$$V_{\text{lim}} \approx \mathbb{P} = \frac{\gamma_{XX}}{\gamma_{XX} + \gamma_X}, \quad (6.2)$$

which for QD4 is 0.68.

Interestingly this fundamental limit contradicts many previously reported HOM visibilities under two-photon excitation where values from $\sim 70\%$ all the way to 93% has been reported (D. Huber et al., 2017; Liu et al., 2019; Müller et al., 2014; H. Wang, Hu, et al., 2019). All these measurements were performed using only 2 ns time delay as previously discussed in section 5.7.2 extracting the central peak area reliably here is highly dependent on the background subtraction. We note that the highest reported value of 93% in D. Huber et al., 2017 does not use a separate cross-polarized measurement, and instead use a side peak for reference. Therefore, this value could be overestimated. As an outlook, we would like to confirm this limitation in HOM visibility through the optical Bloch equation model of the cascaded system.

The experimentally observed limitation in both the HOM visibility and single-photon purity and conceptual understanding of the limitations imply that single photons from

the cascaded decay are not feasible as a single-photon source. In Schöll et al., 2020 they suggest overcoming the fundamental limit by Purcell enhancing the XX transition, which will increase the limiting value in equation 6.2. This could be achieved in a PCW since the XX transition is spectrally closer to the band-edge than the X transition, and could be a very interesting approach to investigate.

* * *

In this chapter we have investigated two different excitation schemes which can be employed to potentially improve the emission properties from a quantum dot.

Firstly we investigated the influence of changing the laser bandwidth under strict resonant excitation. We observe that an optimal bandwidth exists, where the single-photon purity is minimized as a consequence of simultaneous laser background suppression and suppressed re-excitation. At this optimal point, raw HOM visibilities exceeding 94 % was observed.

In the second part of the chapter, a thorough experimental investigation of the two-photon resonant excitation scheme was carried out. We have seen evidence that the excitation process is less efficient, leading to a lower maximal single-photon emission rate. Secondly, the single-photon purity is limited due to re-excitations, confirmed by numerical solutions. Finally, the indistinguishability of the photons emitted from either of the X and XX transitions is limited due to the cascaded nature of the decay.

CHAPTER


POLARIZATION ENTANGLEMENT FROM THE BIEXCITON CASCADE

The method for tomographic reconstruction of polarization-entangled photons is presented and performed using photons emitted from a quantum dot.

Polarization entanglement generated from the cascaded decay of the biexciton was proposed already in the early days of exploring quantum dots as single-photon sources (Yamamoto et al., 2000). A few years later, polarization-entanglement was experimentally demonstrated (Stevenson et al., 2006) and has since been widely studied for the potential to realize a deterministic source of entangled photons (Dousse et al., 2010; D. Huber et al., 2017; T. Huber et al., 2014; Jöns et al., 2017; Liu et al., 2019; Stevenson et al., 2006).

In this chapter, we perform quantum state tomography on the polarization-entangled photons emitted from the biexciton of a *nanowire quantum dot*. This work was performed during a stay in the Photonics group at University of Innsbruck as the *change of scientific environment* which is a part of the PhD programme at University of Copenhagen. It was a pleasure to visit the group and work in their laboratories together with dedicated people. It led to highly fruitful discussions which inspired other parts of this thesis work.

7.1 RECONSTRUCTION OF A TWO-MODE QUANTUM STATE

We start the chapter off by describing how a density matrix representing a two-mode quantum state, can be reconstructed from a series of experimentally measurable inten-

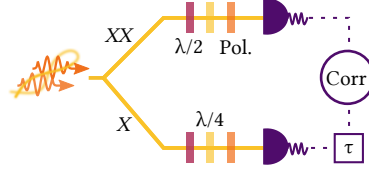


Figure 7.1: Experimental setup employed to perform quantum state tomography of a two-photon polarization-entangled state. The entangled input mode containing two photons from the exciton X and biexciton XX can be separated in frequency using e.g. the filter described in figure 4.4(a).

sity correlations. The density matrix of the entangled state $|\Phi^+\rangle = \frac{1}{\sqrt{2}}(|HH\rangle + e^{i\phi}|VV\rangle)$ emitted from the biexciton cascade as described in section 2.6.2 is

$$\rho_{\text{th}}(\phi) = |\Phi^+\rangle \langle \Phi^+| = \begin{array}{c} \begin{array}{cccc} |HH\rangle & |HV\rangle & |VH\rangle & |VV\rangle \end{array} \\ \left[\begin{array}{cccc} \frac{1}{2} & 0 & 0 & \frac{1}{2}e^{i\phi} \\ 0 & 0 & 0 & 0 \\ 0 & 0 & 0 & 0 \\ \frac{1}{2}e^{-i\phi} & 0 & 0 & \frac{1}{2} \end{array} \right] \begin{array}{l} \langle HH| \\ \langle HV| \\ \langle VH| \\ \langle VV| \end{array} \end{array} \quad (7.1)$$

Using *quantum state tomography*, following the methods presented in James et al., 2001 it is possible to reconstruct the density matrix of an arbitrary two mode quantum state by measuring intensity correlations between the two modes. Figure 7.1 shows the experimental setup employed for the state tomography of polarization-entangled photons. It consists of two sets of polarization optics each consisting of a quarter- and half-waveplate followed by a polarizer. These two sets will be used to perform polarization projections on exciton X photon and biexciton XX photons, respectively, which are the two modes that we study. By rotations of the waveplates, we can project incoming photons to any polarization state.

An incident photon in the $|V\rangle$ polarization is projected by the two waveplate transformation matrices $U_{\text{HWP}}(h)$ and $U_{\text{QWP}}(q)$ at given angles h and q respectively

$$|\Psi^{(1)}(h, q)\rangle = U_{\text{QWP}}(q) \cdot U_{\text{HWP}}(h) |V\rangle = a(h, q) |H\rangle + b(h, q) |V\rangle, \quad (7.2)$$

where,

$$a(h, q) = \frac{1}{\sqrt{2}} \left(\sin(2h) - i \sin(2[h - q]) \right) \quad (7.3)$$

$$b(h, q) = -\frac{1}{\sqrt{2}} \left(\cos(2h) + i \cos(2[h - q]) \right). \quad (7.4)$$

For two photons the projection state with the set of waveplate angles $\{h_1, q_1, h_2, q_2\}$, is given by

$$\begin{aligned} |\Psi_\nu\rangle &= \left(|\Psi^{(1)}(h_{1\nu}, q_{1\nu})\rangle \otimes |\Psi^{(1)}(h_{2\nu}, q_{2\nu})\rangle \right) \\ &= a(h_1, q_1)a(h_2, q_2) |HH\rangle + b(h_1, q_1)b(h_2, q_2) |VV\rangle \\ &\quad + a(h_1, q_1)b(h_2, q_2) |HV\rangle + b(h_1, q_1)a(h_2, q_2) |VH\rangle, \end{aligned} \quad (7.5)$$

here, ν represents a given set of waveplate angles.

The average number of coincidence counts between X and XX photons transmitting through the polarization projection waveplates is generally described by

$$n_\nu = N \langle \Psi_\nu | \rho | \Psi_\nu \rangle, \quad (7.6)$$

where N is a constant dependent on the photon flux and detector efficiencies. We can measure these coincidence counts, which allow to calculate back the density matrix as

$$\rho = \frac{\sum_{\nu=1}^{16} M_\nu n_\nu}{\sum_{\nu=1}^4 n_\nu}, \quad (7.7)$$

where the matrix M_ν represents the polarization basis set. M_ν is calculated from $|\Psi_\nu\rangle$ and 16 independent transformation matrices from the Pauli matrices ($\sigma_i \otimes \sigma_j$). Note that only 16 combinations of polarization are needed to reconstruct ρ since it is a 4×4 matrix. Table 7.1 shows an example of a set of 16 basis states defined by a set of waveplate angles, and the intensity correlation can be measured for each set and used to reconstruct the state.

This is a direct linear reconstruction, mapping the measured data into the corresponding density matrix. This often leads to an unphysical state due to detection noise or errors. The typical method to circumvent this problem is implementing a maximum likelihood method (James et al., 2001). By setting some physical constraints on the final density matrix, we numerically reconstruct the most likely *physical* state given the recorded data.

7.1.1 Maximum Likelihood Estimation

By inferring a maximum likelihood estimation method we can ensure that the final density matrix is physical. We define a matrix T for which $T^\dagger T$ must have the properties of normalization, Hermiticity, and positivity. The matrix T can be written as a tridiagonal matrix to fulfill this, and depends on 16 parameters (t_1, t_2, \dots, t_{16})

$$T(t) = \begin{bmatrix} t_1 & 0 & 0 & 0 \\ t_5 + it_6 & t_2 & 0 & 0 \\ t_{11} + it_{12} & t_7 + it_8 & t_3 & 0 \\ t_{15} + it_{16} & t_{13} + it_{14} & t_9 + it_{10} & t_4 \end{bmatrix}. \quad (7.8)$$

ν	Mode 1	Mode 2	h_1	q_1	h_2	q_2
1	$ H\rangle$	$ H\rangle$	45°	0	45°	0
2	$ H\rangle$	$ V\rangle$	45°	0	0	0
3	$ V\rangle$	$ V\rangle$	0	0	0	0
4	$ V\rangle$	$ H\rangle$	0	0	45°	0
5	$ R\rangle$	$ H\rangle$	22.5°	0	45°	0
6	$ R\rangle$	$ V\rangle$	22.5°	0	0	0
7	$ D\rangle$	$ V\rangle$	22.5°	45°	0	0
8	$ D\rangle$	$ H\rangle$	22.5°	45°	45°	0
9	$ D\rangle$	$ R\rangle$	22.5°	45°	22.5°	0
10	$ D\rangle$	$ D\rangle$	22.5°	45°	22.5°	45°
11	$ R\rangle$	$ D\rangle$	22.5°	0	22.5°	45°
12	$ H\rangle$	$ D\rangle$	45°	0	22.5°	45°
13	$ V\rangle$	$ D\rangle$	0	0	22.5°	45°
14	$ V\rangle$	$ L\rangle$	0	0	22.5°	90°
15	$ H\rangle$	$ L\rangle$	45°	0	22.5°	90°
16	$ R\rangle$	$ L\rangle$	22.5°	0	22.5°	90°

Table 7.1: A selection of 16 basis states and the corresponding wave plate angles needed to make a tomographic reconstruction. Here $|H\rangle$, $|V\rangle$ ect, are the polarization states represented on the Poincaré sphere (see figure 7.3(b)). Table is from James et al., 2001.

The physical density matrix is then given by

$$\rho_{\text{phys}} = \frac{T^\dagger(t)T(t)}{\text{Tr}\{T^\dagger(t)T(t)\}}, \quad (7.9)$$

which is normalized by dividing the density matrix elements by the trace.

It can be quantified how much this state, given a set of the 16 parameters, matches the collected data with a likelihood function

$$L(t_1, t_2, \dots, t_{16}) = \sum_{\nu=1}^{16} \frac{(N \langle \psi_\nu | \rho_{\text{phys}}(t_1, t_2 \dots t_{16}) | \psi_\nu \rangle - n_\nu)^2}{N \langle \psi_\nu | \rho_{\text{phys}}(t_1, t_2 \dots t_{16}) | \psi_\nu \rangle} \quad (7.10)$$

where $N \langle \psi_\nu | \rho_{\text{phys}}(t_1, t_2 \dots t_{16}) | \psi_\nu \rangle = \bar{n}_\nu$ is the expected number of coincidence counts, which is compared to the measured n_ν . By using the standard optimization routine of numerically minimizing the log-likelihood, we can find the parameter set that leads to the most likely physical state given the data. We can then compare to the expected entangled state and extract an entanglement fidelity.

7.2 EXPERIMENTAL REALIZATION OF POLARIZATION ENTANGLEMENT

In this section, we perform quantum state tomography by measuring intensity correlations between the exciton X and biexciton XX photons. The experiment was performed during the *change of scientific environment*, and employs a different type of quantum dot. We begin with a few characterization measurements of this type of quantum dot.

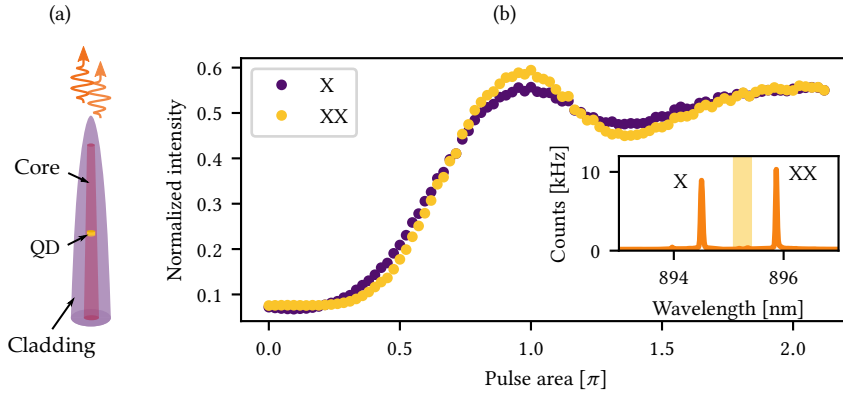


Figure 7.2: (a) Sketch of a nanowire quantum dot, emitting photons from the tapered tip. This design leads to 50% of the photons emitting into the substrate. This loss can be overcome by implementing a DBR at the base of the nanowire to reflect the photons back. (b) Rabi oscillations observed for the exciton X and biexciton XX under two-photon resonant excitation. The inset shows the spectrally resolved emission where the X and XX lines are marked. The laser is fully suppressed by placing two narrow-band notch filters in the region shaded in yellow.

7.2.1 Quantum Dot Characterization

The type of quantum dots used by the Photonics group in Innsbruck to generate biexciton polarization entanglement is *nanowire quantum dots* (T. Huber et al., 2014). A thorough description and characterization is outside the scope of this thesis, but a short introduction and a few characterization measurements will be presented. The setup used for the characterization is similar to the one presented in chapter 4.

In section 3.1 we described the growth process of nanowire quantum dots, leading to out of plane emission along the nanowire as illustrated in figure 7.2(a). As mentioned earlier, the radial symmetry of the nanowire leads to a smaller fine structure splitting, which for the specific quantum dot employed here was measured to be ~ 2.4 GHz. The symmetry of the nanowire design means that there is no polarization-dependent coupling of the emitted photons, and should ideally collect the photons with equal efficiency regardless of their polarization.

The biexciton is excited with two-photon resonant excitation, using a stretched laser pulse as described in section 6.2. A spectrum recorded under two-photon excitation is displayed in the inset of figure 7.2(b). Note that two narrow-band (< 0.6 nm) *notch filters* are placed in the yellow shaded region, to suppress the laser background. This is necessary for spectroscopy in the nanowire, where we excite and collect in the same spatial mode. By increasing the power of the excitation laser we observe Rabi oscillations of both the X and XX transitions. A substantial amount of dephasing is present seen by the heavy damping of the oscillations, already before reaching π -pulse excitation, which could be limited by surface charges on the nanowire.

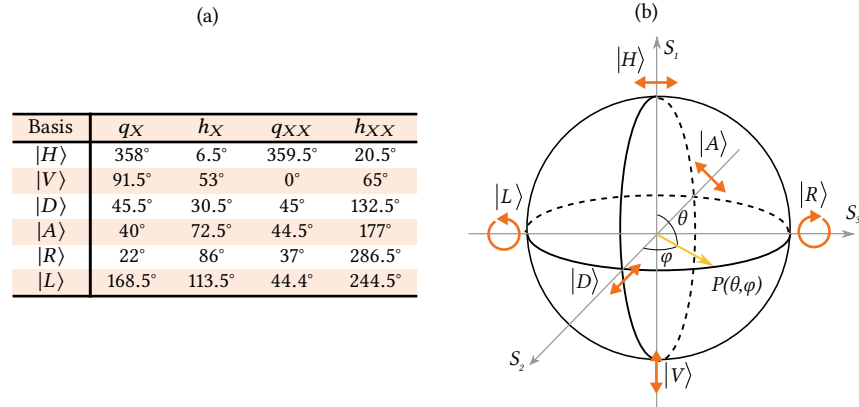


Figure 7.3: (a) Calibrated waveplate angles measured for the two sets of tomography waveplates. The calibration is done using a polarimeter to determine the resulting basis state. (b) Poincaré sphere illustrating the possible basis states. Any polarization state is represented by the vector $P(\theta, \phi)$.

Finally, the lifetime of both the exciton and the biexciton was measured and fitted to an exponential decay as described in 5.4 yielding decay rates of $\gamma_X = 0.57 \text{ ns}^{-1}$ and $\gamma_{XX} = 1.6 \text{ ns}^{-1}$. Again the biexciton decays approximately twice as fast due to the two decay channels.

7.2.2 Calibration of the Tomography Setup

The reconstruction of the matrix relies on knowing exactly in which basis set a given measurement was performed. The waveplates are mounted in manual rotation mounts. We characterize each set of waveplates using a polarimeter, where the angle settings leading to a given polarization state can be identified. The polarimeter can measure the polarization state of an optical beam with azimuth and ellipticity accuracies of $\pm 0.025^\circ$ on the Poincaré sphere displayed in 7.3(b). We use a cw laser source for the characterization, and first, the polarizer is placed in the beam, and aligned with $|H\rangle$ polarization. After the polarizer, we place the waveplates in reverse order compared to the tomography setup seen in figure 7.1, to map out the transformation from $|H\rangle$ to some other given polarization. The waveplates are rotated until the desired basis state is reached at the polarimeter, and the angle settings are noted down. This is repeated for each basis state and all angle settings are listed in the table of figure 7.3(a). Note that all combinations of these bases leads to 36 possibilities, and for a tomography measurement a subset of 16 combinations are chosen as the example in table 7.1.

7.2.3 Cross-correlation Measurements

Cross-correlation measurements between the X photon and the XX photon are performed for 16 combinations of polarization bases defined by the waveplate angles

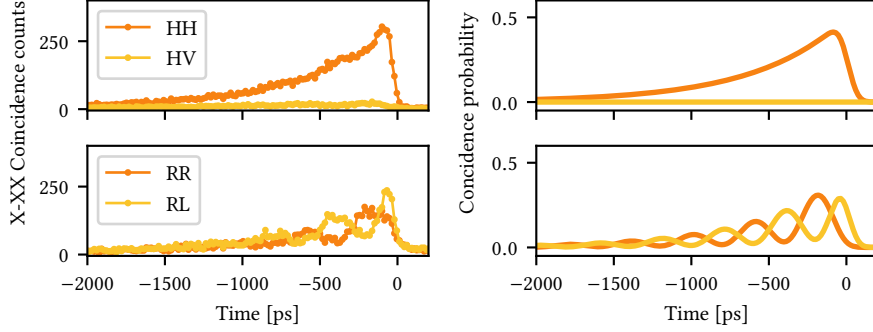


Figure 7.4: The first two panels are the cross-correlation histograms between the exciton X and biexciton XX transition measured for different waveplate settings defining polarization projections according to the table in figure 7.3(a). The second two panels are the calculated coincidence probability from equation 7.12 with the same polarization projections.

in figure 7.3(a). The cross-correlation histograms recorded in some of the basis sets are displayed in figure 7.4. The cascaded decay leads to an asymmetric shape of the coincidence histograms, which is most apparent in the co-polarized linear basis $|HH\rangle$. The cascade dictates that the XX is always emitted before the X photon, therefore no X -to- XX coincidence events exist after time bin 0. From figure 2.12(a) we see $|HH\rangle$ corresponds to a single branch of the cascade, and therefore see a bunching in the coincidence events. On the other hand, projecting the two photons onto different branches as in $|HV\rangle$ we detect almost no coincidence counts.

If we instead project onto circular polarization bases $|R\rangle$ and $|L\rangle$ we observe a different behavior in the coincidences. The biexciton decay expressed in the circular basis exhibits a time-dependent spin-flip of the exciton state due to the fine structure splitting as explained in figure 2.12(b). This leads to oscillations in the coincidence histogram. We take a closer look at the dynamics for the $|RL\rangle$ histogram; Initially at $t \approx 0$ there is maximal counts since this corresponds to photons that follow a single branch in the circular basis. Shifted by one oscillation period, we observe minimal counts. This corresponds to a time where the exciton has experienced a spin flip such that the second photon in the cascade X is emitted with the polarization given by the opposite branch. Equivalently, the oscillations of $|RR\rangle$ are shifted by π .

The projection dependent coincidence histograms can be described with a simple theoretical model (Winik et al., 2017). An arbitrary polarization of a photon can be represented on the Poincaré sphere $P(\theta, \phi)$ as in figure 7.3(b) and is given by

$$P(\theta, \phi) = \cos(\theta/2) |H\rangle + e^{i\phi} \sin(\theta/2) |V\rangle. \quad (7.11)$$

The coincidence probability to detect the first biexciton photon with polarization P_{XX} and after a time t detect the second cascaded exciton photon P_X is

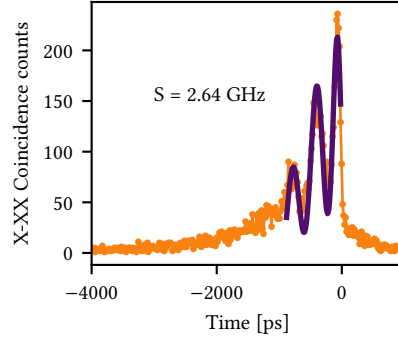


Figure 7.5: Cross-correlation histogram in the RL projection basis. The purple solid line is a fit to equation 7.12 convolved with a Gaussian instrument response function. From the fit the fine structure splitting S is extracted and displayed on the figure.

$$\begin{aligned}
 & p\left(t, P_X(\theta_X, \phi_X), P_{XX}(\theta_{XX}, \phi_{XX})\right) \\
 &= \frac{e^{-t/\tau_X}}{2\tau_X} \left| \langle P_X(\theta_X, \phi_X) P_{XX}(\theta_{XX}, \phi_{XX}) | \Psi(t) \rangle \right|^2 \\
 &= \frac{e^{-t/\tau_X}}{2\tau_X} \left| \cos\left(\frac{\theta_X - \theta_{XX}}{2}\right) \cos\left(\frac{\phi_X + \phi_{XX}}{2} + \pi t S\right) \right. \\
 &\quad \left. + i \cos\left(\frac{\theta_X + \theta_{XX}}{2}\right) \sin\left(\frac{\phi_X + \phi_{XX}}{2} + \pi t S\right) \right|^2. \tag{7.12}
 \end{aligned}$$

In the right panels of figure 7.4 the theoretical coincidence probability of the displayed measured polarization states is shown. The model is convolved with a Gaussian function to simulate the instrument response function and uses the measured values of τ_X and S . The theoretical model is in very good agreement with the measured histograms.

Furthermore, this model can be used as a method for fitting the fine structure splitting, as shown in figure 7.5.

For a robust fit, a reference measurement of the IRF should be included, but this was unfortunately not available for the used detectors. The returned fine structure splitting of 2.71 GHz is in good agreement with the previously stated value of 2.5 GHz, which is measured with a method that has the tendency to slightly underestimate the value (T. Huber et al., 2014).

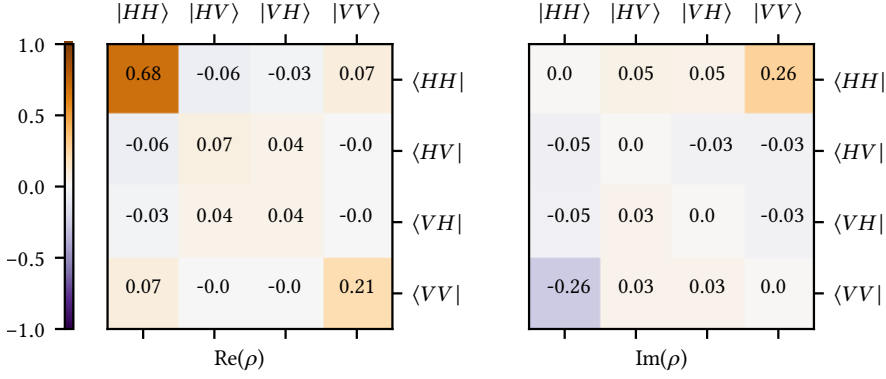


Figure 7.6: Reconstructed density matrix using maximum likelihood estimation. The matrix is reconstructed from the first time bin of cross-correlation histograms in 16 different polarization bases.

7.2.4 Density Matrix Reconstruction

To circumvent the time-dependent evolution of the cross-correlations as observed in figure 7.4 we post-select the first time bin of the histograms for the reconstruction of the density matrix. Using the maximum likelihood method introduced in section 7.1, the resulting density matrix is plotted in figure 7.6, with the real and imaginary part in the two panels.

We notice a dramatic difference in the $|HH\rangle\langle HH|$ component than the $|VV\rangle\langle VV|$, which in theory should be equal (see equation 7.1). This imbalance can be attributed to a possible asymmetry in the nanowire shape leading to a polarization-dependent outcoupling efficiency (Bulgarini et al., 2014).

The significant imaginary components of $|HH\rangle\langle VV|$ and $|VV\rangle\langle HH|$, suggest an initial phase of $|\Phi^+(\phi = \pi/2)\rangle = \frac{1}{\sqrt{2}}(|HH\rangle + i|VV\rangle)$. This initial phase rotation could arise from the coupling to the nanowire waveguide mode and is consistent with previously reported measurements in the setup. We compare how much the reconstructed state overlaps with this state by the fidelity

$$F = \langle \Phi^+(\phi = \pi/2) | \rho_{\text{meas}} | \Phi^+(\phi = \pi/2) \rangle = 0.71, \quad (7.13)$$

which shows good agreement with the state. This is consistent with previously measured fidelities in this experiment (T. Huber et al., 2014). In Jöns et al., 2017 they demonstrate an improved fidelity of 0.81 which they explain by employing a quasi resonant excitation scheme to avoid re-excitations. However, much higher fidelities have been demonstrated in e.g. D. Huber et al., 2017 and H. Wang, Hu, et al., 2019 using the two-photon resonant excitation scheme. Here a different type of quantum dot and nanophotonic structure was employed. Achieving high fidelity of the polarization

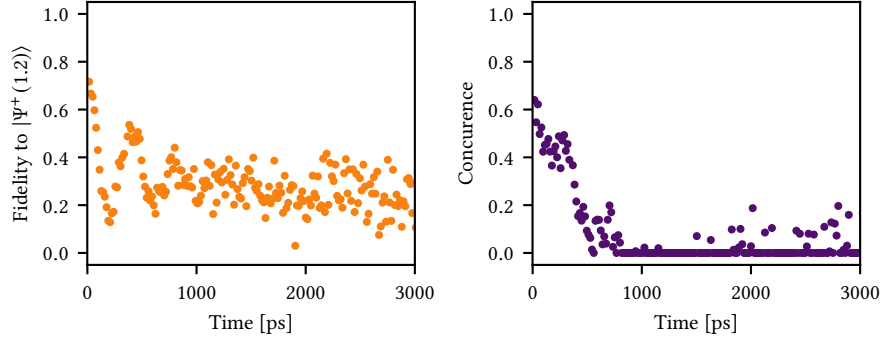


Figure 7.7: Entanglement fidelity and concurrence calculated for a reconstructed density matrix like in figure 7.6 for each time bin of the 16 coincidence histograms. The fidelity oscillates with fine structure splitting, while the concurrence does not depend on this.

entangled state relies on efficient preservation of the emitted photon state, and the limited values achieved in nanowires could stem from imperfection in the preservation of polarization in the nanowire.

Using the phase as a free parameter, by maximizing the fidelity, we can estimate the initial state of the two-photon entangled state $|\Phi^+(\phi = 1.2)\rangle = \frac{1}{\sqrt{2}}(|HH\rangle + e^{i1.2}|VV\rangle)$, leading to a slightly improved fidelity of $F = 0.72$.

We calculate the fidelity compared to $|\Phi^+(\phi = 1.2)\rangle$ of a reconstructed density matrix for each time bin of the 16 correlation histograms. This reveals clear oscillations as the emitted state rotates into and out of phase with the $|\Phi^+(\phi = 1.2)\rangle$ state as seen in figure 7.7. The oscillations are heavily dampened where we observe that after around two periods of oscillations the fidelity drops to $F < 0.5$. The fidelity is highly dependent on the choice of comparison state, meaning that we would reach maximal fidelity at the current minimum, if we compare to $|\Phi^+(\phi = 1.2 \pm \pi)\rangle$ instead.

A more robust and generalized quantity expressing the entanglement quality is the concurrence

$$C = \max(0, \lambda_1 - \lambda_2 - \lambda_3 - \lambda_4) = 0.64, \quad (7.14)$$

also calculated for the first time bin. λ_n is the n 'th eigenvalue of the reconstructed density matrix. The concurrence is dependent only on the matrix itself and can thus be compared across physical systems. A quantum state has some degree of entanglement if $C > 0$, while for a fully pure and non-separable entangled state $C = 1$.

The concurrence is calculated for each time bin and is plotted in figure 7.7. As expected, no oscillations are present in the concurrence but it shows a dramatic drop already within a few time bins. For times > 750 ps most of the reconstructed matrices correspond to states that are fully separable, with no entanglement. This could be connected with the strong decoherence observed in the Rabi oscillations.

Ideally, integrating the correlation histograms over the whole photon packet in time is preferred, both in terms of efficiency and simplicity. Doing this results in a reconstructed matrix with $F = 0.3$ and $C = 0$, meaning that there is no entanglement. Recently, in a preprint a high concurrence of ~ 0.90 is reported which stays > 0.5 across the whole photon wave packet (Zeuner et al., 2019). For our highly coherent charge-controlled self-assembled InAs quantum dots we expect similar high concurrence.

* * *

In this chapter we have explained and shown how to measure polarization entanglement, using quantum state tomography. The entanglement was generated from the biexciton cascade in a nanowire quantum dot, and measured using 16 cross-correlation measurements. A density matrix representing the entangled state was reconstructed using a maximum likelihood method. Both the entanglement fidelity and concurrence was calculated for each time bin of the correlation histograms, both proving entanglement of the source. However, this is very dependent on post-selecting the short time scale time bin.

We have seen how the fine structure splitting induces a time evolution of the entangled state, evident in the time dependent entanglement fidelity. In Fognini et al., 2018 they propose to experimentally 'erase' this oscillation by fast switching of the measurement basis polarization. This appealing idea needs extremely fast switching and is proposed to be implemented using an EOM (electro-optic modulator). This remains to be demonstrated experimentally and might not be feasible in practice. Another approach to circumvent the oscillations is to reduce the fine structure splitting using low strain droplet etched quantum dots (D. Huber et al., 2017; H. Wang, Hu, et al., 2019).

CHIRAL COUPLING OF THE BIEXCITON CASCADE

The polarization entanglement generated from the biexciton cascade can be preserved and converted to path-encoding by chiral coupling in a planar nanophotonic structure.

The cascaded decay from the biexciton provides a source of polarization-entangled photons as presented in chapter 7. High-efficiency entangled photon generation is a key requirement in the quantum information protocols as discussed in chapter 1. The integration in a planar nanophotonic structure with high coupling efficiency could be a promising approach to achieve this. However, as soon as a photon couples to a planar waveguide mode, the polarization information is lost since the waveguide only supports a single mode. Coupling the photons of a polarization-entangled state to a single-mode waveguide results in a loss of the polarization information and hence the entanglement. This can be remedied by transferring the polarization-entanglement into another degree of freedom. In general, information encoded in the polarization basis could undergo arbitrary rotations while transmitting over long distances using optical fibers. More robust bases are frequency, time bin, or spatial encoding (Gisin et al., 2002).

The polarization entanglement can be efficiently converted to path entanglement by polarization-dependent directional coupling in a planar nanostructure. This can be achieved by crossing two orthogonal nanobeam waveguides (Luxmoore et al., 2013) or in the chiral points in a standard PCW (Young et al., 2015). However, deterministic photon coupling is not possible in a nanobeam waveguide, and in a PCW chiral points do not overlap with the regions that have near unity coupling i.e. $\beta \rightarrow 1$ (Söllner et al.,

2015). To overcome this limitation, a photonic crystal with glide-plane symmetry as introduced in section 3.2.2 can be employed instead. In a glide plane waveguide (GPW) the overlap between the chiral points and high β regions is maximized and hence is ideal for efficient conversion of the polarization entanglement. In this chapter, we demonstrate successful conversion from polarization basis to path basis of photons emitted from the biexciton cascade.

8.1 CHIRAL NANOSTRUCTURE FOR ENTANGLEMENT PRESERVATION

Efficient preservation of the entanglement in a planar nanophotonic structure can be achieved by directional coupling in a chiral point of a GPW. In this section, we are going to investigate how the polarization-entangled photons from the biexciton cascade couple to the waveguide when the quantum dot is located at the chiral point. Furthermore, we detail how chiral coupling can be demonstrated by studying the time dynamics of the cross-correlation between the exciton and biexciton photons.

8.1.1 Polarization to Path Conversion

The key property is high directional coupling efficiency to the two oppositely propagating waveguide modes. This is enabled by breaking the spatial symmetry, which opens up in-plane circular polarization near the center of the waveguide that overlaps with the high β region. The two circular polarization states $|R\rangle$ and $|L\rangle$ propagate in opposite directions, due to their opposite helicity. Directional coupling of emission from a quantum dot is dependent on its spatial location in the GPW. Emission from a dipole located at the position \bar{r}_0 with the dipole moment $\mathbf{d}(\bar{r}_0)$ couples to the local electric field of the waveguide $\mathbf{E}(\bar{r}_0)$. The coupling is described by the matrix element $|\mathbf{E}(\bar{r}_0) \cdot \mathbf{d}(\bar{r}_0)|^2$. The electric field propagating in the forward direction is given by $\mathbf{E}(\bar{r}_0) = E_0(\hat{\mathbf{e}}_x + e^{i\phi}\hat{\mathbf{e}}_y)$ while the backward direction $\mathbf{E}(\bar{r}_0) = E_0(\hat{\mathbf{e}}_x + e^{-i\phi}\hat{\mathbf{e}}_y)$ where E_0 is the normalization. In a perfect chiral point the phase is $\phi = \pi/2$. For circular dipoles we have $\mathbf{d}_{\pm}(\bar{r}_0) = d_0(\hat{\mathbf{e}}_x \pm i\hat{\mathbf{e}}_y)$, where d_0 is the magnitude of the dipole moment. If circular dipoles are located in a perfect chiral point, the coupling matrix element is maximal for photons emitted with opposite helicity.

Figure 8.1 illustrates how this is used for polarization to path conversion of the entangled state. We consider the biexciton decay in the circular basis as shown in figure 8.1(a), which at $t = 0$ leads to the entangled state

$$|\Psi(t = 0)\rangle = \frac{1}{\sqrt{2}}(|R_{XX}L_X\rangle + |L_{XX}R_X\rangle). \quad (8.1)$$

For a quantum dot located in a perfectly chiral point, all right-hand circular polarized photons couple to the mode propagating in one direction. This means that all R photons are transported to the same outcoupling grating which we could call A , as illustrated in figure 8.1(b). In the same way, all L photons end up at grating B . In this way polarization encoding of the photons is converted to path (or 'which grating outcoupler') encoding.

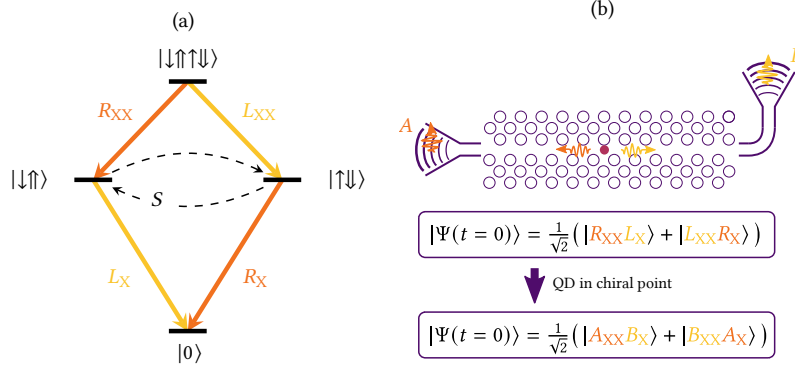


Figure 8.1: Polarization to path conversion of biexciton entanglement. (a) 4-level energy diagram of the biexciton cascade represented in the circular basis. Here there is an oscillation between the two degenerate exciton states at a rate defined by the fine structure splitting S . (b) Glide plane waveguide, which converts polarization-entangled photons to be path-entangled between grating couplers A and B , if the quantum dot is located in a chiral point. The boxes illustrate the conversion of the entangled state.

The same basis change argument applies when considering superposition states, where a superposition of polarization is converted into a superposition of paths, going to grating A and B . The conversion of the full polarization-entangled state is illustrated with the boxed equations in figure 8.1(b). Colors are kept for conceptually keeping track of the original polarization, but that information is lost when the photons couple to the TE-polarized mode of the waveguide. Depending on the sign of the directionality in a given point in the GPW, R photons couple to either outcoupler A or B .

8.1.2 Path-Dependent Cross-Correlations

We are now going to investigate the cross-correlation dynamics between the exciton and biexciton photon, dependent on which path they couple to. The coupling probability for the cascaded photons is given by the matrix element $|\langle P_X P_{XX} | \Psi(t) \rangle|^2$, where P_X and P_{XX} is the polarization projection of the local electric field in the waveguide for the X and XX photons respectively, and $|\Psi(t)\rangle$ is the polarization state of the two entangled photons. This matrix element is exactly the one studied in the model for the cross-correlations in polarization tomography in equation 7.12. The coupling of a certain polarization into the waveguide mode is essentially the same as projecting the photon onto a polarization basis within the waveguide. Therefore, by collecting and measuring the coincidence probability between the exciton photon on one grating, say A_X , and the biexciton photons on B_{XX} , it corresponds to a tomography measurement projecting on the $|P_X = L_X, P_{XX} = R_{XX}\rangle$ basis. Similarly, the measurement of exciton and biexciton photons collected at the same grating, e.g. A_X and A_{XX} corresponds to projecting on $|L_X, L_{XX}\rangle$ or $|R_X, R_{XX}\rangle$. In circular polarization, the model for the coincidence probability reduces to

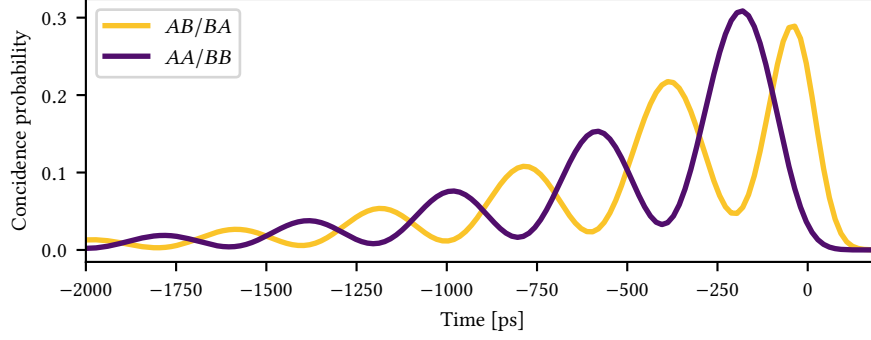


Figure 8.2: Coincidence probability from equation 8.2, using parameters from figure 7.4. For AA (ϕ_X, ϕ_{XX}) = $(\frac{3\pi}{2}, \frac{3\pi}{2})$ where for AB (ϕ_X, ϕ_{XX}) = $(\frac{3\pi}{2}, \frac{\pi}{2})$.

$$p\left(t, P_X\left(\frac{\pi}{2}, \phi_X\right), P_{XX}\left(\frac{\pi}{2}, \phi_{XX}\right)\right) = \frac{e^{-t/\tau}}{2\tau} \left| \cos\left(\frac{\phi_X + \phi_{XX}}{2} + \pi t S\right) \right|^2, \quad (8.2)$$

where,

$$\begin{aligned} |R\rangle &= P\left(\frac{\pi}{2}, \phi = \frac{3\pi}{2}\right) \\ |L\rangle &= P\left(\frac{\pi}{2}, \phi = \frac{\pi}{2}\right) \end{aligned} \quad (8.3)$$

(see Poincare sphere in figure 7.3(b)). The coincidence probability that we expect to see in the two cases of collecting the X and XX photon on opposite gratings AB/BA (either AB or BA) or on the same grating AA/BB is plotted in figure 8.2. Conceptually these oscillations are caused by the time-dependent spin flip of the exciton induced by the fine structure splitting S . This leads to oscillations between the entangled states $|\Psi\rangle = 1/\sqrt{2}(|R_{XX}L_X\rangle + |L_{XX}R_X\rangle)$ and $|\Phi\rangle = 1/\sqrt{2}(|R_{XX}R_X\rangle + |L_{XX}L_X\rangle)$.

The phase of the projections of local electric field polarization for the exciton and biexciton coupling to modes propagating in opposite directions will satisfy $\phi_X = -\phi_{XX}$ while for the same direction we have $\phi_X = \phi_{XX}$. This leads to an oscillation phase of

$$\begin{aligned} AB/BA : \quad \phi_X + \phi_{XX} &= 0 \\ AA/BB : \quad \phi_X + \phi_{XX} &= \pi, \end{aligned} \quad (8.4)$$

for perfect directional coupling of circular polarization phases from equation 8.3. This is exactly the π phase shift of the oscillations seen in figure 8.2.

A phase offset between the oscillations in the two histograms is only present if the emission couples chirally. If the quantum dot is located in a non-chiral point, but still in a location that equally couples the two dipoles, for example diagonal polarization point, the phase in the two configurations AB and AA is identical. Therefore, there is no phase shift between the two cross-correlation plots. In this way, performing such a measurement is evidencing chiral coupling and conversion of entanglement from polarization to path basis.

8.2 EXPERIMENTAL EVIDENCE OF CHIRALLY COUPLED BIEXCITON

In this section, we discuss the measurement described above to demonstrate chiral coupling of the biexciton decay, and thereby realizing conversion of entanglement from polarization to path.

The oscillation period of the correlations is determined by the fine structure splitting. The average fine structure splitting of the exciton is ~ 6 GHz for the self-assembled InAs quantum dots employed in the previous chapters, which corresponds to an oscillation period of < 200 ps. The quantum dot that we discuss in this section is from a different wafer and has a $S \sim 14$ GHz corresponding to ~ 70 ps and an exciton lifetime of only $\tau_X \sim 200$ ps. Resolving the oscillations therefore requires very high timing resolution of the detectors. We employ fast SNSPDs with timing jitter < 20 ps for these measurements.

8.2.1 Sample Characterization

The sample containing GPW employed for these measurements was first characterized. We now briefly present these characterization measurements before studying the directionality.

Figure 8.3(a) displays an SEM image of a GPW structure on the sample used for the measurements. We characterize the photonic properties of the GPW by recording the transmitted signal collected in grating coupler A of a cw laser coupled through the waveguide on grating coupler B . By scanning the wavelength of the laser we record the transmission scan displayed in figure 8.3(b). The transmission scan shows a bandgap region of ~ 10 nm from the two supported modes in the GPW.

The exciton resonance wavelength needs to be at least 3 nm away from the band-edge, in order to keep the biexciton out of the bandgap region. A quantum dot with suitable spectral properties was identified, whereafter it is excited with two-photon resonant excitation. The exciton and biexciton emission lines are identified by recording the charge plateau map seen in figure 8.4(a). Note that the gate voltage applied to populate the neutral exciton for this sample is different as we performed this measurement on another sample with a slightly different diode heterostructure. The emission from the two transitions is filtered separately using a grating filter. Upon varying the excitation power, we observe clear Rabi oscillations of both the exciton as well as the biexciton emission as seen in figure 8.4(b). The intensity plotted here is the raw counts

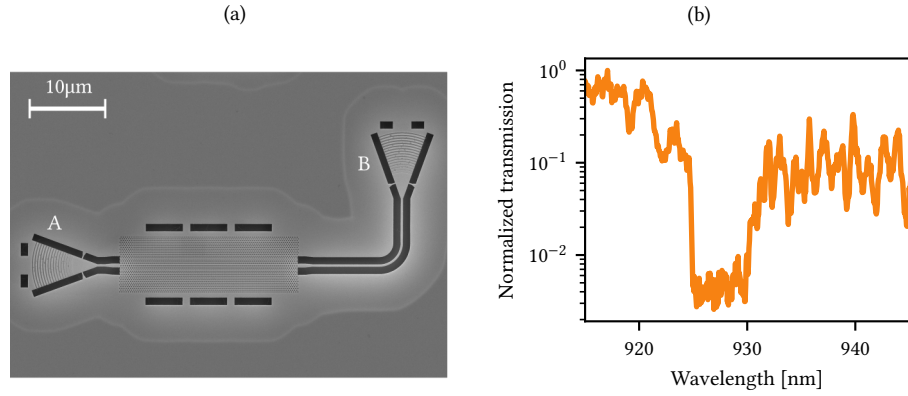


Figure 8.3: Transmission characterization of GPW device. (a) SEM image of a GPW on the sample. (b) Wavelength-dependent transmission through the specific GPW device used for the measurements in figures 8.4 and 8.6.

measured on the SNSPDs, without accounting for any inefficiencies⁽¹⁾. The measured intensity of the exciton emission is about a factor two lower than the biexciton, which is a consequence of the inefficiency of the grating filter employed for filtering the exciton⁽²⁾.

Lifetime measurements performed using the fast detectors together with the exponential fits are shown in figure 8.5. We extract the exciton and biexciton lifetimes to be $\tau_X = 205$ ps and $\tau_{XX} = 102$ ps, respectively.

8.2.2 Chiral Coupling of the Biexciton Cascade

With the quantum dot characterized, we are now ready to perform the two sets of X - XX cross-correlation measurements. For the first set of measurements, we need both collection ports of the experimental setup introduced in section 4.1.2. The two ports are orthogonally polarized and separated on a PBS, and allow us to collect from output gratings A and B simultaneously. Each output is sent through an independent grating filter, with one tuned to the X transition and the other to the XX transition. The filtered signals are sent to the fast SNSPDs and a cross-correlation histogram is recorded at π -pulse excitation. The resulting histogram is plotted with the label AB in figure 8.6. For the second measurement using the same grating, the signal from outcoupler A is split using a fiber beam splitter and X and XX are sent through the two grating filters. The X - XX cross-correlation histogram of the filtered emission is

(1) Due to a wrong thickness of a layer during growth the efficiency of the shallow etched gratings on this sample is low, leading to very low count rates in figure 8.4(b)

(2) Efficiency of the grating filter employed for filtering exciton has an efficiency of $\sim 30\%$ against the $\sim 60\%$ of the one used for filtering the biexciton emission.

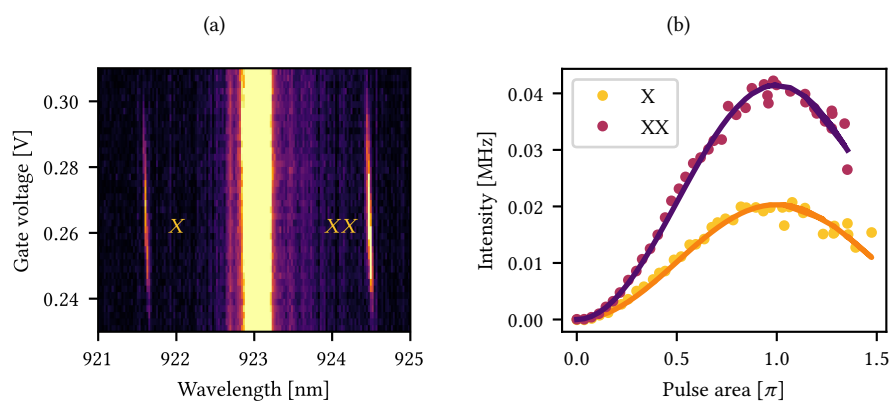


Figure 8.4: Quantum dot characterization (a) Voltage plateau under two-photon excitation, where the exciton X and the biexciton XX are identified. (b) Emission intensity of the exciton and biexciton transitions at gate voltage 0.252 V with varying power exhibit Rabi oscillations. The displayed data is counts with no efficiency corrections. Solid lines are fits to a squared sine.

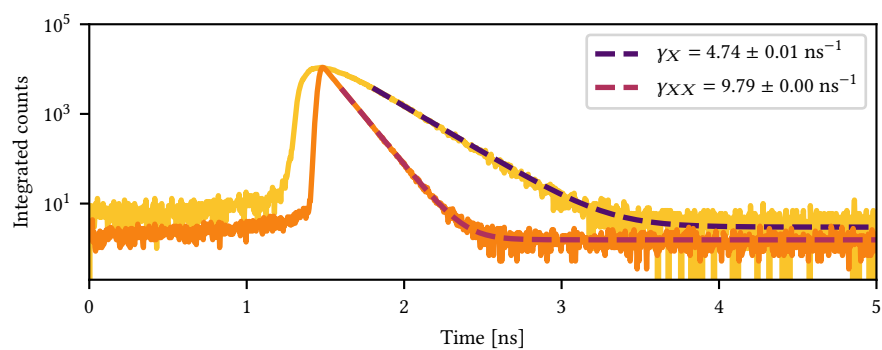


Figure 8.5: Time-resolved measurement of the exciton X and biexciton XX emission. The data are fitted to exponential decays and the extracted lifetimes are shown in the legend.

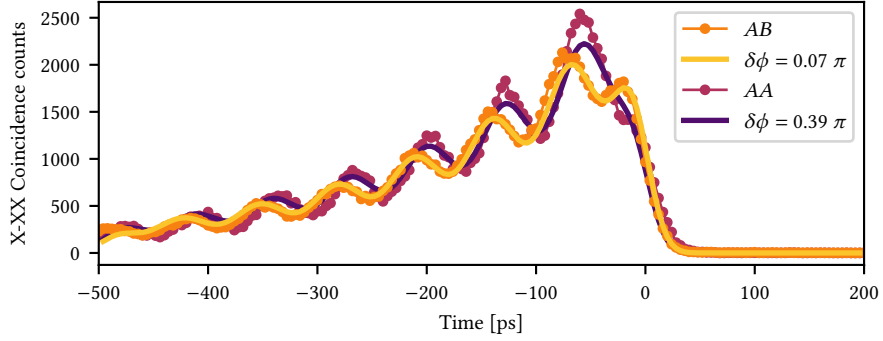


Figure 8.6: Cross-correlation measurements between X and XX in two configurations, shown with dots connected by a line. The AB configuration corresponds to collecting photons on both the gratings (see figure 8.1(b)). The AA configuration is both photons collected on the same grating. The time axis of the two data sets is matched using pulses up to 1 ms (see main text). Solid lines are fits to equation 7.12 convolved with a Gaussian.

recorded, which is shown with the label AA in figure 8.6. We clearly see a phase shift between the two curves.

Robust determination of the relative time axis between the two data sets is crucial, to estimate the phase difference correctly. Due to a different optical path length for collected photons in the two data sets, the arrival time has a small offset. Using the side peaks of the cross-correlation histograms, the two data traces are matched in time with a precision of at least 4 ps over a 1 ms time window. This high precision temporal alignment enables us to reliably estimate small phase shifts of $\sim 0.1\pi$ (for a time period ~ 70 ps) even with the rapid oscillations observed in the quantum dot.

The two data series are fitted to the full model in equation 7.12 to also allow projections that are not on circular polarization. The model leads to multiple degenerate solutions for different sets of $\{\theta_X\theta_{XX}, \phi_X\phi_{XX}\}$ parameters, and therefore we make some constraints to the fit. Since we are only interested in the absolute phase shift in ϕ between the two data series, we fit to the sum as a single parameter $\delta\phi = \phi_X + \phi_{XX}$. We further constrain the fit by setting $\theta_X = \theta_{XX}$ and fix it to be identical for the two curves. The resulting fits are shown with solid lines in figure 8.6, where the fine structure splitting is $S = 14.1$ GHz. The fitted phase for the two data sets is shown in the legend. These phases can be compared to the expected values in equation 8.4 for a perfectly chiral point. In the case of non-directional coupling the two curves will exhibit oscillations that are in phase, and therefore any offset between the two fitted phases is evidence partial chiral coupling. In this way we demonstrate that polarization to path conversion of the biexciton cascade is possible. The fitted phases in the opposite grating configuration gives us directly information of the local projected phase of the emitted photon. Therefore we can estimate the directionality as defined in section 3.2.2

in this point of the GPW

$$D = |\langle L|P(\theta, \phi)\rangle|^2 - |\langle R|P(\theta, \phi)\rangle|^2 = \pm 0.43. \quad (8.5)$$

We have carried out this experiment for two additional quantum dots. The phase shift between the two recorded histograms was 0.26π and 0.18π , for those two dots and hence also exhibits partial directionality. This highlights the spatial dependence of directionality for different quantum dots. By deterministic positioning of a quantum dot in a perfectly chiral point, full conversion from polarization to path is possible (He et al., 2017; Ollivier et al., 2020; Pregolato et al., 2020).

8.2.3 Towards Entanglement Tomography

To fully prove that the entanglement is preserved under the conversion to path a full quantum state tomography is needed. Performing tomography in the spatial basis is a more cumbersome task since this requires stabilizing two interferometers (Solntsev & Sukhorukov, 2017). Tomography in the polarization basis is straightforward as we have seen, therefore one solution is to convert back from path to polarization to estimate the entanglement fidelity. This can be carried out on-chip using *polarization diversity gratings*, known from silicon photonics (Roelkens et al., 2010; J. Wang et al., 2016). These gratings work as an on-chip polarization beam splitters that combines the two spatial modes into a single diffracted optical mode with orthogonal polarizations. Work on implementing polarization diversity gratings on our suspended GaAs platform is already in progress in the group.

* * *

In this chapter, we have seen how a cross-correlation measurement of the biexciton cascade is evidence for chiral coupling. We have demonstrated polarization to path conversion of the biexciton cascade, by chiral coupling of the decay to counter-propagating modes in a GPW. This was observed by a clear phase shift between two cross-correlation histograms recorded for different path configurations. This conversion is a clear pathway for an efficient path-entangled photon source directly on-chip.

Determining the phase shift relies on resolving the fine structure induced oscillations in the correlation histograms. Future work would certainly include repeating the measurement on a quantum dot with smaller fine structure splitting. This means vanishing time averaging when employing the fast SNSPDs, and a high presumed entanglement concurrence across the whole photon temporal package as observed in the preprint Zeuner et al., 2019. Furthermore, using the droplet etched quantum dots with an oscillation period of > 500 ps is interesting to employ since this is longer than the typical lifetime of ~ 200 ps (D. Huber et al., 2017). In this case, we expect maximal correlation in configuration *AB* and no correlation at all times in the histogram for the *AA* configuration. Implementing these types of quantum dots in planar nanostructures will be investigated in the next chapter.

CHAPTER
9

LOW-STRAIN DROPLET-ETCHED QUANTUM DOTS COUPLED TO NANOSTRUCTURES

Progress on the integration of droplet etched quantum dots in planar nanophotonic structures are presented. These dots are promising for entanglement generation due to their low strain.

Low-strain quantum dots grown with droplet epitaxy as described in section 2.2.2 has been of increasing interest in the quantum dot community in the past decade. Firstly, they are highly appealing for polarization-entangled sources because of their low fine-structure splitting but have also proven strong candidates for single-photon sources and spin physics experiments (Bodey et al., 2019; Zhai et al., 2020).

The droplet etched GaAs quantum dot grown in an AlGaAs matrix has an emission wavelength of ~ 790 nm with a narrow spectral distribution between different quantum dots due to the predefined size from the nanoholes (see section 2.2.2). This important wavelength range, which is not covered by the traditional self-ass InAs quantum dots, offers the possibility possibility for interfacing with atomic or ion qubits (Akopian et al., 2010; Jahn et al., 2015; Keil et al., 2017). In contrast to their InAs counterparts, the droplet dots have been suffering from large amounts of charge-noise causing blinking and linewidth broadening, thus making strict resonant excitation challenging which has only in recent years been demonstrated (Jahn et al., 2015; Schöll et al., 2019; Tripathi et al., 2018). Despite this noise, droplet etched quantum dots have proven to generate polarization entanglement of remarkably high fidelity $> 90\%$ (D. Huber et al., 2018; Liu et al., 2019). Very recently, the implementation of droplet etched quantum dots in a diode heterostructure was successful almost fully overcoming the charge noise to the

same degree and maybe even better than observed for the InAs quantum dots (Zhai et al., 2020).

The results presented in this chapter, is work towards employing a droplet etched quantum dot in PCW as a source of entangled photons. We present the first results of the integration of droplet etched quantum dots with nanophotonic structures.

9.1 BULK SPECTROSCOPY AND FINE STRUCTURE SPLITTING

Before the fabrication of nanophotonic structures, we characterize the quantum dots in the bulk wafer. We employ an above-band excitation scheme, for the initial characterization using a 532 nm diode laser. We find that the spatial density of dots is approximately $1/\mu\text{m}^2$, meaning that a nanophotonic structure on this sample will contain only a few quantum dots per device. We note that this sample is without any diode heterostructure, and thus we expect to see emission from the neutral exciton and charged states simultaneously, under above-band excitation.

Figure 9.1(a) shows the spectrally resolved emission from a quantum dot in the sample where the neutral exciton, is the brightest peak. Additionally, we see emission from a charged trion state of the same quantum dot with a peak shifted by ~ 1 nm together with weak emission from other charged states. We confirm that the identified emission line is the neutral exciton by fitting the power saturation curve. The power-dependent emission intensity follows $A(1 - e^{-(P/P_{\text{sat}})^b})$, where P is the applied power, P_{sat} is the power where the emission saturates, b is the exponential slope and A is the saturated maximal counts. The recorded intensity is displayed in figure 9.1(b) together with the fit yielding a slope of $b = 1.05 \pm 0.02$ as expected for X. The dashed line marks the power at which the spectrum in (a) is recorded.

9.1.1 Fine Structure Splitting

One of the main motivations for investigating the droplet quantum dots is the low fine structure splitting. We, therefore, measure the fine structure splitting for an ensemble of quantum dots to confirm this property. The method employed in section 5.3 for measuring the fine structure splitting is not possible for these quantum dots with our available experimental equipment. This would require either a tunable narrow-band laser in the 790 nm range or electrical tuning of the quantum dot resonance, which is unavailable for this system. Therefore, we have implemented a different method exploiting the orthogonal polarization of the fine-structure-split exciton lines (Huo et al., 2013).

The experimental setup employed for the measurements is illustrated in figure 9.2(a). The quantum dot emission passes through a half waveplate and a polarizer before it is detected on the spectrometer. The spectrometer has a resolution of ~ 20 GHz and hence cannot resolve the low fine structure split emission lines. Instead, we record the spectra as a function of the half-wave plate (HWP) angle is shown in figure 9.2(b). We see that the emission appears in the same spectrometer pixel at all HWP angles, but

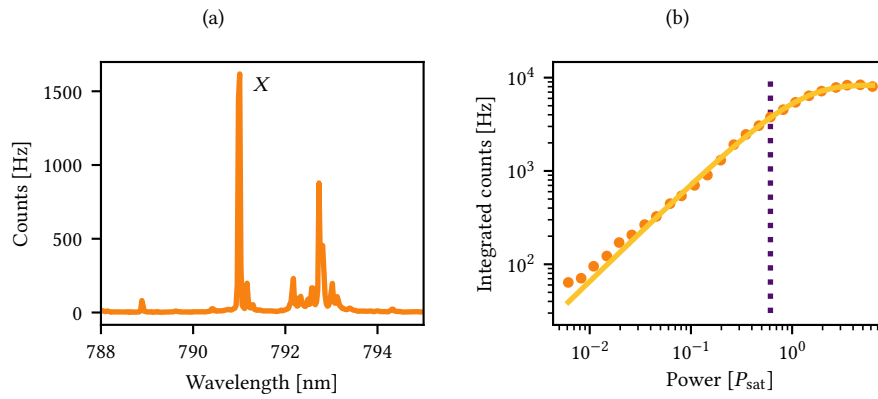


Figure 9.1: Quantum dot emission in a bulk sample with above-band excitation. (a) Spectrally resolved emission from a quantum dot, with the neutral exciton X_0 emission line marked. (b) Power saturation curve of neutral quantum dot emission. The dotted line marked the power at which the spectrum in (a) was recorded.

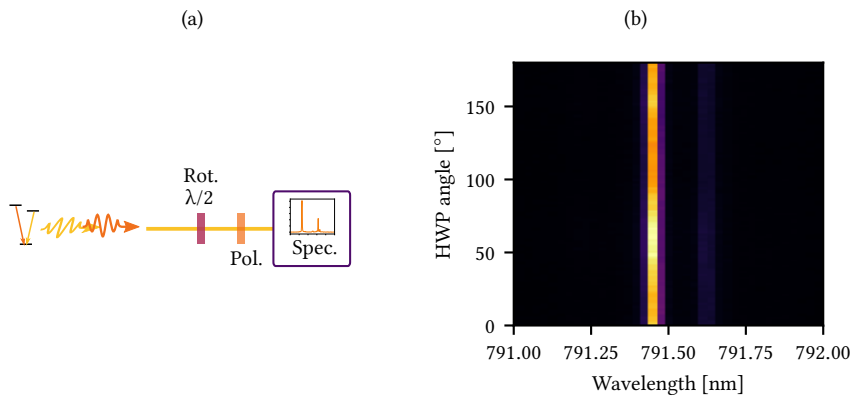


Figure 9.2: Fine structure splitting measurement. (a) The experimental setup used for fine structure splitting measurements, by the rotation of the $\lambda/2$ waveplate (HWP). (b) The emission spectrum from a quantum dot as a function of HWP angle. We observe that the majority of the emission is within a single pixel of the spectrometer, but by employing Voigt fitting for each HWP angle, an oscillation of the center value can be extracted. This is plotted in figure 9.3.

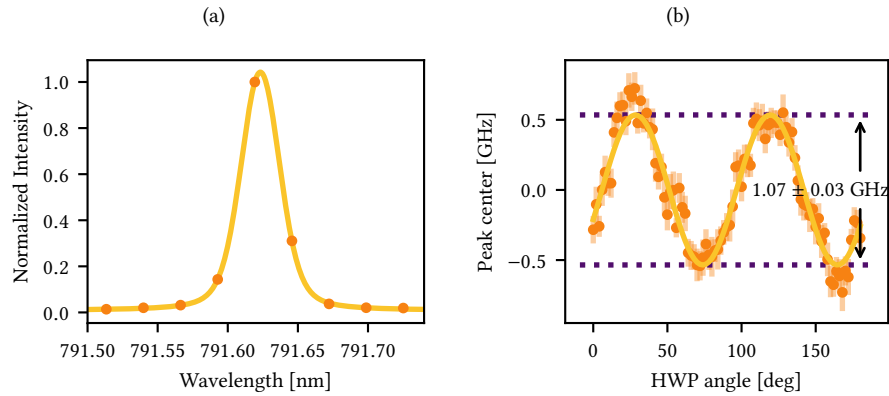


Figure 9.3: (a) Emission lineshape fitted to a Voigt function to extract the center value. (b) The center value of the emission lineshape extracted from fits like (a) plotted as a function of the HWP angle. The solid line is a cosine fit, where the amplitude corresponds to the fine structure splitting.

observe a slight variation in amplitude. This is a consequence of measuring on the two different dipoles as the waveplate is rotated.

The Lorentzian emission lineshape is fit to a Voigt profile to account for the Gaussian IRF, such a fit is shown in figure 9.3(a). From the fitted Voigt, we extract the center frequency for each of the recorded spectra, which is plotted as a function of HWP angle in figure 9.3(b). A clear oscillation of the center frequency is observed, and the amplitude of this oscillation corresponds to the fine structure splitting and is extracted from a cosine fit.

The measurement was repeated for a series of quantum dots on the sample and the extracted values for the fine structure splitting are summarized in figure 9.4(a). For comparison measured the fine structure splitting of self-assembled InAs quantum dots are presented in figure 9.4(b). We observe that not only is the average value of the fine structure splitting is much lower for the droplet quantum dots but also has a much smaller standard deviation.

9.2 NANOPHOTONIC STRUCTURES IN ALGAAS

The quantum dots are grown in the center of a 150 nm thick AlGaAs membrane, which is capped off by 4 nm GaAs to prevent oxidation. The nanophotonic structures are etched into the membrane using the same procedure as the GaAs membranes in the previous chapters. From the etched holes, there is a risk of reintroducing oxidation that could potentially affect the quantum dot emission. In this section, we present recorded data of quantum dots in nanophotonic structures that appear unaffected upon fabrication and with no degradation in emission properties over half a year of operation.

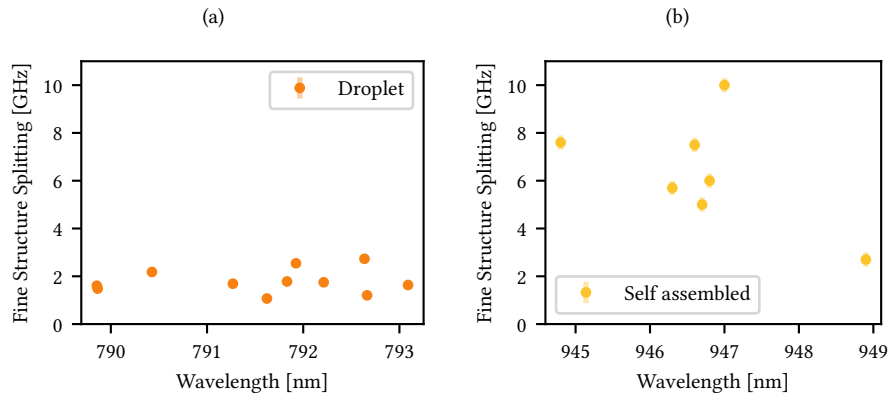


Figure 9.4: (a) Fine structure splittings of droplet etched GaAs quantum dots extracted from fits like in 9.3. (b) Fine structure splittings of self-assembled InAs quantum dots estimated from the RT frequency scan in figure 5.3.

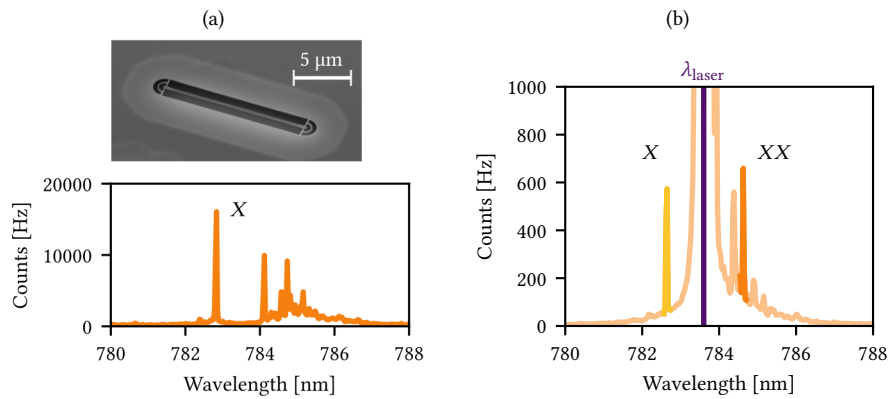


Figure 9.5: Quantum dot emission in a Nanobeam waveguide. (a) The top figure is an SEM image of a nanobeam waveguide with circular grating couplers. The bottom is the spectrally resolved emission from a quantum dot in a nanobeam waveguide under above-band excitation. The XX peak is not observed in this excitation scheme. (b) Spectrally resolved emission of the same quantum dot as in (a) under two-photon resonant excitation.

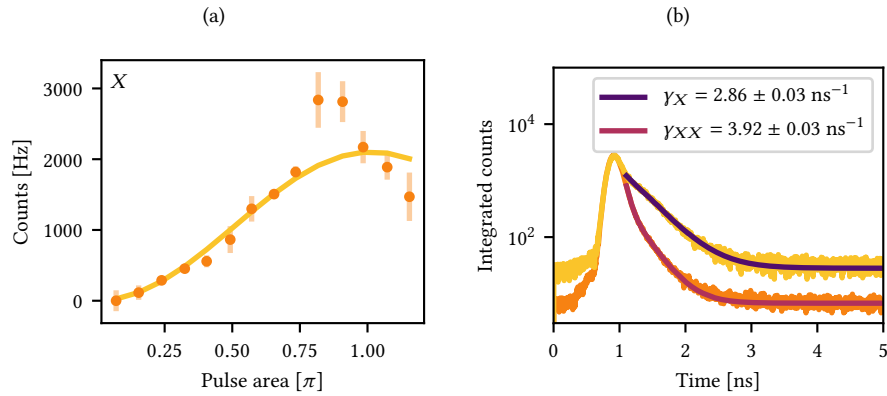


Figure 9.6: (a) Emission from a quantum dot exciton X in a nanobeam waveguide under two-photon resonant excitation showing Rabi oscillations with increasing excitation power. Points are estimated from the areas under peaks like in 9.5(b), with the laser background subtracted. (b) Lifetime measurement of the exciton X and biexciton XX under two-photon resonant excitation.

9.2.1 Droplet Quantum Dot Coupled to a Nanobeam Waveguide

To minimize the risk of oxidation we began with the simplest possible planar nanostructure, namely nanobeam waveguides terminated with circular grating outcouplers. An SEM image of a fabricated device in the AlGaAs membrane is displayed in the top panel of figure 9.5(a). Three arrays of single-mode waveguides with different widths were fabricated. We found quantum dots in several of them using above-band excitation. A spectrum of one of the quantum dots coupled to a nanobeam waveguide is displayed in the lower panel of figure 9.5(a). In general, the collection efficiency is improved with the nanophotonic structure, and we observe no effect on the emission spectrum from the fabrication.

To employ the droplet quantum dots for the generation of polarization-entangled photons, we need to use the two-photon resonant excitation scheme described in section 6.2. Figure 9.5(b) shows the emission from the same quantum dot under two-photon resonant excitation, where the exciton X clearly appears at the same wavelength and the biexciton appears $\sim 2 \text{ nm}$ longer wavelength. The two-photon resonant requires high excitation power, and in this case, it is evident from the spectrum that the laser pulse excites multiple other charged states in the quantum dot. The emission rate is not very high and not very well isolated, which makes the extinction of laser background and contributions from the other emission lines difficult. Therefore, performing further experiments was challenging. Figure 9.6(a) shows a Rabi oscillation of the X with increasing excitation power. The data points are extracted from the area under the peak using spectrometer measurements as in 9.5(b), where the significant laser background had to be subtracted. This subtraction leads to large uncertainty at high powers, and

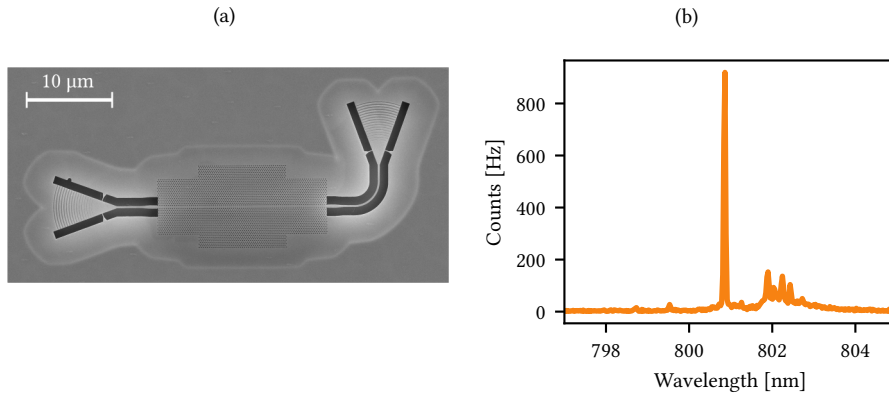


Figure 9.7: (a) A PCW terminated with shallow etched grating outcouplers fabricated in AlGaAs. (b) Emission from a quantum dot in a PCW under pulsed quasi-resonant excitation. The excitation laser is at 790 nm.

as seen in figure 9.6(a) this also leads to some deviation that is not modeled by the fit. In figure 9.6(b) time-resolved measurements reveal the emission rates of both the X and XX transitions. We notice that the ratio of the decay rates if the X and XX transitions is not the expected factor of two. We do not know the origin of this disparity and should be further investigated using other quantum dots. Further, we observe an identical rise time of the two which we expect to be longer for the exciton since it is populated through the biexciton state first⁽¹⁾. This could be explained by some amount of resonant excitation of the laser tails as also discussed in section 6.2.

9.2.2 Droplet Quantum Dot Coupled to a Photonic Crystal Waveguide

With the successful coupling of quantum dots to nanobeam waveguides, we move on to more complicated structures, namely PCW terminated with shallow etched grating outcouplers. The lattice parameters of the PCW are scaled-down compared to the one introduced in section 5.1 such that the photonic crystal transmission band shifts to 790 nm. This is achieved with a lattice constant of $a = 246$ nm and hole radius of $r = 46$ nm. This small hole size is close to the limit of what can be reliably fabricated. Figure 9.7(a) shows an SEM of a successfully fabricated device where the holes were inspected in SEM and exhibit radii close to the design value.

Due to limited wafer material of good high quantum dot quality, the sample containing the devices in figure 9.7(a) had slightly worse emission properties when investigated in bulk before fabrication. Only a small fraction of the quantum dots inspected exhibited narrow emission lines under above-band excitation. Therefore finding quantum

(1) Note that the same detectors were employed and the decay rates are similar to figure 6.8, where we do see a different rise time.

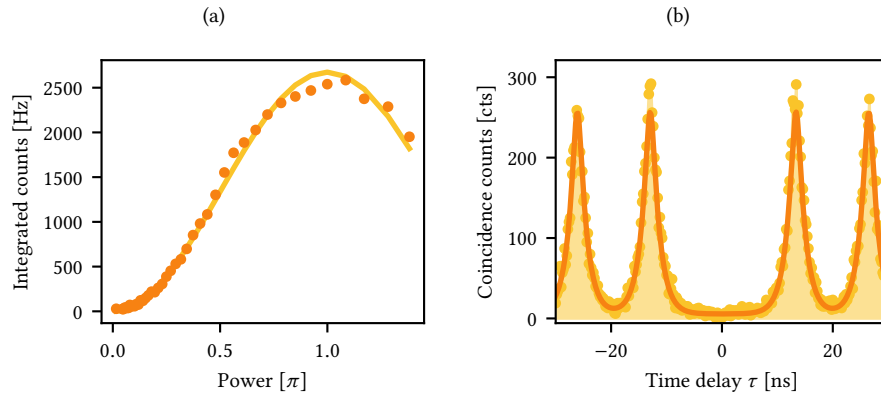


Figure 9.8: Emission under quasi-resonant excitation from a quantum dot coupled to a PCW (a) Rabi oscillations observed with increased laser power. (b) Autocorrelation histogram was recorded in an HBT experiment. A fit to equation 5.6 is displayed with a solid line.

dots that were both coupled to a PCW and exhibited good emission properties was challenging.

Figure 9.7(b) shows the emission of a quantum dot coupled to a PCW excited with pulsed *quasi*-resonant excitation. The excitation laser is at 790 nm, which is close to the *p*-shell of the quantum dot exciton. In this scheme, the neutral exciton emission line is isolated from the laser background. Rabi oscillations of the spectrally filtered exciton are observed with increasing excitation power as seen in figure 9.8(a). To confirm the single-photon property of the emission from the droplet quantum dots we perform an HBT experiment to extract $g^{(2)}(0)$. The recorded coincidence histogram is displayed in figure 9.8(b). The data are fit to the multi-peak function in equation 5.6, which is plotted with a solid line. We observe clear suppression of the central peak, exhibiting almost perfect purity as a consequence of the far-detuned excitation laser. Due to low coincidence counts in figure 9.8(b) it is not possible to reliably extract a value for $g^{(2)}(0)$, since the counts of the central peak are below the background noise level. However, from the clear suppression of the central peak, we can confirm the single-photon property of the emission.

* * *

In this chapter, we have investigated the possibility to integrate droplet-etched GaAs quantum dots into planar nanophotonic structures. Firstly, the high symmetry of the quantum dots was confirmed by a series of fine-structure splitting measurements. The average fine structure splitting was measured to be 1.8 GHz.

After the fabrication of nanophotonic structures, we see improved collection efficiency under above-band excitation. Further two-photon resonant excitation was performed, and Rabi oscillations of the exciton emission were observed. Preliminary results from a quantum dot coupled to a PCW under quasi-resonant excitation was presented. The collection efficiency was further improved by the implementation of shallow-etched gratings. From an autocorrelation measurement, we confirm high single-photon purity of the emission.

Recent experiments have successfully realized GaAs quantum dots embedded in a *p-i-n* diode heterostructure that exhibited excellent emission properties Zhai et al., 2020. Therefore, integrating a charged controlled droplet etched quantum dot sample with nanophotonic structures is a natural next step. In this context, the experiments in this chapter pave way for subsequent experiments with electrically-contacted GaAs quantum dots that would be important for deterministic entangled photon generation. Moreover, the low-strain quantum dots are also expected to possess longer electron spin coherence times and hence important for spin-photon entanglement generation schemes.

CONCLUSIONS AND OUTLOOK

Conclusions and summary of the work carried out in this thesis, and an outlook towards future work for single and entangled photons from quantum dots in photonic crystal waveguides.

Quantum dots excited with pulsed resonant excitation have high potential as deterministic single- and multi-photon sources, which are key ingredients in a scalable quantum network. To realize this, efficient coupling of the emitted photons is crucial. In this thesis, we have studied the emission from quantum dots coupled to photonic crystal waveguides, where near-unity coupling efficiency can be achieved.

The thesis started out with an introduction to the theoretical framework for employing a quantum dot for single-photon emission. After introducing the photonic crystal waveguide as an efficient nanophotonic structure, we described the experimental setup which was carefully characterized and optimized for high-performance experiments.

We have shown that near transform-limited linewidths can be achieved for a large fraction of the quantum dots coupled to a photonic crystal waveguide using resonant transmission measurements. This is a consequence of reduced charge noise due to the diode heterostructure embedding the quantum dots.

High in-fiber single-photon rates of 10 MHz with a purity quantified through $g^{(2)}(0) < 1\%$ has been demonstrated in chapter 5. Importantly, the photon stream was demonstrated to be indistinguishable across more than 100 photons through HOM interference experiments, which is a key step in realizing a scalable single-photon source. For an optimized HOM interference experiment, quantum interference visibilities as high as 98.4% were demonstrated. Our source thereby represents the new state-of-the-art for single-photon sources and paves the route towards demonstration of quantum advantage using photonic boson sampling. The high indistinguishability was achieved in an

excitation pulse bandwidth optimized experiment. The optimized configuration was found by systematically performing HBT and HOM experiments at different excitation laser bandwidths. Further, an alternative resonant excitation scheme was investigated, namely two-photon resonant excitation of the biexciton state. We found that this scheme is both inefficient in the photon generation rate as well as exhibited limited indistinguishability of $\sim 50\%$. This limitation is likely intrinsic to the excitation scheme due to the cascaded nature of the biexciton decay.

While the biexciton cascade might not be suitable for single-photon generation, it is an exciting candidate for high-fidelity polarization entanglement (D. Huber et al., 2017; H. Wang, Hu, et al., 2019). In this thesis, we show how polarization entanglement is generated from a quantum dot and is measured using quantum state tomography. Upon its integration in a planar nanophotonic structure, the polarization state of the entangled photons cannot be preserved. We demonstrate how the polarization-encoded entangled state can be efficiently converted to path-encoded entanglement using a glide-plane-symmetric photonic crystal waveguide. Efficient conversion of the polarization to path entanglement provides a clear pathway for on-chip, on-demand entangled-photon generation.

We rounded this thesis off by detailing the progress for the integration of low-strain droplet quantum dots with planar nanostructures. The low strain leads to a reduced fine-structure splitting in comparison to the self-assembled InAs quantum dots as confirmed experimentally. Successful integration of the droplet-etched GaAs quantum dots into nanophotonic structures is experimentally evidenced with a series of characterization measurements.

Outlook

The improved indistinguishability of the single-photon source demonstrated in this thesis together with the infrastructure employed in the boson sampling experiment performed in H. Wang, Qin, et al., 2019 would enable boson sampling with 54 photons (Uppu et al., 2020). It was shown in Uppu et al., 2020 that achieving a total source efficiency of 78% is the key step towards the demonstration of quantum advantage. Therefore the efficiencies presented in table 5.1 need to be improved. The intrinsic source efficiency of $\eta_S > 82\%$ is mainly limited by a non-unity β which can be improved for a better-located quantum dot and could be realized through deterministic positioning of the quantum dot (He et al., 2017; Ollivier et al., 2020; Pregolato et al., 2020). There are multiple steps to improve the setup efficiency of $\eta_{\text{setup}} = 8\%$. The directionality is straight forward to improve to 100% by employing a single-sided device, and the spectral filtering efficiency can be improved to $> 98\%$ using a free-space cavity. By using grating outcouplers with a DBR layer, and by replacing the collection optics by efficiency-optimized components, the total outcoupling efficiency could be improved to be $> 85\%$. The chip-to-fiber efficiency could further be improved by replacing the grating outcouplers with on-chip spot-size converters (e.g. inverted tapers) (Uğurlu et al., 2019), where efficiencies exceeding 96% have been achieved (Pu et al., 2010; Tiecke et al., 2015).

While the infrastructural challenges in scaling up to 50 photon experiments (e.g. acquiring large number of single-photon detectors, designing circuits) are significant, the high-quality source demonstrated in this thesis is directly relevant for few photon experiments such as, heralded two-photon entanglement (Zhang et al., 2008) generation or scaling up to higher photon numbers entanglement such as forming GHZ states (Greenberger et al., 1990; Pan et al., 2000). To this end, the single-photon pulse train emitted from the quantum dot should be demultiplexed into different spatial modes. This can be done with very high efficiency using a bulk experimental setup (Hummel et al., 2019). An alternative approach is to perform the demultiplexing directly on the chip, where photons can be routed in an integrated waveguide using electrically controlled switches (Lodahl, 2017; Papon et al., 2019). The high source rate could enable heralded generation of multi-photon entangled states with comparable (maybe higher) probability to SPDC sources. Crucially, the multi-photon entangled states generated from quantum dot single-photons would possess higher fidelity due to the ultra-low multi-photon emission in comparison to SPDC single-photon sources. Such multi-photon states (e.g. GHZ, cluster, graph states (Adcock et al., 2019; Asavanant et al., 2019; Larsen et al., 2019; Schwartz et al., 2016)) are relevant for implementing one-way quantum computing and error-corrected quantum communication (Gimeno-Segovia et al., 2015; Rudolph, 2017; Varnava et al., 2006).

Our demonstration of the conversion of polarization entanglement to spatial entanglement paves a clear path towards on-chip, high-fidelity entanglement generation. Complete conversion and preservation of the entanglement rely on the quantum dot being located in a perfectly chiral point. This can be achieved using deterministic positioning (He et al., 2017; Ollivier et al., 2020; Pregolato et al., 2020). The next step would be to implement the low-strain droplet-etched quantum dots coupled to a glide plane waveguide and to perform the conversion experiment as presented in chapter 8. Quantum state tomography should also be performed on the path-converted entangled state to confirm the entanglement preservation. This can be realized either by converting back to the polarization basis using polarization diversity gratings (Roelkens et al., 2010; J. Wang et al., 2016), or performing spatial interferometric tomography, which could be integrated on-chip (Solntsev & Sukhorukov, 2017). Similar to the case of the single-photon source, the entanglement generation efficiency can be improved and efficiencies exceeding 70 % should be reachable. Such a high-efficiency entanglement source is a key resource for realizing device-independent quantum key distribution schemes (Acín et al., 2007; Máttar et al., 2020).

BIBLIOGRAPHY

- Aaronson, S., & Arkhipov, A. (2013). “The computational complexity of linear optics”. *Theor. Comput.*, 9(4), 143–252 (cit. on p. 6).
- Acín, A., Brunner, N., Gisin, N., Massar, S., Pironio, S., & Scarani, V. (2007). “Device-Independent Security of Quantum Cryptography against Collective Attacks”. *Physical Review Letters*, 98(23), 230501 (cit. on pp. 7, 133).
- Adcock, J. C., Morley-Short, S., Silverstone, J. W., & Thompson, M. G. (2019). “Hard limits on the postselectability of optical graph states”. *Quantum Science and Technology*, 4(1), 15010 (cit. on p. 133).
- Akopian, N., Perinetti, U., Wang, L., Rastelli, A., Schmidt, O. G., & Zwiller, V. (2010). “Tuning single GaAs quantum dots in resonance with a rubidium vapor”. *Applied Physics Letters*, 97(8), 082103 (cit. on pp. 14, 121).
- Arcari, M., Söllner, I., Javadi, A., Lindskov Hansen, S., Mahmoodian, S., Liu, J., Thyrestrup, H., Lee, E. H., Song, J. D., Stobbe, S., & Lodahl, P. (2014). “Near-Unity Coupling Efficiency of a Quantum Emitter to a Photonic Crystal Waveguide”. *Physical Review Letters*, 113 (cit. on pp. 34, 35, 38, 66).
- Arute, F., Arya, K., Babbush, R., Bacon, D., Bardin, J., Barends, R., Biswas, R., Boixo, S., Brandao, F., Buell, D., Burkett, B., Chen, Y., Chen, J., Chiaro, B., Collins, R., Courtney, W., Dunsworth, A., Farhi, E., Foxen, B., ... Martinis, J. (2019). “Quantum Supremacy using a Programmable Superconducting Processor”. *Nature*, 574, 505–510 (cit. on p. 6).
- Asavanant, W., Shiozawa, Y., Yokoyama, S., Charoensombutamon, B., Emura, H., Alexander, R. N., Takeda, S., Yoshikawa, J.-i., Menicucci, N. C., Yonezawa, H., & Furusawa, A. (2019). “Generation of time-domain-multiplexed two-dimensional cluster state”. *Science*, 366(6463), 373–376 (cit. on p. 133).
- Aspuru-Guzik, A., & Walther, P. (2012). “Photonic quantum simulators”. *Nat. Phys.*, 8(4), 285–291 (cit. on p. 6).
- Ates, S., Ulrich, S. M., Reitzenstein, S., Löffler, A., Forchel, A., & Michler, P. (2009). “Post-Selected Indistinguishable Photons from the Resonance Fluorescence of a Single Quantum Dot in a Microcavity”. *Physical Review Letters*, 103(16), 167402 (cit. on pp. 29, 31).
- Bardeen, J., & Brattain, W. H. (1948). “The Transistor, A Semi-Conductor Triode”. *Physical Review*, 74(2), 230–231 (cit. on p. 5).

- Bell, J. S. (1964). "On the Einstein Podolsky Rosen paradox". *Physics Physique Fizika*, 1, 195–200 (cit. on p. 7).
- Bennett, C. H., & Brassard, G. (1984). "Quantum cryptography: Public key distribution and coin tossing". *International Conference on Computers, Systems and Signal Processing*, 175, 8. <http://www.sciencedirect.com/science/article/pii/S0304397514004241> (cit. on p. 6)
- Bennett, C. H., & Brassard, G. (2014). "Quantum cryptography: Public key distribution and coin tossing". *Theoretical Computer Science*, 560(P1), 7–11 (cit. on p. 6).
- Bentham, C., Itskevich, I. E., Coles, R. J., Royall, B., Clarke, E., O'Hara, J., Prtljaga, N., Fox, A. M., Skolnick, M. S., & Wilson, L. R. (2015). "On-chip electrically controlled routing of photons from a single quantum dot". *Applied Physics Letters*, 106(22), 221101 (cit. on p. 37).
- Bodey, J. H., Stockill, R., Denning, E. V., Gangloff, D. A., Éthier-Majcher, G., Jackson, D. M., Clarke, E., Hugues, M., Gall, C. L., & Atatüre, M. (2019). "Optical spin locking of a solid-state qubit". *npj Quantum Information*, 5(1), 1–6 (cit. on p. 121).
- Brown, R. H., & Twiss, R. Q. (1956). "Correlation between photons in two coherent beams of light". *Nature*, 177(4497), 27–29 (cit. on p. 71).
- Bulgarini, G., Reimer, M. E., Bouwes Bavinck, M., Jöns, K. D., Dalacu, D., Poole, P. J., Bakkers, E. P., & Zwiller, V. (2014). "Nanowire waveguides launching single photons in a Gaussian mode for ideal fiber coupling". *Nano Letters*, 14(7), 4102–4106 (cit. on pp. 31, 107).
- Calsamiglia, J., & Lütkenhaus, N. (2001). "Maximum efficiency of a linear-optical Bell-state analyzer". *Applied Physics B: Lasers and Optics*, 72(1), 67–71 (cit. on p. 7).
- Carolan, J., Harrold, C., Sparrow, C., Martín-López, E., Russell, N. J., Silverstone, J. W., Shadbolt, P. J., Matsuda, N., Oguma, M., Itoh, M., Marshall, G. D., Thompson, M. G., Matthews, J. C., Hashimoto, T., O'Brien, J. L., & Laing, A. (2015). "Universal linear optics". *Science*, 349(6249), 711–716 (cit. on p. 6).
- Claudon, J., Bleuse, J., Malik, N. S., Bazin, M., Jaffrennou, P., Gregersen, N., Sauvan, C., Lalanne, P., & Gérard, J.-M. (2010). "A highly efficient single-photon source based on a quantum dot in a photonic nanowire". *Nature Photonics*, 4(3), 174–177 (cit. on pp. 7, 32).
- Clauser, J. F., Horne, M. A., Shimony, A., & Holt, R. A. (1969). "Proposed Experiment to Test Local Hidden-Variable Theories". *Phys. Rev. Lett.*, 23, 880–884 (cit. on p. 7).
- Coles, R. J., Price, D. M., Dixon, J. E., Royall, B., Clarke, E., Kok, P., Skolnick, M. S., Fox, A. M., & Makhonin, M. N. (2016). "Chirality of nanophotonic waveguide with embedded quantum emitter for unidirectional spin transfer". *Nature Communications*, 7 (cit. on p. 36).
- Das, S., Zhai, L., Čepulskovskis, M., Javadi, A., Mahmoodian, S., Lodahl, P., & Sørensen, A. S. (2019). "A wave-function ansatz method for calculating field correlations and its application to the study of spectral filtering and quantum dynamics of multi-emitter systems". <http://arxiv.org/abs/1912.08303> (cit. on pp. 87, 88)

- Deutsch, D., & Jozsa, R. (1992). "Rapid solution of problems by quantum computation". *Proceedings of the Royal Society of London. Series A: Mathematical and Physical Sciences*, 439(1907), 553–558 (cit. on p. 6).
- Ding, X., He, Y., Duan, Z. C., Gregersen, N., Chen, M. C., Unsleber, S., Maier, S., Schneider, C., Kamp, M., Höfling, S., Lu, C. Y., & Pan, J. W. (2016). "On-Demand Single Photons with High Extraction Efficiency and Near-Unity Indistinguishability from a Resonantly Driven Quantum Dot in a Micropillar". *Physical Review Letters*, 116(2), 020401 (cit. on pp. 29, 31, 32, 83).
- Dousse, A., Suffczynski, J., Beveratos, A., Krebs, O., Lemaitre, A., Sagnes, I., Bloch, J., Voisin, P., & Senellart, P. (2010). "Ultrabright source of entangled photon pairs". *Nature*, 466(7303), 217–220 (cit. on pp. 31, 99).
- Dreessen, C. L., Ouellet-Plamondon, C., Tighineanu, P., Zhou, X., Midolo, L., Sørensen, A. S., & Lodahl, P. (2019). "Suppressing phonon decoherence of high performance single-photon sources in nanophotonic waveguides". *Quantum Science and Technology*, 4(1), 15003 (cit. on pp. 24, 67).
- Eberhard, P. H. (1993). "Background level and counter efficiencies required for a loophole-free Einstein-Podolsky-Rosen experiment". *Phys. Rev. A*, 47, R747–R750 (cit. on p. 7).
- Ekert, A. K. (1991). "Quantum cryptography based on Bell's theorem." *Physical Review Letters*, 67 6, 661–663 (cit. on p. 7).
- Fano, U. (1961). "Effects of configuration interaction on intensities and phase shifts". *Physical Review*, 124(6), 1866–1878 (cit. on p. 68).
- Fischer, K. A., Hanschke, L., Kremser, M., Finley, J. J., Müller, K., & Vučković, J. (2018). "Pulsed Rabi oscillations in quantum two-level systems: Beyond the area theorem". *Quantum Science and Technology*, 3(1), 14006 (cit. on p. 86).
- Fognini, A., Ahmadi, A., Daley, S. J., Reimer, M. E., & Zwiller, V. (2018). "Universal fine-structure eraser for quantum dots". *Opt. Express*, 26(19), 24487–24496 (cit. on p. 109).
- Gerry, C., & Knight, P. (2004). *Introductory Quantum Optics*. Cambridge University Press. (Cit. on p. 71).
- Gimeno-Segovia, M., Shadbolt, P., Browne, D. E., & Rudolph, T. (2015). "From Three-Photon Greenberger-Horne-Zeilinger States to Ballistic Universal Quantum Computation". *Phys. Rev. Lett.*, 115, 020502 (cit. on p. 133).
- Gisin, N., Ribordy, G., Tittel, W., & Zbinden, H. (2002). "Quantum cryptography". *Rev. Mod. Phys.*, 74, 145–195 (cit. on p. 111).
- Greenberger, D. M., Horne, M. A., Shimony, A., & Zeilinger, A. (1990). "Bell's theorem without inequalities". *American Journal of Physics*, 58(12), 1131–1143 (cit. on p. 133).
- Grover, L. K. (1996). "A fast quantum mechanical algorithm for database search". *Proceedings of the twenty-eighth annual ACM symposium on Theory of computing - STOC '96, Part F129452*, 212–219 (cit. on p. 6).
- Grover, L. K. (2001). "From Schrödinger's equation to the quantum search algorithm". *American Journal of Physics*, 69(7), 769–777 (cit. on p. 6).

- Ha, N., Mano, T., Chou, Y. L., Wu, Y. N., Cheng, S. J., Bocquel, J., Koenraad, P. M., Ohtake, A., Sakuma, Y., Sakoda, K., & Kuroda, T. (2015). "Size-dependent line broadening in the emission spectra of single GaAs quantum dots: Impact of surface charge on spectral diffusion". *Physical Review B*, 92(7), 075306 (cit. on p. 68).
- Hansen, S. L. (2017). *Single-Photon Manipulation in Nanophotonic Circuits* (Doctoral dissertation). Niels Bohr Institute, University of Copenhagen. (Cit. on p. 38).
- He, Y.-M., Liu, J., Maier, S., Emmerling, M., Gerhardt, S., Davanço, M., Srinivasan, K., Schneider, C., & Höfling, S. (2017). "Deterministic implementation of a bright, on-demand single-photon source with near-unity indistinguishability via quantum dot imaging". *Optica*, 4(7), 802–808 (cit. on pp. 67, 119, 132, 133).
- Hong, C. K., Ou, Z. Y., & Mandel, L. (1987). "Measurement of subpicosecond time intervals between two photons by interference". *Physical Review Letters*, 59(18), 2044–2046 (cit. on p. 75).
- Houel, J., Kuhlmann, A. V., Greuter, L., Xue, F., Poggio, M., Warburton, R. J., Gerardot, B. D., Dalgarno, P. A., Badolato, A., Petroff, P. M., Ludwig, A., Reuter, D., & Wieck, A. D. (2012). "Probing single-charge fluctuations at a GaAs/AlAs interface using laser spectroscopy on a nearby InGaAs quantum dot". *Physical Review Letters*, 108(10), 107401 (cit. on p. 68).
- Huber, D., Reindl, M., Covre Da Silva, S. F., Schimpf, C., Martín-Sánchez, J., Huang, H., Piredda, G., Edlinger, J., Rastelli, A., & Trotta, R. (2018). "Strain-Tunable GaAs Quantum Dot: A Nearly Dephasing-Free Source of Entangled Photon Pairs on Demand". *Physical Review Letters*, 121(3), 033902 (cit. on pp. 32, 121).
- Huber, D., Reindl, M., Huo, Y., Huang, H., Wildmann, J. S., Schmidt, O. G., Rastelli, A., & Trotta, R. (2017). "Highly indistinguishable and strongly entangled photons from symmetric GaAs quantum dots". *Nature Communications*, 8, 15506 (cit. on pp. 13, 14, 25, 26, 97, 99, 107, 109, 119, 132).
- Huber, T., Predojević, A., Khoshnegar, M., Dalacu, D., Poole, P. J., Majedi, H., & Weihs, G. (2014). "Polarization entangled photons from quantum dots embedded in nanowires". *Nano Letters*, 14(12), 7107–7114 (cit. on pp. 25, 31, 99, 103, 106, 107).
- Hudson, A. J., Stevenson, R. M., Bennett, A. J., Young, R. J., Nicoll, C. A., Atkinson, P., Cooper, K., Ritchie, D. A., & Shields, A. J. (2007). "Coherence of an entangled exciton-photon state". *Physical Review Letters*, 99(26), 266802 (cit. on p. 25).
- Hughes, S. (2004). "Enhanced single-photon emission from quantum dots in photonic crystal waveguides and nanocavities". *Optics Letters*, 29(22), 2659 (cit. on p. 34).
- Hummel, T., Ouellet-Plamondon, C., Ugur, E., Kulkova, I., Lund-Hansen, T., Broome, M. A., Uppu, R., & Lodahl, P. (2019). "Efficient demultiplexed single-photon source with a quantum dot coupled to a nanophotonic waveguide". *Appl. Phys. Lett.*, 115(2), 21102 (cit. on p. 133).
- Huo, Y. H., Rastelli, A., & Schmidt, O. G. (2013). "Ultra-small excitonic fine structure splitting in highly symmetric quantum dots on GaAs (001) substrate". *Appl. Phys. Lett.*, 102(152105) (cit. on pp. 13, 122).
- Jahn, J. P., Munsch, M., Béguin, L., Kuhlmann, A. V., Renggli, M., Huo, Y., Ding, F., Trotta, R., Reindl, M., Schmidt, O. G., Rastelli, A., Treutlein, P., & Warburton,

- R. J. (2015). “An artificial Rb atom in a semiconductor with lifetime-limited linewidth”. *Physical Review B*, 92(24), 245439 (cit. on pp. 14, 67, 121).
- James, D. F. V., Kwiat, P. G., Munro, W. J., & White, A. G. (2001). “Measurement of qubits”. *Physical Review A*, 64(052312) (cit. on pp. 100–102).
- Javadi, A., Mahmoodian, S., Söllner, I., & Lodahl, P. (2018). “Numerical modeling of the coupling efficiency of single quantum emitters in photonic-crystal waveguides”. *Journal of the Optical Society of America B*, 35(3), 514 (cit. on pp. 34, 35).
- Javadi, A., Söllner, I., Arcari, M., Hansen, S. L., Midolo, L., Mahmoodian, S., Kiršanskė, G., Pregolato, T., Lee, E. H., Song, J. D., Stobbe, S., & Lodahl, P. (2015). “Single-photon non-linear optics with a quantum dot in a waveguide”. *Nat. Commun.*, 6(1), 8655 (cit. on pp. 33, 34, 36, 57, 68).
- Joannopoulos, J. D., Johnson, S. G., Winn, J. N., & Meade, R. D. (2011). *Photonic crystals: Molding the flow of light* (Second edition). Princeton University Press. <http://ab-initio.mit.edu/book/photonic-crystals-book.pdf>. (Cit. on p. 33)
- Johansen, J., Julsgaard, B., Stobbe, S., Hvam, J. M., & Lodahl, P. (2010). “Probing long-lived dark excitons in self-assembled quantum dots”. *Phys. Rev. B*, 81(8), 81304 (cit. on pp. 22, 74).
- Jöns, K. D., Schweickert, L., Versteegh, M. A., Dalacu, D., Poole, P. J., Gulinatti, A., Giudice, A., Zwiller, V., & Reimer, M. E. (2017). “Bright nanoscale source of deterministic entangled photon pairs violating Bell’s inequality”. *Scientific Reports*, 7(1), 1–11 (cit. on pp. 31, 99, 107).
- Kaneda, F., & Kwiat, P. G. (2019). “High-efficiency single-photon generation via large-scale active time multiplexing”. *Sci. Adv.*, 5(10), eaaw8586 (cit. on p. 7).
- Keil, R., Zopf, M., Chen, Y., Höfer, B., Zhang, J., Ding, F., & Schmidt, O. G. (2017). “Solid-state ensemble of highly entangled photon sources at rubidium atomic transitions”. *Nature Communications*, 8(1), 1–8 (cit. on pp. 13, 14, 121).
- Kimble, H. J., Dagenais, M., & Mandel, L. (1977). “Photon Antibunching in Resonance Fluorescence”. *Phys. Rev. Lett.*, 39, 691–695 (cit. on p. 7).
- Kimble, H. J. (2008). “The quantum internet”. *Nature*, 453(7198), 1023–1030 (cit. on pp. 5, 9).
- Kuhlmann, A. V., Houel, J., Ludwig, A., Greuter, L., Reuter, D., Wieck, A. D., Poggio, M., & Warburton, R. J. (2013). “Charge noise and spin noise in a semiconductor quantum device”. *Nature Physics*, 9(9), 570–575 (cit. on p. 24).
- Kuhlmann, A. V., Prectel, J. H., Houel, J., Ludwig, A., Reuter, D., Wieck, A. D., & Warburton, R. J. (2015). “Transform-limited single photons from a single quantum dot”. *Nat. Commun.*, 6(1), 8204 (cit. on p. 67).
- Kurtsiefer, C., Mayer, S., Zarda, P., & Weinfurter, H. (2000). “Stable Solid-State Source of Single Photons”. *Phys. Rev. Lett.*, 85, 290–293 (cit. on p. 7).
- Kwiat, P. G., Mattle, K., Weinfurter, H., Zeilinger, A., Sergienko, A. V., & Shih, Y. (1995). “New High-Intensity Source of Polarization-Entangled Photon Pairs”. *Phys. Rev. Lett.*, 75, 4337–4341 (cit. on p. 7).
- Lang, B., Oulton, R., & Beggs, D. M. (2017). “Optimised photonic crystal waveguide for chiral light-matter interactions”. *Journal of Optics*, 19(4), 045001 (cit. on p. 36).

- Larsen, M. V., Guo, X., Breum, C. R., Neergaard-Nielsen, J. S., & Andersen, U. L. (2019). "Deterministic generation of a two-dimensional cluster state". *Science*, 366(6463), 369–372 (cit. on p. 133).
- Linskens, A. F., Holleman, I., Dam, N., & Reuss, J. (1996). "Two-photon Rabi oscillations". *Physical Review A*, 54(6), 4854–4862 (cit. on p. 92).
- Liu, J., Konthasinghe, K., Davanço, M., Lawall, J., Anant, V., Verma, V., Mirin, R., Nam, S. W., Song, J. D., Ma, B., Chen, Z. S., Ni, H. Q., Niu, Z. C., & Srinivasan, K. (2018). "Single Self-Assembled InAs/GaAs Quantum Dots in Photonic Nanostructures: The Role of Nanofabrication". *Phys. Rev. Applied*, 9(6), 64019 (cit. on p. 68).
- Liu, J., Su, R., Wei, Y., Yao, B., da Silva, S. F. C., Yu, Y., Iles-Smith, J., Srinivasan, K., Rastelli, A., Li, J., & Wang, X. (2019). "A solid-state source of strongly entangled photon pairs with high brightness and indistinguishability". *Nature Nanotechnology*, 14(6), 586–593 (cit. on pp. 13, 26, 32, 97, 99, 121).
- Löbl, M. C., Scholz, S., Söllner, I., Ritzmann, J., Denneulin, T., Kovács, A., Kardynał, B. E., Wieck, A. D., Ludwig, A., & Warburton, R. J. (2019). "Excitons in InGaAs quantum dots without electron wetting layer states". *Communications Physics*, 2(1), 1–7 (cit. on p. 13).
- Löbl, M. C., Söllner, I., Javadi, A., Pregolato, T., Schott, R., Midolo, L., Kuhlmann, A. V., Stobbe, S., Wieck, A. D., Lodahl, P., Ludwig, A., & Warburton, R. J. (2017). "Narrow optical linewidths and spin pumping on charge-tunable close-to-surface self-assembled quantum dots in an ultrathin diode". *Physical Review B*, 96(16), 165440 (cit. on p. 67).
- Lodahl, P. (2017). "Quantum-dot based photonic quantum networks". *Quantum Sci. Technol.*, 3(1), 13001 (cit. on p. 133).
- Lodahl, P., Mahmoodian, S., & Stobbe, S. (2015). "Interfacing single photons and single quantum dots with photonic nanostructures". *Rev. Mod. Phys.*, 87(2), 347–400 (cit. on pp. 12, 19, 35).
- Lounis, B., & Moerner, W. E. (2000). "Single photons on demand from a single molecule at room temperature". *Nature*, 407(6803), 491–493 (cit. on p. 7).
- Lund-Hansen, T., Stobbe, S., Julsgaard, B., Thyrestrup, H., Sünner, T., Kamp, M., Forchel, A., & Lodahl, P. (2008). "Experimental Realization of Highly Efficient Broadband Coupling of Single Quantum Dots to a Photonic Crystal Waveguide". *Phys. Rev. Lett.*, 101, 113903 (cit. on p. 7).
- Luxmoore, I. J., Wasley, N. A., Ramsay, A. J., Thijssen, A. C. T., Oulton, R., Hugues, M., Fox, A. M., & Skolnick, M. S. (2013). "Optical control of the emission direction of a quantum dot". *Applied Physics Letters*, 103(24), 241102 (cit. on p. 111).
- Madsen, K. H., Ates, S., Liu, J., Javadi, A., Albrecht, S. M., Yeo, I., Stobbe, S., & Lodahl, P. (2014). "Efficient out-coupling of high-purity single photons from a coherent quantum dot in a photonic-crystal cavity". *Physical Review B*, 90, 155303 (cit. on p. 76).
- Mahmoodian, S., Prindal-Nielsen, K., Söllner, I., Stobbe, S., & Lodahl, P. (2017). "Engineering chiral light-matter interaction in photonic crystal waveguides with slow light". *Optical Materials Express*, 7(1), 43 (cit. on pp. 36, 37).

- Marquez, J., Geelhaar, L., & Jacobi, K. (2001). “Atomically resolved structure of InAs quantum dots”. *Applied Physics Letters*, 78(16), 2309–2311 (cit. on p. 11).
- Mátar, A., Kołodzyński, J., Skrzypczyk, P., Cavalcanti, D., Banaszek, K., & Acín, A. (2020). “Device-independent quantum key distribution with single-photon sources”. *Quantum*, 4, 260 (cit. on pp. 7, 133).
- Meystre, P., & Sargent, M. (2007). *Elements of quantum optics*. Springer Berlin Heidelberg. (Cit. on pp. 20–22).
- Michler, P., Kiraz, A., Becher, C., Schoenfeld, W. V., Petroff, P. M., Zhang, L., Hu, E., & Imamoglu, A. (2000). “A Quantum Dot Single-Photon Turnstile Device”. *Science*, 290(5500), 2282–2285 (cit. on p. 7).
- Michler, P. (2017). *Quantum Dots for Quantum Information Technologies*. (Cit. on p. 9).
- Midolo, L., Hansen, S. L., Zhang, W., Papon, C., Schott, R., Ludwig, A., Wieck, A. D., Lodahl, P., & Stobbe, S. (2017). “Electro-optic routing of photons from a single quantum dot in photonic integrated circuits”. *Optics Express*, 25(26), 33514 (cit. on p. 37).
- Müller, M., Bounouar, S., Jöns, K. D., Glässl, M., & Michler, P. (2014). “On-demand generation of indistinguishable polarization-entangled photon pairs”. *Nature Photonics*, 8, 224–228 (cit. on p. 97).
- Najer, D., Söllner, I., Sekatski, P., Dolique, V., Löbl, M. C., Riedel, D., Schott, R., Starosielec, S., Valentin, S. R., Wieck, A. D., Sangouard, N., Ludwig, A., & Warburton, R. J. (2019). “A gated quantum dot strongly coupled to an optical microcavity”. *Nature*, 575(7784), 622–627 (cit. on p. 31).
- Olesen, C. T. (2020). *Efficient Generation of Pure and Indistinguishable Single Photons* (Master Thesis). University of Copenhagen. (Cit. on p. 77).
- Ollivier, H., Maillette de Buy Wenniger, I., Thomas, S., Wein, S. C., Harouri, A., Coppola, G., Hilaire, P., Millet, C., Lemaître, A., Sagnes, I., Krebs, O., Lanco, L., Loredó, J. C., Antón, C., Somaschi, N., & Senellart, P. (2020). “Reproducibility of High-Performance Quantum Dot Single-Photon Sources”. *ACS Photonics*, 7(4), 1050–1059 (cit. on pp. 119, 132, 133).
- Pagliano, F., Cho, Y., Xia, T., Van Otten, F., Johne, R., & Fiore, A. (2014). “Dynamically controlling the emission of single excitons in photonic crystal cavities”. *Nat. Commun.*, 5(1), 5786 (cit. on p. 53).
- Pan, J. W., Bouwmeester, D., Daniell, M., Weinfurter, H., & Zeilinger, A. (2000). “Experimental test of quantum nonlocality in three-photon Greenberger-Horne-Zeilinger entanglement”. *Nature*, 403(6769), 515–519 (cit. on p. 133).
- Papon, C., Zhou, X., Thyrestrup, H., Liu, Z., Stobbe, S., Schott, R., Wieck, A. D., Ludwig, A., Lodahl, P., & Midolo, L. (2019). “Nanomechanical single-photon routing”. *Optica*, 6(4), 524 (cit. on pp. 37, 133).
- Pedersen, F. T., Wang, Y., Olesen, C. T., Scholz, S., Wieck, A. D., Ludwig, A., Löbl, M. C., Warburton, R. J., Midolo, L., Uppu, R., & Lodahl, P. (2020). “Near Transform-limited Quantum Dot Linewidths in a Broadband Photonic Crystal Waveguide”. *ACS Photonics* (cit. on p. 55).
- Pregolato, T., Chu, X.-L., Schröder, T., Schott, R., Wieck, A. D., Ludwig, A., Lodahl, P., & Rotenberg, N. (2020). “Deterministic positioning of nanophotonic waveguides

- around single self-assembled quantum dots". *APL Photonics*, 5(8), 086101 (cit. on pp. 67, 119, 132, 133).
- Prilmüller, M., Huber, T., Müller, M., Michler, P., Weihs, G., & Predojević, A. (2018). "Hyperentanglement of Photons Emitted by a Quantum Dot". *Physical Review Letters*, 121(11), 110503 (cit. on p. 31).
- Pu, M., Liu, L., Ou, H., Yvind, K., & Hvam, J. M. (2010). "Ultra-low-loss inverted taper coupler for silicon-on-insulator ridge waveguide". *Optics Communications*, 283(19), 3678–3682 (cit. on p. 132).
- Purcell, E. M. (1946). "Proceedings of the american physical society". *Physical Review*, 69(11-12), 680–681 (cit. on p. 29).
- Rastelli, A., Stufler, S., Schliwa, A., Songmuang, R., Manzano, C., Costantini, G., Kern, K., Zrenner, A., Bimberg, D., & Schmidt, O. G. (2004). "Hierarchical self-assembly of GaAs/AlGaAs quantum dots". *Physical Review Letters*, 92(16), 166104 (cit. on p. 13).
- Reimer, M. E., Bulgarini, G., Akopian, N., Hocoavar, M., Bavinck, M. B., Verheijen, M. A., Bakkers, E. P., Kouwenhoven, L. P., & Zwiller, V. (2012). "Bright single-photon sources in bottom-up tailored nanowires". *Nature Communications*, 3(1), 1–6 (cit. on p. 31).
- Renema, J. J., Menssen, A., Clements, W. R., Triginer, G., Kolthammer, W. S., & Walmsley, I. A. (2018). "Efficient Classical Algorithm for Boson Sampling with Partially Distinguishable Photons". *Phys. Rev. Lett.*, 120(22), 220502 (cit. on p. 6).
- Rivest, R. L., Shamir, A., & Adleman, L. (1978). "A Method for Obtaining Digital Signatures and Public-Key Cryptosystems". *Communications of the ACM*, 21(2), 120–126 (cit. on p. 6).
- Roelkens, G., Vermeulen, D., Laere, F. V., Selvaraja, S., Scheerlinck, S., Taillaert, D., Bogaerts, W., Dumon, P., Thourhout, D. V., & Baets, R. (2010). "Bridging the Gap Between Nanophotonic Waveguide Circuits and Single Mode Optical Fibers Using Diffractive Grating Structures". *Journal of Nanoscience and Nanotechnology*, 10, 1551–1562 (cit. on pp. 38, 119, 133).
- Rudolph, T. (2017). "Why I am optimistic about the silicon-photon route to quantum computing". *APL Photonics*, 2(3), 30901 (cit. on p. 133).
- Santori, C., Fattal, D., Vučković, J., Solomon, G. S., & Yamamoto, Y. (2002). "Indistinguishable photons from a single-photon device". *Nature*, 419(6907), 594–597 (cit. on pp. 7, 77).
- Schöll, E., Hanschke, L., Schweickert, L., Zeuner, K. D., Reindl, M., Covre Da Silva, S. F., Lettner, T., Trotta, R., Finley, J. J., Müller, K., Rastelli, A., Zwiller, V., & Jöns, K. D. (2019). "Resonance Fluorescence of GaAs Quantum Dots with Near-Unity Photon Indistinguishability". *Nano Letters*, 19(4), 2404–2410 (cit. on pp. 13, 83, 121).
- Schöll, E., Schweickert, L., Hanschke, L., Zeuner, K. D., Sbresny, F., Lettner, T., Trivedi, R., Reindl, M., da Silva, S. F. C., Trotta, R., Finley, J. J., Vučković, J., Müller, K., Rastelli, A., Zwiller, V., & Jöns, K. D. (2020). "The crux of using the cascaded emission of a 3-level quantum ladder system to generate indistinguishable photons". <http://arxiv.org/abs/2006.05476> (cit. on pp. 97, 98)

- Schwartz, I., Cogan, D., Schmidgall, E. R., Don, Y., Gantz, L., Kenneth, O., Lindner, N. H., & Gershoni, D. (2016). "Deterministic generation of a cluster state of entangled photons". *Science*, 354(6311), 434–437 (cit. on p. 133).
- Schweickert, L., Jöns, K. D., Zeuner, K. D., da Silva, S. F., Huang, H., Lettner, T., Reindl, M., Zichi, J., Trotta, R., Rastelli, A., & Zwiller, V. (2018). "On-demand generation of background-free single photons from a solid-state source". *Appl. Phys. Lett.*, 112(9), 93106 (cit. on pp. 85, 93, 95).
- Shen, Y., Harris, N. C., Skirlo, S., Prabhu, M., Baehr-Jones, T., Hochberg, M., Sun, X., Zhao, S., Laroche, H., Englund, D., & Soljacic, M. (2017). "Deep learning with coherent nanophotonic circuits". *Nature Photonics*, 11(7), 441–446 (cit. on p. 6).
- Shin, J., Chang, Y. C., & Dagli, N. (2008). "0.3 V drive voltage GaAs/AlGaAs substrate removed Mach-Zehnder intensity modulators". *Applied Physics Letters*, 92(20), 201103 (cit. on p. 37).
- Shockley, W. (1949). "The Theory of p-n Junctions in Semiconductors and p-n Junction Transistors". *Bell System Technical Journal*, 28(3), 435–489 (cit. on p. 5).
- Shor, P. (1994). "Algorithms for quantum computation: discrete logarithms and factoring". *Proceedings 35th Annual Symposium on Foundations of Computer Science*, 124–134 (cit. on p. 6).
- Söllner, I., Mahmoodian, S., Hansen, S. L., Midolo, L., Javadi, A., Kiršanskė, G., Pregolato, T., El-Ella, H., Lee, E. H., Song, J. D., Stobbe, S., & Lodahl, P. (2015). "Deterministic photon-emitter coupling in chiral photonic circuits". *Nature Nanotechnology*, 10(9), 775–778 (cit. on pp. 36, 111).
- Solntsev, A. S., & Sukhorukov, A. A. (2017). "Path-entangled photon sources on nonlinear chips". *Reviews in Physics*, 2, 19–31 (cit. on pp. 119, 133).
- Somaschi, N., Giesz, V., De Santis, L., Loredano, J. C., Almeida, M. P., Hornecker, G., Portalupi, S. L., Grange, T., Antón, C., Demory, J., Gómez, C., Sagnes, I., Lanzillotti-Kimura, N. D., Lemaître, A., Auffeves, A., White, A. G., Lanco, L., & Senellart, P. (2016). "Near-optimal single-photon sources in the solid state". *Nature Photonics*, 10(5), 340–345 (cit. on pp. 29, 31, 83).
- Steck, D. A. (2007). *Quantum and Atom Optics*. <http://steck.us/teaching>. (Cit. on pp. 21, 22)
- Stevenson, R. M., Young, R. J., Atkinson, P., Cooper, K., Ritchie, D. A., & Shields, A. J. (2006). "A semiconductor source of triggered entangled photon pairs". *Nature*, 439(7073), 178–182 (cit. on p. 99).
- Thyrrerstrup, H., Kiršanskė, G., Le Jeannic, H., Pregolato, T., Zhai, L., Raahauge, L., Midolo, L., Rotenberg, N., Javadi, A., Schott, R., Wieck, A. D., Ludwig, A., Löbl, M. C., Söllner, I., Warburton, R. J., & Lodahl, P. (2018). "Quantum optics with near-lifetime-limited quantum-dot transitions in a nanophotonic waveguide". *Nano Lett.*, 18(3), 1801–1806 (cit. on p. 67).
- Tiecke, T. G., Nayak, K. P., Thompson, J. D., Peyronel, T., de Leon, N. P., Vuletić, V., & Lukin, M. D. (2015). "Efficient fiber-optical interface for nanophotonic devices". *Optica*, 2(2), 70–75 (cit. on p. 132).
- Tighineanu, P., Dreessen, C. L., Flindt, C., Lodahl, P., & Sørensen, A. S. (2018). "Phonon decoherence of quantum dots in photonic structures: broadening of the zero-

- phonon line and the role of dimensionality". *Phys. Rev. Lett.*, 120(25), 257401 (cit. on pp. 24, 44, 67, 83).
- Tillmann, M., Dakić, B., Heilmann, R., Nolte, S., Szameit, A., & Walther, P. (2013). "Experimental boson sampling". *Nature Photonics*, 7(7), 540–544 (cit. on p. 6).
- Tomm, N., Javadi, A., Antoniadis, N. O., Najer, D., Löbl, M. C., Korsch, A. R., Schott, R., Valentin, S. R., Wieck, A. D., Ludwig, A., & Warburton, R. J. (2020). "A bright and fast source of coherent single photons". *arXiv:2007.12654v1*. <https://arxiv.org/abs/2007.12654> (cit. on pp. 31, 32, 83)
- Tripathi, L. N., He, Y. M., Dusanowski, Ł., Wroński, P. A., Lu, C. Y., Schneider, C., & Höfling, S. (2018). "Resonance fluorescence from an atomic-quantum-memory compatible single photon source based on GaAs droplet quantum dots". *Applied Physics Letters*, 113(2), 021102 (cit. on p. 121).
- Uğurlu, A. D., Thyrestrup, H., Uppu, R., Ouellet-Plamondon, C., Schott, R., Wieck, A. D., Ludwig, A., Lodahl, P., & Midolo, L. (2019). "Suspended Spot-Size Converters for Scalable Single-Photon Devices". *Adv. Quantum Technol.*, 3, 1900076 (cit. on p. 132).
- Unsleber, S., He, Y.-M., Gerhardt, S., Maier, S., Lu, C.-Y., Pan, J.-W., Gregersen, N., Kamp, M., Schneider, C., & Höfling, S. (2016). "Highly indistinguishable on-demand resonance fluorescence photons from a deterministic quantum dot micropillar device with 74% extraction efficiency". *Optics Express*, 24(8), 8539 (cit. on pp. 29, 31).
- Uppu, R., Pedersen, F. T., Wang, Y., Olesen, C. T., Papon, C., Zhou, X., Midolo Leonardo, S. S., Wieck, A. D., Ludwig, A., & Lodahl, P. (2020). "Scalable integrated single-photon source". *arXiv:2003.08919*. <https://arxiv.org/abs/2003.08919> (cit. on pp. 38, 55, 66, 83, 132)
- Uppu, R., Wolterink, T. A. W., Tentrup, T. B. H., & Pinkse, P. W. H. (2016). "Quantum optics of lossy asymmetric beam splitters". *Opt. Express*, 24(15), 16440–16449 (cit. on p. 80).
- Varnava, M., Browne, D. E., & Rudolph, T. (2006). "Loss Tolerance in One-Way Quantum Computation via Counterfactual Error Correction". *Phys. Rev. Lett.*, 97, 120501 (cit. on p. 133).
- Wang, C. F., Badolato, A., Wilson-Rae, I., Petroff, P. M., Hu, E., Urayama, J., & Imamoglu, A. (2004). "Optical properties of single InAs quantum dots in close proximity to surfaces". *Applied Physics Letters*, 85(16), 3423–3425 (cit. on p. 68).
- Wang, C., Wang, F. X., Chen, H., Wang, S., Chen, W., Yin, Z. Q., He, D. Y., Guo, G. C., & Han, Z. F. (2017). "Realistic Device Imperfections Affect the Performance of Hong-Ou-Mandel Interference With Weak Coherent States". *Journal of Lightwave Technology*, 35(23), 4996–5002 (cit. on p. 80).
- Wang, H., He, Y., Li, Y.-H., Su, Z.-E., Li, B., Huang, H.-L., Ding, X., Chen, M.-C., Liu, C., Qin, J., Li, J.-P., Y.-M., H., Schneider, C., Kamp, M., Peng, C.-Z., Höfling, S., Lu, C.-Y., & Pan, J.-W. (2017). "High-efficiency multiphoton boson sampling". *Nat. Photon.*, 11(6), 361–365 (cit. on p. 6).
- Wang, H., Hu, H., Chung, T. H., Qin, J., Yang, X., Li, J. P., Liu, R. Z., Zhong, H. S., He, Y. M., Ding, X., Deng, Y. H., Dai, Q., Huo, Y. H., Höfling, S., Lu, C. Y., &

- Pan, J. W. (2019). "On-Demand Semiconductor Source of Entangled Photons Which Simultaneously Has High Fidelity, Efficiency, and Indistinguishability". *Physical Review Letters*, 122(11), 113602 (cit. on pp. 26, 32, 97, 107, 109, 132).
- Wang, H., Qin, J., Ding, X., Chen, M.-C., Chen, S., You, X., He, Y.-M., Jiang, X., Wang, Z., You, L., Renema, J. J., Höfling, S., Lu, C.-Y., & Pan, J.-W. (2019). "Boson Sampling with 20 Input Photons and a 60-Mode Interferometer in a 10^{14} -Dimensional Hilbert Space". *Phys. Rev. Lett.*, 123, 250503 (cit. on pp. 6, 132).
- Wang, J., Bonneau, D., Villa, M., Silverstone, J. W., Santagati, R., Miki, S., Yamashita, T., Fujiwara, M., Sasaki, M., Terai, H., Tanner, M. G., Natarajan, C. M., Hadfield, R. H., O'Brien, J. L., & Thompson, M. G. (2016). "Chip-to-chip quantum photonic interconnect by path-polarization interconversion". *Optica Vol 3. No. 4* (cit. on pp. 119, 133).
- Wang, J., Sciarrino, F., Laing, A., & Thompson, M. G. (2019). "Integrated photonic quantum technologies". *Nat. Photon.*, 1–12 (cit. on p. 37).
- Warburton, R. J. (2013). "Single spins in self-assembled quantum dots". *Nat. Mater.*, 12(6), 483–493 (cit. on pp. 15, 17).
- Wehner, S., Elkouss, D., & Hanson, R. (2018). "Quantum internet: A vision for the road ahead". *Science*, 362(6412), eaam9288 (cit. on pp. 5, 9).
- Winik, R., Cogan, D., Don, Y., Schwartz, I., Gantz, L., Schmidgall, E. R., Livneh, N., Rapaport, R., Buks, E., Gershoni, D., & Viterbi, E. (2017). "On-demand source of maximally entangled photon pairs using the biexciton-exciton radiative cascade". *Physical Review B*, 95, 235435 (cit. on p. 105).
- Yamamoto, Y., Santori, C., & Pelton, M. (2000). "Regulated and entangled photons from a single quantum dot". *Physical Review Letters*, 84(11), 2513–2516 (cit. on p. 99).
- Young, A. B., Thijssen, A. C. T., Beggs, D. M., Androvitsaneas, P., Kuipers, L., Rarity, J. G., Hughes, S., & Oulton, R. (2015). "Polarization Engineering in Photonic Crystal Waveguides for Spin-Photon Entanglers". *Phys. Rev. Lett.*, 115, 153901 (cit. on pp. 36, 111).
- Zeuner, K. D., Jöns, K. D., Schweickert, L., Hedlund, C. R., Lobato, C. N., Lettner, T., Wang, K., Gyger, S., Schöll, E., Steinhauer, S., Hammar, M., & Zwiller, V. (2019). "On-demand generation of entangled photon pairs in the telecom C-band for fiber-based quantum networks". *arXiv:1912.04782*. <http://arxiv.org/abs/1912.04782> (cit. on pp. 25, 32, 109, 119)
- Zhai, L., Löbl, M. C., Nguyen, G. N., Ritzmann, J., Javadi, A., Spinnler, C., Wieck, A. D., Ludwig, A., & Warburton, R. J. (2020). "Low-noise GaAs quantum dots for quantum photonics". *Nature Communications*, 11(1), 4745 (cit. on pp. 14, 121, 122, 129).
- Zhang, Q., Bao, X.-H., Lu, C.-Y., Zhou, X.-Q., Yang, T., Rudolph, T., & Pan, J.-W. (2008). "Demonstration of a scheme for the generation of "event-ready" entangled photon pairs from a single-photon source". *Phys. Rev. A*, 77, 062316 (cit. on p. 133).
- Zhong, H.-S., Li, Y., Li, W., Peng, L.-C., Su, Z.-E., Hu, Y., He, Y.-M., Ding, X., Zhang, W., Li, H., Zhang, L., Wang, Z., You, L., Wang, X.-L., Jiang, X., Li, L., Chen, Y.-A., Liu, N.-L., Lu, C.-Y., & Pan, J.-W. (2018). "12-Photon Entanglement and

- Scalable Scattershot Boson Sampling with Optimal Entangled-Photon Pairs from Parametric Down-Conversion”. *Phys. Rev. Lett.*, 121, 250505 (cit. on p. 7).
- Zhou, X., Kulkova, I., Lund-Hansen, T., Hansen, S. L., Lodahl, P., & Midolo, L. (2018). “High-efficiency shallow-etched grating on GaAs membranes for quantum photonic applications”. *Applied Physics Letters*, 113(25), 251103 (cit. on pp. 38, 50, 51).